Master's thesis

2019

Sondre Haug

NTNU
Norwegian University of
Science and Technology
Faculty of Engineering
Department of Marine Technology

Master's thesis

Sondre Haug

Robust Hybrid Heading Control of Autonomous Ships

June 2019

NTNU
Norwegian University of
Science and Technology

NTNU
Norwegian University of
Science and Technology

NTNU
Norwegian University of
Science and Technology

Robust Hybrid Heading Control of Autonomous Ships

Sondre Haug

Marine Technology
Submission date: June 2019
Supervisor: Roger Skjetne, IMT
Co-supervisor: Andrew Teel, USCB
Jon Bjørnø, IMT

Norwegian University of Science and Technology
Department of Marine Technology

NTNU Trondheim
Norwegian University of Science and Technology
Department of Marine Technology

MSC THESIS DESCRIPTION SHEET

Name of the candidate: Haug, Sondre
Field of study: Marine control engineering
Thesis title (Norwegian): Robust hybrid retningsstyring for autonome skip
Thesis title (English): Robust hybrid heading control of autonomous ships

Background

In dynamic positioning and autopilots for ships, the yaw angle, typically defined in the ±180 degree range, is controlled to a desired yaw. Using this interval of the reals to constrain the heading within causes several issues:

- Different devices, sensors, etc. represent angles in different ranges, so that mappings to ±180 degrees are needed. We call this a rad2pipi mapping.
- Two angles within ±180 degrees may have a difference outside this range, so that a rad2pipi mapping back into the ±180 range is again needed (but often forgotten).
- An error between two angles, after correct rad2pipi mapping, is bounded within the [-180,+180] degree interval. In some control algorithms it may be necessary to transform this further to the [-∞,+∞] interval to get an unbounded error potential when moving towards the maximum error.
- The 180 degrees error point causes a robustness issue, where arbitrarily small noise levels may make the controller switch at high frequency between moving clockwise or counterclockwise towards the desired heading angle, and in some cases make the controller get stuck at 180 degrees offset.
- The 180 degrees error point typically makes out an additional equilibrium, rendering stability non-global.

In this MSc thesis, the objective is to study robust hybrid control designs for the yaw on S^1 to achieve globally stable closed-loop dynamics based on hybrid feedback with an S^1 representation of angles. This is a building block towards more resilient control designs for autonomous ships. The project will include a literature review, algorithm development, implementation of simulation models for verification of the control algorithms, and experimental testing in MC-Lab.

Work description

1. Provide a short and concise background and literature review with information and relevant references on:
   - Autonomy for marine control systems.
   - Relevant dynamical model(s) of ships.
   - Hybrid dynamical systems, e.g.: "Hybrid Dynamical Systems", R. Goebel, R.G. Sanfelice, and A.R. Teel, IEEE Control Systems Magazine, vol. 29, no. 2, pp. 28-93.
   - Hybrid control of planar rotations, e.g., the ACC 2010 paper by Mayhew and Teel.
   - Synergistic Lyapunov functions for hybrid feedback control of rotations, e.g. ACC and 2011 CDC papers by Mayhew et al.
   - DP, Autopilot, and path-following control designs.

   Write a list with abbreviations and definitions of terms, explaining relevant concepts related to the literature study and project assignment.

<u>In the following, all formulations of angles shall be done by unit vectors on S^1.</u>

2. Formulate the 1DOF Heading Control (HC) problem, using the 1DOF Nomoto model as control design model (CDM), but reformulated on S^1. Perform a heading control design based on «Hybrid Control of Planar Rotations» by Mayhew and Teel (2010):
   - Design control laws based on several potential functions, using yaw rate r as control input:
     - Analyze and discuss the closed-loop behavior in terms of stability, convergence rates, etc.
   - Design and present the hybrid control mechanism that ensures GAS:
     - By switching between two control laws.
     - By switching and using hysteresis by a dwell time.
   - Extend the kinematic control design using backstepping to derive a hybrid HC with rudder as input.
     - Analyze and discuss the closed-loop behavior in terms of transient response, convergence rates, and steady-state behavior.
   - Verify and discuss the designs for the Nomoto CDM based on simulation with the CDM.

3. Formulate the 2DOF Velocity Vector Control (VVC) problem, incl. CDM w/disturbances, assumptions, and control objective:

- Include an irrotational constant current in the global frame. Define and describe yaw, course, and sideslip angles, as well as relevant velocity vectors and total speed in the S^1 formulation.
- Perform the non-hybrid control design for the VVC problem. Simulate on the CDM and discuss the closed-loop performance, incl. assessment of equilibria and stability.
- Perform the hybrid control design to achieve global stability. Present the hybrid mechanism(s) that achieve robust global stability. Simulate on the CDM and verify stable and robust closed-loop performance.
- Present a Simulation Verification Model (SVM) for the VVC problem. Simulate on the SVM and discuss the closed-loop behavior.

4. Extend the VVC problem into a Path-Following Control (PFC) problem. Formulate the PFC problem, incl. CDM w/disturbances, assumptions, and control objective.
   - Present and implement a path-generation method for relevant paths.
   - Derive and present a Line-of-sight (LOS) guidance algorithm, that combined with the hybrid VVC control law will ensure convergence to and following the path, including current compensation.
   - Simulate on the CDM and verify stable and robust closed-loop performance.
   - Define some relevant test scenarios / case studies for testing the hybrid path-following autopilot. Simulate on the SVM and discuss the heading and path-following responses with currents in various directions, with/without waves, etc.

5. Work together with other students in MC-Lab on establishing simulations model(s) and carrying out HIL- and MC-Lab testing. Implement and test your HC, VVC, and PFC control designs, and present and discuss the results.

Specifications

The scope of work may prove to be larger than initially anticipated. By the approval from the supervisor, described topics may be deleted or reduced in extent without consequences with regard to grading.

The candidate shall present personal contribution to the resolution of problems within the scope of work. Theories and conclusions should be based on mathematical derivations and logic reasoning identifying the various steps in the deduction.

The report shall be organized in a logical structure to give a clear exposition of background, results, assessments, and conclusions. The text should be brief and to the point, with a clear language. Rigorous mathematical deductions and illustrating figures are preferred over lengthy textual descriptions. The report shall have font size 11 pts., and it is not expected to be longer than 70 A4-pages, 100 B5-pages, from introduction to conclusion, unless otherwise agreed upon. It shall be written in English (preferably US) and contain the following elements: Title page, abstract, acknowledgements, thesis specification, list of symbols and acronyms, table of contents, introduction with objective, background, and scope and delimitations, main body with problem formulations, derivations/developments and results, conclusions with recommendations for further work, references, and optional appendices. All figures, tables, and equations shall be numerated. The original contribution of the candidate and material taken from other sources shall be clearly identified. Work from other sources shall be properly acknowledged using quotations and a Harvard citation style (e.g. *natbib* Latex package). The work is expected to be conducted in an honest and ethical manner, without any sort of plagiarism and misconduct. Such practice is taken very seriously by the university and will have consequences. NTNU can use the results freely in research and teaching by proper referencing, unless otherwise agreed upon.

The thesis shall be submitted with an electronic copy to the main supervisor and department according to NTNU administrative procedures. The final revised version of this thesis description shall be included after the title page. Computer code, pictures, videos, dataseries, etc., shall be included electronically with the report.

Start date: January, 2019 **Due date:** As specified by the administration.

Supervisor: Roger Skjetne
Co-advisor(s): Andrew Teel (theory), and J. Bjørnø, E. Ueland, H. Schmidt-Didlaukies (MC-Lab)

Trondheim, 27.03.2019

Roger Skjetne
Digitally signed by Roger Skjetne
Date: 2019.03.27 11:52:28 +01'00'

Roger Skjetne
Supervisor

Abstract

In the later years, there has been an increased interest in control system design and guidance for autonomous vessels. These systems has high demands for robustness such that they behave as expected. Autopilots for ships are based on control of the yaw angle typically defined in the ±180 degree range. Using this intervals of reals to constrain the heading within this interval causes several issues related to mapping, measurement noise and error calculation. As the sensors and devices using angles may have different ranges, a correct mapping to the same interval must be performed in order for their signals to be processed in a system. The error between two angles could also end up outside this interval, which means mapping of the error also must be performed. In addition, small noise may trick the vessel to be stuck at a 180 degree offset, as it can not determine which direction the vessel needs to turn in order to achieve the control objective.

In this thesis, a background study of relevant dynamic models for ships, maneuvering models, guidance systems and autonomous systems is first presented, as well as a brief introduction to hybrid dynamical systems and control. A robust hybrid heading controller(HHC) based on mapping the angles to an $\mathbb{S}^1$ representation is then derived, tested, analyzed and simulated on a 3DOF ship model of the scale model of C/S Inocean Cat I Drillship (CSAD). The HHC is derived by first analyzing several potential function candidates and their deduced non-hybrid kinematic controls. Then a global diffeomorphism is applied to derive two controls and put these into a hybrid structure. By a smooth switching strategy and backstepping approach, the needed control force is derived such that Global Asymptotic Stability(GAS) can be achieved. The HHC is then extended to a Velocity Vector Control(VVC) problem including disturbances such as ocean currents, and the proposed method uses adaptive control techniques and sideslip compensation to achieve GAS of the desired velocity vector. The VVC problem is extended to a Path-Following Control(PFC) problem, and different path-generation methods and Line-of-Sight(LOS) guidance on $\mathbb{S}^1$ is developed to ensure convergence to the path both with and without ocean currents.

The yielded results are promising, as the simulations proved to work as intended. The HHC ensured the heading to converge to its desired setpoint, and the VVC design was able to track both constant and time varying desired velocity vectors, both with and without currents. In addition, the PFC design proved to be able to converge to both straight and curved paths with a constant velocity along the path. To validate the results, physical experiments in the ocean basin at the Marine Cybernetics Laboratory (MC-lab) at the Norwegian University of Science and Technology(NTNU) was conducted. The proposed control can be extended and tested with more complex operations such as with wind, waves and constraints in the thrust allocation, as the used simulation model is not of high-fidelity. The work done in this thesis is a stepping stone for more advanced control systems of ships that increases the level of autonomy and robustness, and can be extended to spherical orientation control on $\mathbb{S}^2$ such as underwater robotics. Full scale testing would also give valuable insight on how the overall performance is compared to model tests.

Sammendrag

I de senere år har det vært økt interesse for styringssystemdesign og veiledning av autonome fartøy. Etter hvert som kompleksiteten i disse systemene øker, er det stor etterspørsel etter å designe robuste systemer som oppfører seg som forventet. Autopiloter for skip er basert på kontroll av en retnings-vinkel som vanligvis er definert i ± 180 graders området. Ved å bruke dette intervallet av for å begrense retningen kan det forårsake flere numeriske problemer relatert til mapping, målestøy og feilberegning. Ettersom sensorene og enhetene som bruker vinkler kan ha forskjellige definisjonsområder, må en korrekt mapping til samme intervall utføres for at signalene skal behandles i et system. Feilen mellom to vinkler kan også ende opp utenfor dette intervallet, noe som betyr at mapping av feilen også må utføres. I tillegg kan liten støy lure fartøyet til å sitte fast ved 180 graders forskyvning, da det ikke kan bestemme hvilken retning fartøyet må vende for å oppnå målet.

I denne oppgaven presenteres en bakgrunnsundersøkelse av relevante dynamiske modeller for skip, manøvreringsmodeller, veiledningssystemer og autonome systemer, samt en introduksjon til hybride dynamiske systemer og regulering. En robust hybrid retningskontroller (HHC) basert på kartlegging av vinklene til en $\mathbb{S}^1$-representasjon blir deretter utledet, testet, analysert og simulert på en skipmodell i tre frihetsgrader av skalamodellen til skipet C/S Inocean Cat I Drillship (CSAD). HHC er utledet ved først å analysere flere potensialfunksjons-kandidater og deres avledede ikke-hybride kinematiske kontrollere. Deretter brukes en global diffeomorfi for å utlede to kontrollere og sette disse inn i en hybrid struktur. Ved en glatt byttestrategi mellom disse og backstepping-tilnærming er den nødvendige kontrollstyrken utledet slik at Global Asymptotisk Stabilitet (GAS) kan oppnås. HHC blir deretter utvidet til et hastighetsvektor(VVC)-problem, inkludert forstyrrelser som havstrømmer, og den foreslåtte metoden bruker adaptive kontrollteknikker og sideslip- kompensasjon for å oppnå GAS. VVC-problemet er utvidet til et banefølgings(PFC)-problem, og forskjellige veidannelsesmetoder og siktelinje-veiledning på $\mathbb{S}^1$ er utviklet for å sikre konvergens til banen både med og uten havstrømmer.

Resultatene er lovende, da simuleringene viste seg å fungere som ønsket. HHC sørget for at retningen konvergerte til ønsket settpunkt, og VVC-designet var i stand til å følge både konstante og tidsvarierende ønskede hastighetsvektorer, både med og uten havstrømmer. I tillegg viste PFC-designet å kunne konvergere til både rette og buede baner med konstant hastighet langs banen. For å validere resultatene ble fysiske eksperimenter i havbassenget ved Marin Kybernetikk Laboratoriet (MC-lab) ved Norges Teknisk-Naturvitenskapelige Universitet(NTNU) gjennomført. Den foreslåtte kontrolleren bli utvidet og testet med mer komplekse operasjoner som for eksempel vind, bølger og begrensninger i thrust-allokering, da den brukte simuleringsmodellen ikke er høynøyaktig. Arbeidet i denne oppgaven er en skritt på veien for mer avanserte kontrollsystemer for skip som øker selvstendighetsnivået og robustheten, og kan også utvides sfærisk orienteringskontroll på $\mathbb{S}^2$ som undervannsrobotikk. Fullskala testing vil også gi verdifullt innblikk i hvordan den samlede ytelsen sammenlignes med modelltester.

Preface

This Master's Thesis has been written during the spring of 2019 as a concluding part of a Master of Science degree in Marine Cybernetics at the Norwegian University of Science and Technology(NTNU).

This thesis is a continuation of the project work done during the Fall of 2018, where I investigated the area of nonlinear and robust hybrid control, an area I had limited knowledge about. The project work provided me with better understanding of the concept and to find promising methods to develop further in this master thesis. It is inspired by the ongoing effort to investigate robust hybrid control system methods for autonomous control of ships, a topic that has gained interest in recent years. The work consist of development of a robust hybrid autopilot control design on $\mathbb{S}^1$ for globally stable heading and course control based on hybrid feedback on an $\mathbb{S}^1$ representation of angles. This is a building block towards more advanced path-following control designs for underactuated ships, and eventually autonomous guidance and control of ships in transit. Throughout the process, my supervisors have provided me with valuable insight and discussions on the subject, ideas for implementation, feedback on results and problem scope through regular meetings.

The first months of the work done included development of the control algorithms and simulations on a numerical vessel model for hybrid heading control, velocity vector control and path following. In the last stages of the work, some of the control algorithms were implemented on a physical scale model vessel in the Marine Cybernetics lab(MC-lab) at the Department of Marine Technology.

I would like to thank my supervisor, professor Roger Skjetne at the Department of Marine Technology, NTNU. He has provided me with guidance and resources in understanding the general concepts of nonlinear control. To my co-supervisor Andrew Teel, thanks for discussions and lectures in hybrid systems. I would also like to thank Torgeir Wahl for making sure the equipment at the MC-lab worked as it should. Furthermore Jon Bjørnø for introducing me to the vessel model used for Hardware In the Loop testing and troubleshooting when doing physical experiments at the MC-lab. My lab-partners Edvard Meyer Flaatten, Håvard Løvås and Aksel Knudsen Nordstoga have also been very helpful during the work of this thesis. Lastly, to my family and closest friends, thank you for the support and motivation throughout my years of study.

Trondheim, June 25, 2019

Sondre Haug

....

Sondre Haug

Table of Contents

List of Tables

List of Figures

Abbreviations and Nomenclature

Abbreviations

BODY	Body frame coordinate system
CB	Constant Bearing
CDM	Control Design Model
COLREG	Convention on the International Regulations for Preventing Collisions at Sea
cRIO	National Instrument CompactRIO
CSAD	C/S Inocean Cat I Drillship
DOF	Degree of Freedom
DP	Dynamic Positioning
EBS	Enclosure Based Steering
EC	Environment Complexity
EKF	Extended Kalman Filter
GES	Global Exponentially Stable
GS	Global Stable
HC	Heading Control
HHC	Hybrid Heading Controller
HI	Human Independence
HIL	Hardware In the Loop
IR	Infrared
LAS	Local Asymptotic Stable
LBS	Lookahead-Based Steering
LES	Local Exponential Stable
LOS	Line of Sight
LP	Low-Pass
MC	Mission Complexity
MC-lab	Marine Cybernetics Laboratory
MSS	Marine Systems Simulator toolbox
NED	North, East, Down coordinate system
NPO	Nonlinear Passive Observer
NTNU	Norwegian University of Science and Technology
PFC	Path Following Control
PID	Proportional, Integral, Derivative

PP	Pure Pursuit
PS3	Playstation 3
QTM	Qualisys Track Manager
SISO	Single Input Single Output
SISO	Single-Input-Single-Output
SVM	Simulation Verification Model
TT	Target Tracking
UGAS	Uniform Global Asymptotic Stable
UGES	Uniform Global Exponential Stable
VVC	Velocity Vector Control
WP	Waypoint

Nomenclature

$\mathbf{R}(\psi)$	Rotation matrix
$\mathcal{A}$	Compact set
$\mathcal{A}_0$	Set
α_1, α_2	Parameters in derivation of adaptive control
α_k	Path-tangential angle between waypoints
$\bar{\mathbf{z}}_P$	Unstable critical point along unit circle
β	Crab angle
β_c	Current direction in NED
β_r	Sideslip angle
$\boldsymbol{\alpha}$	Azimuth angles
$\boldsymbol{\Delta}$	Matrix of damping factors
$\boldsymbol{\eta}$	Position and attitude vector
$\boldsymbol{\eta}_d$	Desired position in north, east, yaw
$\boldsymbol{\Gamma}_u$	Diagonal matrix for surge speed controller
$\boldsymbol{\nu}$	Linear and angular velocity vector
$\boldsymbol{\Omega}$	Matrix of natural frequencies
$\boldsymbol{\tau}$	Force, either control force or total sum of forces
$\boldsymbol{\tau}_{current}$	Environmental forces from currents
$\boldsymbol{\tau}_{FF}$	Feedforward term in controller
$\boldsymbol{\tau}_{PID}$	Control force from PID-controller
$\boldsymbol{\tau}_{wave}$	Environmental forces from waves
$\boldsymbol{\tau}_{wind}$	Environmental forces from wind
$\boldsymbol{\theta}$	Estimation matrix for adaptive control
$\boldsymbol{\upsilon}$	BODY frame linear velocities
$\boldsymbol{\upsilon}_c$	Ocean current velocity vector in BODY frame
$\boldsymbol{\upsilon}_r$	Relative BODY frame velocitiy vector
$\boldsymbol{\varphi}$	State dependent vector for adaptive control
C, C_1, C_2	Flow set
χ	Course angle
χ_d	Desired course
χ_p	Path-tangential angle

χ_r	Velocity path relative angle
χ_t	Course of target vessel
$\mathscr{C}$	Class of controls on $\mathbb{S}^1$
$\mathcal{D}, \mathcal{D}_1, \mathcal{D}_2$	Jump set
δ	Rudder angle or synergy gap
$\Delta_{\tilde{p}}$	Gain that affects the transient interceptor-target rendezvous behaviour
Δ_{CB}	Gain to affect the rendezvous behaviour towards the target vessel for constant bearing guidance
Δ_{LBS}	Lookahead distance
$\dot{p}_d$	Desired velocity vector
$\mathcal{E}_0$	Set
$\mathbf{e}_1$	Unit vector in x/1-direction
ϵ	Minimum surge speed
ϵ_d	Desired relative along and cross-track position from a target
ϵ_t, ϵ_n	Along and cross track error
$\mathbf{e}_2$	Unit vector in y/2-direction
Γ_1, Γ_2	Adaption gain matrix for hybrid heading control backstepping
γ_1, γ_2	Adaption gains
$\mathcal{H}$	Hybrid system or hybrid tuple
κ	Stabilizing term / virtual control
$\kappa_{00}, \kappa_{01}, \kappa_{02}, \kappa_{03}, \kappa_{\mathcal{T}_1}, \kappa_{\mathcal{T}_2}$	Virtual controls
λ	Constant in potential function
λ_{max}	Maximum eigenvalue
$\mathcal{M}$	Minimum function for potential functions
$\mathbf{C}(\boldsymbol{\upsilon})$	Coriolis matrix
$\mathbf{D}(\boldsymbol{\upsilon})$	Damping matrix
$\mathbf{D}_L$	Linear damping matrix
$\mathbf{D}_{NL}(\boldsymbol{\upsilon}_r)$	Non-Linear damping matrix
$\mathbf{g}(\boldsymbol{\eta})$	restoring forces matrix
$\mathbf{g}_0$	Stationary resoring forces
$\mathbf{J}(\boldsymbol{\eta})$	Transformation matrix
$\mathbf{K}$	Diagonal force coefficients for thrust allocation
$\mathbf{K}_p, \mathbf{K}_i, \mathbf{K}_d$	Gain matrices for PID controller
$\mathbf{M}$	Mass matrix
$\mathbf{M}_A$	Hydrodynamic added mass matrix
$\mathbf{M}_{RB}$	Rigid body mass matrix
$\mathbf{p}^n$	Position in North and East
$\mathbf{p}_k^n$	Position of waypoint k
$\mathbf{r}^n$	Velocity reference setpoint
$\mathbf{T}(\boldsymbol{\alpha})$	Thrust configuration matrix
$\mathbf{u}$	Vector of control inputs for each thruster
$\mathbf{y}_d$	Desired output
C^0, C^1, C^3, C^T	Generated paths which are continuous and 0, 1, 3 and T times differentiable

μ	Upper bound of synergy gap
$\mu_{\mathcal{W}}$	Weak synergy gap maximum
∇	Gradient operator
∇_z	Gradient operator
ν_c^b	Current velocity expressed in BODY
ν_c^n	Current velocity expressed in NED
ν_r	Relative velocity in BODY
ω	Control or frequency
ω_β	Angular rate of crab angle
ω_a	Angular rate for an angle a
ω_b	Bandwidth / Angular rate for an angle b
ω_n	Natural frequency
$\omega_{\dot{p}_d}$	Desired turning rate from desired velocity vector
ω_{n_r}	Natural frequency in turning rate
ω_{n_u}	Natural frequency in surge speed
Φ	Exponential map function
$\phi_0, \phi_1, \psi_0, \psi_1$	State space functions on $\mathbb{S}^1$
$\mathscr{P}$	Class of potential functions on $\mathbb{S}^1$
ψ	Heading
ψ_d	Desired heading
ρ	Water density
$\sigma(q)$	Unit vector in direction q
$\sigma_1(\boldsymbol{v}_r), \sigma_2(\boldsymbol{v}_r), \sigma_3(\boldsymbol{v}_r)$	Compressed functions to describe the dynamical equations of a ships' motion
$\sigma_{1,\delta}(\boldsymbol{v}_r), \sigma_{21,\delta}(\boldsymbol{v}_r), \sigma_{22,\delta}(\boldsymbol{v}_r), \sigma_{31,\delta}(\boldsymbol{v}_r), \sigma_{32,\delta}(\boldsymbol{v}_r)$	Compressed functions to describe the dynamical equations of a ships' motion when controlled with the rudder angle
$\mathbb{S}^1$	Set of unit vectors along unit circle
$\mathcal{T}$	Global diffeomorphism
$\mathcal{T}_q$	Indexed diffeomorphism
τ_u, τ_v, τ_r	Control forces in surge, sway and yaw
$\tilde{\boldsymbol{\eta}}$	Error in position
$\tilde{\boldsymbol{\theta}}$	Estimate error in surge speed controller
$\tilde{\nu}$	Error in velocities
$\tilde{p}$	Error of smooth switch p
Υ_2	Error in hybrid heading control backstepping design
$\varphi_1, \varphi_2, \varphi_3, \varphi_4$	State dependent adaptive control functions
$\vartheta(z)$	Vector with virtual controls
ξ	State vector
ζ	Damping factor
A	Linear system matrix
b	Linear system result vector
B, D, T	Breadth, Debdth, Freeboard
$b_{11}, b_{22}, b_{23}, b_{32}, b_{33}$	Combined constants on how the forces in surge, sway and yaw affects the response

$c_{A,13}, c_{A,23}$	Coriolis matrix functions
D	Propeller diameter
$d_{11,NL}, d_{22,NL}, d_{23,NL}, d_{32,NL}, d_{33,NL}$	Non-linear damping matrix functions
E	Hybrid time domain
e	Cross-track error
e_u	Error in surge speed controller
$e_{k,x}(p^n), e_{k,y}(p^n)$	Along and crosstrack distance
$g(z)$	Setvalues mapping function
H_C	Heading control transfer function
H_N	Nomoto model transfer function
I_z	Second moment of inertia about the z-axis
J	Jacobian or matrix for $\mathbb{S}^1$-manipulations
K	Nomoto gain
K, M, N	Moment Forces in BODY frame roll, pitch and yaw
k_1, k_2	Constants in the design of hybrid heading control
K_2, K_3, K_p	Gains for hybrid heading control
K_Q, K_T	Thrust coefficients
K_{pu}	Gain for surge speed controller
L	Constant in potential function
Lpp	Length between perpendiculars
m	Mass
$m_{11}, m_{22}, m_{33}, m_{23}$	Mass matrix coefficients
n	Propeller shaft speed
p	Smooth logic mode signal
p, q, r	Angular velocities in roll, pitch and yaw
P_1, P_2, P_{00}, P_{01}	Potential functions
p_d^s	First s-derivative of $p_d(s)$
q	Logic mode
q_0, q_f	Initial and final logic mode at the start and end of a simulation
Q_a	Obtained torque from thruster
R	Rotation matrix
R_k, R_{k+1}	Circle of acceptance for waypoint switching
R_{EBS}	Enclosure Based Steering enclosure radius
R_{LBS}	Lookahead distance
r_{ref}	Setpoint yaw rate
S	Matrix for $\mathbb{S}^1$ manipulations
s	Laplace variable / continuous function for path following / along-track error
$SO(2)$	Set of rotation matrices in $\mathbb{R}^2$
T	Time constant
T_a	Obtained thrust from thruster
U	Speed over ground
u, v, w	Linear velocities in surge, sway and heave
u_0, v_0, r_0	Initial velocities when starting simulations

U_d	Desired speed over ground
u_d	Desired surge speed
U_p	Desired speed along path
U_r	Relative speed
u_r, v_r	Relative velocities in surge and sway
U_t	Speed over ground of target vessel
$U_{a,max}$	Maximum approaching speed
$u_{r,0}, v_{r,0}$	Initial relative velocities when starting simulations
u_{ref}	Setpoint in surge speed
$v(z, p, q)$	Function of the derivative of the smooth switching signal p
$V_0(z, q), V_1(z, q)$	Lyapunov functions on $\mathbb{S}^1$
V_1, V_2	Lyapunov functions
V_c	Ocean current speed
X, Y, Z	Forces in BODY frame surge, sway and heave
x_g	Center of the ship along its x-axis
$X_{\dot{u}}, Y_{\dot{v}}, Y_{\dot{r}}, N_{\dot{v}}, N_{\dot{r}}$	Hydrodynamic added mass coefficients
x_{los}, y_{los}	Line of sight position along path
Y_δ, N_δ	Gains that describes how the sway and yaw forces relates to the rudder angle
z	A vector on $\mathbb{S}^1$ or the heading error represented on $\mathbb{S}^1$
z^χ	Course angle expressed on $\mathbb{S}^1$
z^a	$\mathbb{S}^1$ representation of an angle a
z^{β_c}	Current angle expressed on $\mathbb{S}^1$
z^{β_r}	Sideslip angle expressed on $\mathbb{S}^1$
z^{χ_k}	Path tangential angle between waypoints
z_1, z_2	The first and second value of an angle z on $\mathbb{S}^1$
z_x^β, z_y^β	x and y component of crab angle expressed on $\mathbb{S}^1$
$z_{EBS}^{\chi_d}$	Desired course for Enclosure Based Steering expressed on $\mathbb{S}^1$
$z_{LBS}^{\chi_d}$	Desired course for Lookahead Based Steering expressed on $\mathbb{S}^1$
$z_{PF}^{\chi_d}$	Desired course for Path Following expressed on $\mathbb{S}^1$
$z_{PF}^{\chi_d}$	Desired course for Target Tracking expressed on $\mathbb{S}^1$

Chapter 1

Introduction

1.1 Objective

The developments of control systems started back in the 19th century, and is now an important part of many systems such as cars, aircrafts and marine vessels. The control algorithms gets more and more complex, while giving increased accuracy and reliability. For marine vessels, the most important control systems are dynamic positioning and autopilot. During the last years the development of autonomous vessels is soon to become a reality. This demands even more robust systems, both in terms of decision making, but also ensuring the vessel behave the way we want it to. A vessel is equipped with numerous sensors that together provide information that the control system reacts on. These sensors might have different standards for the format of the information, and a robust control system must process these data robustly to handle imperfections.

Autopilots for ships are based on control of a yaw angle typically defined in the $\pm$ 180 degree range. Using this interval of the reals to constrain the heading within this interval causes several numerical issues, such as different devices, angular mapping and measurement noise. This motivates for a way to handle these effects robustly such that it does not compromise the safety and reliability of the control system as a whole.

This thesis will discuss algorithms to cope with these effects, and analyze the methods in terms of stability and equilibria. The proposed algorithms will be tested on dynamical models of the Norwegian University of Science and Technology(NTNU)s vessel model C/S Inocean Cat I Drillship(CSAD), as well as physical experiments.

1.2 Scope and Delimitations

This thesis will focus on applying robust hybrid control technologies that has been proposed in the later years, and adapt them to a 3-Degree of freedom(DOF) ship model. The hybrid concepts will be used to control the heading of a ship both without and with the influence of ocean currents in a robust manner. This thesis will look into how the hybrid formulation affects the control in Dynamic Positioning(DP), path following and maneuvering operations. The work will be separated into seven main parts:

- Perform a background study of relevant dynamic models of ships, maneuvering models, guidance systems, autonomous systems and hybrid dynamical systems.
- Formulate the 1DOF Heading Control(HC) problem with a control design model(CDM) reformulated on $\mathbb{S}^1$ based on the work done in Mayhew and Teel (2010) with on several potential functions.
- Design a hybrid heading controller (HHC) with backstepping according to Mayhew et al. (2011) .
- Formulate the 2DOF Velocity Vector Control(VVC) problem including disturbances and extend the HHC with an adaptive surge controller to solve the VVC problem to achieve global stability.
- Extend the VVC problem into a Path-Following Control(PFC) problem, and present path generation methods and Line-of-Sight(LOS) guidance that ensures convergence to and following of a path including current compensation.
- Carry out Hardware-in-the-Loop(HIL) tests to prepare the control algorithms to be tested on CSAD at the MC-lab.
- Implement and test the control design on the scale model of CSAD at the MC-lab.

1.3 Outline of the Thesis

The rest of this thesis will be organized as follows:

Chapter 2: Describes the kinetics and kinematics of vessels in 6 and 3 DOFs. Methods for Autopilot control designs are presented, with references to previous work on DP, course and speed control, path following and target tracking. Some specification on autonomous marine control systems are presented, with different axis of complexity.

Chapter 3: Study on hybrid dynamical systems and control, where notation from professor Andrew Teel is introduced on hybrid systems and control on $\mathbb{S}^1$. An example showing a simple point stabilization problem in $\mathbb{S}^1$ is presented, which in general is the core theory behind this thesis. Lastly, different potential functions for hybrid control on $\mathbb{S}^1$ systems with synergistic Lyapunov functions and backstepping are analyzed, tested and discussed in terms of stability and equilibria.

Chapter 4: Describes the simulations and experimental setup, i.e how the numerical model of CSAD is implemented in MATLAB/Simulink. In addition, the procedure for HIL testing is presented, as well as some notes on physical experiments in the Marine Cybernetics(MC)-lab.

Chapter 5: Presents and solves the HC problem. The derivations from Chapter 3 is applied on a 3-DOF model of CSAD, and some different cases are shown. In addition, test results from physical experiments are presented.

Chapter 6: Presents and solves the VVC problem. An $\mathbb{S}^1$ formulation of angles and current is presented, and some test scenarios are shown to illustrate the robustness of the controller.

Chapter 7: Presents and solves the PFC problem. Different path generation techniques are shown and combined with LOS guidance for both straight and curved paths. The combined guidance and control are tested through some different scenarios, both with and without the influence of current.

Chapter 8: Concludes the thesis and proposes further work.

Appendix A: Presents the numerical values for the vessel model of CSAD used in simulations, in addition to some expressions of differentials not suited to fit in the main part of this thesis.

Appendix B: Provides a QR code that links to a video showing the experiments at the MC-lab

Chapter 2

Background

In this section, background and definitions for mathematical modelling, control, guidance and reference models are presented. Most of the study was conducted the fall of 2018 for the author's project thesis; Haug (2018).

2.1 Dynamical Models of Ships

A dynamic model represents the behaviour of an object over time when exposed to forces. It is used where the object's behaviour is best described as a set of states that occur in a defined sequence. Hence, a dynamical model of a ship is the combined kinematics(geometry of motion) and kinetics(how forces create motion).

2.1.1 Ship Dynamics

The ship dynamics can be presented in a compact 6-DOF matrix-vector as:

$$\begin{aligned} \dot{\boldsymbol{\eta}} &= \mathbf{J}(\boldsymbol{\eta})\boldsymbol{\upsilon} \\ \mathbf{M}\dot{\boldsymbol{\upsilon}} + \mathbf{C}(\boldsymbol{\upsilon})\boldsymbol{\upsilon} + \mathbf{D}(\boldsymbol{\upsilon})\boldsymbol{\upsilon} + \mathbf{g}(\boldsymbol{\eta}) + \mathbf{g}_0 &= \boldsymbol{\tau} + \boldsymbol{\tau}_{wind} + \boldsymbol{\tau}_{wave} + \boldsymbol{\tau}_{current} \end{aligned} \tag{2.1}$$

Where $\boldsymbol{\eta}, \boldsymbol{\upsilon} \in \mathbb{R}^6$ are vectors of generalized North-East-Down(NED)-position({n}) and angles $\boldsymbol{\eta} = [N, E, D, \phi, \theta, \psi]^\top$ and BODY({b})-velocities $\boldsymbol{\upsilon} = [u, v, w, p, q, r]^\top$, $\mathbf{J}(\boldsymbol{\eta}) \in \mathbb{R}^{6x6}$ is the Euler Angle Transformation matrix, converting {b}-velocities to {n}-velocities, $\mathbf{M} \in \mathbb{R}^{6x6}$ the system inertia matrix, including Mass, added mass and second moment of inertia, $\mathbf{C}(\boldsymbol{\upsilon}) \in \mathbb{R}^{6x6}$ is the Coriolis and centripetal matrix, due to the rotation of body frame about {n} frame, $\mathbf{D}(\boldsymbol{\upsilon}) \in \mathbb{R}^{6x6}$ is the damping matrix, $\mathbf{g}(\boldsymbol{\eta}) \in \mathbb{R}^6$ is the vector of gravitational and buoyancy forces, $\mathbf{g}_0 \in \mathbb{R}^6$ is the vector used for pretrimming (ballast control), $\boldsymbol{\tau} = [X, Y, Z, K, M, N]^\top \in \mathbb{R}^6$ is the vector of control inputs, and $\boldsymbol{\tau}_{wind} \in \mathbb{R}^6$, $\boldsymbol{\tau}_{wave} \in \mathbb{R}^6$ and $\boldsymbol{\tau}_{current} \in \mathbb{R}^6$ are the vector of environmental loads. For more details; see Fossen (2011).

2.1.2 Maneuvering Models

A 3-DOF system is sufficient to create an autopilot design, assuming the motions in roll, heave and pitch are small. The states that describes the horizontal motion can be extracted from the 6-DOF model in (2.1), i.e surge, sway and yaw. Hence, the state vectors describing the 3-DOF systems are $\boldsymbol{\eta} = [N, E, \psi]^\top \in \mathbb{R}^3$ and $\boldsymbol{\upsilon} = [u, v, r]^\top \in \mathbb{R}^3$. Introducing relative velocity $\boldsymbol{\upsilon}_r = \boldsymbol{\upsilon} - \boldsymbol{\upsilon}_c \in \mathbb{R}^3$, where $\boldsymbol{\upsilon}_c \in \mathbb{R}^3$ is the current velocity expressed in body frame, gives (2.2):

$$\dot{\boldsymbol{\eta}} = \mathbf{R}(\psi)\boldsymbol{\upsilon} \tag{2.2a}$$

$$\mathbf{M}\dot{\boldsymbol{\upsilon}}_r + \mathbf{C}(\boldsymbol{\upsilon}_r)\boldsymbol{\upsilon}_r + \mathbf{D}(\boldsymbol{\upsilon}_r)\boldsymbol{\upsilon}_r = \boldsymbol{\tau} \tag{2.2b}$$

Where $\mathbf{R}(\psi) \in SO(3)$, $\mathbf{M} = \mathbf{M}_A + \mathbf{M}_{RB} \in \mathbb{R}^{3x3}$, $\mathbf{C}(\boldsymbol{\upsilon}_r) \in \mathbb{R}^{3x3}$, $\mathbf{D}(\boldsymbol{\upsilon}_r) \in \mathbb{R}^{3x3}$, and $\boldsymbol{\tau} \in \mathbb{R}^3$. The matrices $\mathbf{R}(\psi)$, $\mathbf{M}_{RB}$ and $\mathbf{M}_A$ are defined as follows (Fossen, 2011):

$$\mathbf{R}(\psi) = \begin{bmatrix} \cos(\psi) & -\sin(\psi) & 0 \\ \sin(\psi) & \cos(\psi) & 0 \\ 0 & 0 & 1 \end{bmatrix}, \qquad \mathbf{M}_{RB} = \begin{bmatrix} m & 0 & 0 \\ 0 & m & mx_g \\ 0 & mx_g & I_z \end{bmatrix}, \qquad \mathbf{M}_A = \begin{bmatrix} -X_{\dot{u}} & 0 & 0 \\ 0 & -Y_{\dot{v}} & -Y_{\dot{r}} \\ 0 & -N_{\dot{v}} & -N_{\dot{r}} \end{bmatrix} \tag{2.3}$$

The damping matrix $\boldsymbol{D}(\boldsymbol{\upsilon}_r)$ is defined as a linear(L) term and an non-linear(NL) term:

$$\mathbf{D}(\boldsymbol{\upsilon}_r) = \mathbf{D}_L + \mathbf{D}_{NL}(\boldsymbol{\upsilon}_r) = \begin{bmatrix} d_{11}(\boldsymbol{\upsilon}_r) & 0 & 0 \\ 0 & d_{22}(\boldsymbol{\upsilon}_r) & d_{23}(\boldsymbol{\upsilon}_r) \\ 0 & d_{32}(\boldsymbol{\upsilon}_r) & d_{33}(\boldsymbol{\upsilon}_r) \end{bmatrix} \tag{2.4}$$

with

$$\mathbf{D}_L = \begin{bmatrix} -X_u & 0 & 0 \\ 0 & -Y_v & -Y_r \\ 0 & -N_v & -N_r \end{bmatrix}, \qquad \mathbf{D}_{NL}(\boldsymbol{\upsilon}_r) = \begin{bmatrix} d_{11,NL}(\boldsymbol{\upsilon}_r) & 0 & 0 \\ 0 & d_{22,NL}(\boldsymbol{\upsilon}_r) & d_{23,NL}(\boldsymbol{\upsilon}_r) \\ 0 & d_{32,NL}(\boldsymbol{\upsilon}_r) & d_{33,NL}(\boldsymbol{\upsilon}_r) \end{bmatrix} \tag{2.5}$$

where the NL damping forces are calculated according to (2.6):

$$d_{11,NL}(\boldsymbol{\upsilon}_r) = -X_{|u|u}|u_r| - X_{uuu}u_r^2 \tag{2.6a}$$

$$d_{22,NL}(\boldsymbol{\upsilon}_r) = -Y_{|v|v}|v_r| - Y_{|r|v}|r| - Y_{vvv}v_r^2 \tag{2.6b}$$

$$d_{23,NL}(\boldsymbol{\upsilon}_r) = -Y_{|v|r}|v_r| - Y_{|r|r}|r| - Y_{rrr}r^2 - Y_{ur}u_r \tag{2.6c}$$

$$d_{32,NL}(\boldsymbol{\upsilon}_r) = -N_{|v|v}|v_r| - N_{|r|v}|r| - N_{vvv}v_r^2 - N_{uv}u_r \tag{2.6d}$$

$$d_{33,NL}(\boldsymbol{\upsilon}_r) = -N_{|r|r}|r| - N_{|v|r}|v_r| - N_{rrr}r^2 - N_{ur}u_r \tag{2.6e}$$

With the *munk moment*:

$$Y_{ur} = -X_{\dot{u}} \tag{2.7}$$

$$N_{uv} = -(Y_{\dot{v}} - X_{\dot{u}}) \tag{2.8}$$

$$N_{ur} = -Y_{\dot{r}} \tag{2.9}$$

The Coriolis matrix $\boldsymbol{C}(\boldsymbol{\upsilon}_r)$ are calculated according to (2.10):

$$\mathbf{C}(\boldsymbol{v}_r) = \mathbf{C}_{RB}(\boldsymbol{v}_r) + \mathbf{C}_A(\boldsymbol{v}_r) \tag{2.10}$$

$$\mathbf{C}_{RB}(\boldsymbol{v}_r) = \begin{bmatrix} 0 & 0 & -m(x_g r + v_r) \\ 0 & 0 & mu_r \\ m(x_g r + v_r) & -mu_r & 0 \end{bmatrix}, \quad \mathbf{C}_A(\boldsymbol{v}_r) = \begin{bmatrix} 0 & 0 & c_{A,13}(\boldsymbol{v}_r) \\ 0 & 0 & c_{A,23}(\boldsymbol{v}_r) \\ -c_{A,13}(\boldsymbol{v}_r) & -c_{A,23}(\boldsymbol{v}_r) & 0 \end{bmatrix} \tag{2.11}$$

$$c_{A,13}(\boldsymbol{v}_r) = Y_{\dot{v}} v_r + Y_{\dot{r}} r, \qquad c_{A,23}(\boldsymbol{v}_r) = -X_{\dot{u}} u_r \tag{2.12}$$

Then, by solving for $\dot{\boldsymbol{v}}_r$ we obtain:

$$\dot{\boldsymbol{v}}_r = \mathbf{M}^{-1} \left(\tau - \mathbf{C}(\boldsymbol{v}_r)\boldsymbol{v}_r - \mathbf{D}(\boldsymbol{v}_r)\boldsymbol{v}_r\right) \tag{2.13}$$

with

$$\mathbf{M}^{-1} = \begin{bmatrix} \frac{1}{m_{11}} & 0 & 0 \\ 0 & -\frac{m_{33}}{m_{23}^2 - m_{22}m_{33}} & \frac{m_{23}}{m_{23}^2 - m_{22}m_{33}} \\ 0 & \frac{m_{23}}{m_{23}^2 - m_{22}m_{33}} & -\frac{m_{22}}{m_{23}^2 - m_{22}m_{33}} \end{bmatrix} \tag{2.14}$$

which from Skjetne (2018) by defining

$$\sigma_1(\boldsymbol{v}_r) := -\frac{d_{11}(\boldsymbol{v}_r)}{m_{11}} u_r + \frac{m_{22}v_r + m_{23}r}{m_{11}} r \tag{2.15}$$

$$\begin{aligned}\sigma_2(\boldsymbol{v}_r) := &-\frac{d_{22}(\boldsymbol{v}_r)m_{33} - d_{32}(\boldsymbol{v}_r)m_{23} - m_{23}\left(m_{22} - m_{11}\right)u_r}{m_{22}m_{33} - m_{23}^2} v_r \\ &+ \frac{d_{33}(\boldsymbol{v}_r)m_{23} - d_{23}(\boldsymbol{v}_r)m_{33} + \left(m_{11}m_{33} - m_{23}^2\right)u_r}{m_{22}m_{33} - m_{23}^2} r\end{aligned} \tag{2.16}$$

$$\begin{aligned}\sigma_3(\boldsymbol{v}_r) := &\frac{d_{22}(\boldsymbol{v}_r)m_{23} - d_{32}(\boldsymbol{v}_r)m_{22} - m_{22}\left(m_{22} - m_{11}\right)u_r}{m_{22}m_{33} - m_{23}^2} v_r \\ &- \frac{\left(d_{33}(\boldsymbol{v}_r)m_{22} - d_{23}(\boldsymbol{v}_r)m_{23}\right) + m_{23}\left(m_{22} - m_{11}\right)u_r}{m_{22}m_{33} - m_{23}^2} r\end{aligned} \tag{2.17}$$

$$b_{11} := \frac{1}{m_{11}} \tag{2.18}$$

$$b_{22} := \frac{m_{33}}{m_{22}m_{33} - m_{23}^2}, \qquad b_{23} := \frac{-m_{23}}{m_{22}m_{33} - m_{23}^2} \tag{2.19}$$

$$b_{32} := \frac{-m_{23}}{m_{22}m_{33} - m_{23}^2}, \qquad b_{33} := \frac{m_{22}}{m_{22}m_{33} - m_{23}^2}, \tag{2.20}$$

results in:

$$\dot{u}_r = \sigma_1(\boldsymbol{v}_r) + b_{11}\tau_u \tag{2.21a}$$

$$\dot{v}_r = \sigma_2(\boldsymbol{v}_r) + b_{22}\tau_v + b_{23}\tau_r \tag{2.21b}$$

$$\dot{r} = \sigma_3(\boldsymbol{v}_r) + b_{32}\tau_v + b_{33}\tau_r \tag{2.21c}$$

For an underactuated ship, the main issue is how to handle the sway dynamics. We can see from (2.21b) that a force in yaw induces a velocity in sway. We can use the control allocation for a fully actuated vessel to emulate an underactuated vessel in sway such that $b_{22}\tau_v + b_{23}\tau_r = 0$. This is obtained by constraining $\tau_v = -\frac{b_{23}}{b_{22}}\tau_r = \frac{m_{23}}{m_{33}}\tau_r$ in the control allocation such that

$$\dot{u}_r = \sigma_1(\boldsymbol{v}_r) + \frac{1}{m_{11}}\tau_u \tag{2.22a}$$

$$\dot{v}_r = \sigma_2(\boldsymbol{v}_r) \tag{2.22b}$$

$$\dot{r} = \sigma_3(\boldsymbol{v}_r) + \frac{1}{m_{33}}\tau_r \tag{2.22c}$$

which is the model the simulations will be based on.

Rendering sway underactuated by Rudder steering

If the dynamic model is derived with an arbitrary center along the vessel's body axis, the rudder angle δ will typically generate sway force. According to Tzeng (1998), by transforming the states to the pivot point of the vessel, you can eliminate the the influence δ has on the sway dynamics. This can be done by locating the centre of the vessel's body frame at an appropriate arm x_g relative to the centre of gravity, and suppose:

$$\begin{bmatrix} \tau_u \\ \tau_v \\ \tau_r \end{bmatrix} = \begin{bmatrix} \tau_u \\ Y_\delta \delta \\ N_\delta \delta \end{bmatrix} \tag{2.23}$$

which inserted in (2.21) gives:

$$\begin{bmatrix} \dot{u}_r \\ \dot{v}_r \\ \dot{r} \end{bmatrix} = \begin{bmatrix} -\frac{d_{11}}{m_{11}}u_r + \frac{m_{22}v_r + m_{23}r}{m_{11}}r \\ \frac{(m_{11}-m_{22})m_{23}v_r - \left(m_{23}^2 - m_{11}m_{33}\right)r}{m_{23}^2 - m_{22}m_{33}}u_r + \frac{(d_{22}m_{33}-d_{32}m_{23})v_r + (d_{23}m_{33}-d_{33}m_{23})r}{m_{23}^2 - m_{22}m_{33}} \\ \frac{(m_{22}-m_{11})(m_{23}r + m_{22}v_r)}{m_{23}^2 - m_{22}m_{33}}u_r - \frac{(d_{23}m_{23}-d_{33}m_{22})r + (d_{22}m_{23}-d_{32}m_{22})v_r}{m_{23}^2 - m_{22}m_{33}} \end{bmatrix} + \begin{bmatrix} \frac{1}{m_{11}}\tau_u \\ \frac{m_{23}N_\delta - m_{33}Y_\delta}{m_{23}^2 - m_{22}m_{33}}\delta \\ \frac{m_{23}Y_\delta - m_{22}N_\delta}{m_{23}^2 - m_{22}m_{33}}\delta \end{bmatrix} \tag{2.24}$$

where we notice that if we want to set actuation in sway to zero, we use

$$m_{23}N_\delta - m_{33}Y_\delta = (mx_g - Y_{\dot{r}})N_\delta - (I_z - N_{\dot{r}})\,Y_\delta = 0 \tag{2.25}$$

$$m_{23} = \frac{Y_\delta}{N_\delta}m_{33} \tag{2.26}$$

$$x_g = \frac{Y_{\dot{r}}N_\delta + (I_z - N_{\dot{r}})\,Y_\delta}{mN_\delta} = \frac{Y_{\dot{r}}}{m} + \frac{(I_z - N_{\dot{r}})\,Y_\delta}{mN_\delta} \tag{2.27}$$

By this choise of m_{23} (and x_g) we get for the 3rd component in the input vector of (2.24),

$$\frac{\frac{Y_\delta}{N_\delta}Y_\delta m_{33} - m_{22}N_\delta}{\left(\frac{Y_\delta}{N_\delta}\right)^2 m_{33}^2 - m_{22}m_{33}} = \frac{\frac{Y_\delta^2}{N_\delta}m_{33} - m_{22}N_\delta}{\frac{Y_\delta^2}{N_\delta^2}m_{33}^2 - m_{22}m_{33}} = \frac{N_\delta^2\left(\frac{Y_\delta^2}{N_\delta}m_{33} - m_{22}N_\delta\right)}{N_\delta^2\left(\frac{Y_\delta^2}{N_\delta^2}m_{33}^2 - m_{22}m_{33}\right)} \tag{2.28}$$

$$= \frac{\left(m_{33}Y_\delta^2 - m_{22}N_\delta^2\right)N_\delta}{m_{33}\left(m_{33}Y_\delta^2 - m_{22}N_\delta^2\right)} = \frac{N_\delta}{m_{33}}. \tag{2.29}$$

Moreover, we get

$$\sigma_{1,\delta}(\boldsymbol{v}_r) = -\frac{d_{11}(\boldsymbol{v}_r)}{m_{11}}u_r + \frac{m_{22}r}{m_{11}}v_r + \frac{Y_\delta m_{33}}{N_\delta m_{11}}r^2 \tag{2.30}$$

$$\sigma_{21,\delta}(\boldsymbol{v}_r) = \frac{-\left(d_{32}(\boldsymbol{v}_r)Y_\delta - d_{22}(\boldsymbol{v}_r)N_\delta\right)N_\delta - \left(m_{22} - m_{11}\right)Y_\delta N_\delta u_r}{m_{33}Y_\delta^2 - m_{22}N_\delta^2} \tag{2.31}$$

$$\sigma_{22,\delta}(\boldsymbol{v}_r) = \frac{\left(d_{23}(\boldsymbol{v}_r)N_\delta - d_{33}(\boldsymbol{v}_r)Y_\delta\right)N_\delta - \left(m_{33}Y_\delta^2 - m_{11}N_\delta^2\right)u_r}{m_{33}Y_\delta^2 - m_{22}N_\delta^2} \tag{2.32}$$

$$\sigma_{31,\delta}(\boldsymbol{v}_r) = \frac{m_{22}\left(m_{22} - m_{11}\right)N_\delta^2 u_r - \left(m_{33}Y_\delta N_\delta d_{22}(\boldsymbol{v}_r) - m_{22}N_\delta^2 d_{32}(\boldsymbol{v}_r)\right)}{m_{33}\left(m_{33}Y_\delta^2 - m_{22}N_\delta^2\right)} \tag{2.33}$$

$$\sigma_{32,\delta}(\boldsymbol{v}_r) = \frac{m_{33}\left(m_{22} - m_{11}\right)Y_\delta N_\delta u_r - \left(m_{33}Y_\delta N_\delta d_{23}(\boldsymbol{v}_r) - m_{22}N_\delta^2 d_{33}(\boldsymbol{v}_r)\right)}{m_{33}\left(m_{33}Y_\delta^2 - m_{22}N_\delta^2\right)} \tag{2.34}$$

resulting in

$$\dot{u}_r = \sigma_{1,\delta}(\boldsymbol{v}_r) + \frac{1}{m_{11}}\tau_u \tag{2.35a}$$

$$\dot{v}_r = \sigma_{21,\delta}(\boldsymbol{v}_r)v_r + \sigma_{22,\delta}(\boldsymbol{v}_r)r \tag{2.35b}$$

$$\dot{r} = \sigma_{31,\delta}(\boldsymbol{v}_r)v_r + \sigma_{32,\delta}(\boldsymbol{v}_r)r + \frac{N_\delta}{m_{33}}\delta \tag{2.35c}$$

where $\tau_r = N_\delta\delta$. Than, assuming the numerical values of N_δ and Y_δ are known, we can render sway underactuated.

2.2 Dynamic Positioning Control Designs

Dynamic Positioning is a computer controlled system to automatically maintain a vessel's position with its own controls, i.e its propellers and thrusters. By the aid of position reference sensors, sensors that measures environmental disturbances, motion sensors, gyroscope, compass etc., a DP system uses this information to compensate for these disturbances and motions by allocating thrust to maintain its position at sea. The computer controlled system uses a mathematical model of the vessel that includes information of the estimated loads from the measured disturbances such as wind and current drag, together with the position of the thrusters to calculate the desired output for each thruster. This allows for stationkeeping operation where mooring or anchoring is not feasible due to deep water or restrictions on anchoring nearby seabed installations like pipelines or templates.

A simplified model for Proportional-Integral-Derivative(PID) feedback control for DP application can be performed by choosing a bandwidth ω_b and pole-placement according to Fossen (2011):

$$\omega_n = \frac{1}{\sqrt{1 - 2\zeta^2 + \sqrt{4\zeta^4 - 4\zeta^2 + 2}}}\omega_b \approx \frac{1}{0.64}\omega_b \quad \text{if} \quad \zeta = 1 \tag{2.36a}$$
$$\mathbf{K}_p = \mathbf{M}\omega_n^2 \tag{2.36b}$$
$$\mathbf{K}_d = 2\zeta\omega_n\mathbf{M} - \mathbf{D}_L \tag{2.36c}$$
$$\mathbf{K}_i = \frac{\omega_n}{10}\mathbf{K}_p \tag{2.36d}$$
$$\tilde{\boldsymbol{\eta}} = \boldsymbol{\eta} - \boldsymbol{\eta}_d \tag{2.36e}$$
$$\tilde{\boldsymbol{\upsilon}} = \boldsymbol{\upsilon} - \mathbf{R}(\boldsymbol{\eta})^\top\dot{\boldsymbol{\eta}}_d \tag{2.36f}$$
$$\boldsymbol{\tau}_{PID} = -\mathbf{R}^\top(\boldsymbol{\eta})\mathbf{K}_p\tilde{\boldsymbol{\eta}} - \mathbf{K}_d\tilde{\boldsymbol{\upsilon}} - \mathbf{R}^\top(\boldsymbol{\eta})\mathbf{K}_i\int_0^t \tilde{\boldsymbol{\eta}}(\tau)d\tau \tag{2.36g}$$
$$\boldsymbol{\tau}_{FF} = \mathbf{M}\dot{\upsilon}_d + \mathbf{D}_L\upsilon_d \tag{2.36h}$$
$$\boldsymbol{\tau} = \boldsymbol{\tau}_{PID} + \boldsymbol{\tau}_{FF} \tag{2.36i}$$

Where $\boldsymbol{\tau}$ is the control input to ensure $\tilde{\boldsymbol{\eta}} \rightarrow 0$. The position and attitude reference model $\boldsymbol{\eta}_d$ is typically chosen to be a third order for filtering the steps in the reference(typically set by the operator of the DP system) $\mathbf{r}^n$ by a first order Low-Pass(LP) filter cascaded with a mass-spring-damper system:

$$\frac{\eta_{d_i}}{r_i^n} = \frac{\omega_{n_i}^3}{s^3 + (2\zeta_i + 1)\omega_{n_i}s^2 + (2\zeta_i + 1)\omega_{n_i}^2 s + \omega_{n_i}^3} \tag{2.37}$$

For a vessel to achieve the desired thrust $\boldsymbol{\tau}$, we have the thrust allocation algorithm

$$\boldsymbol{\tau} = \mathbf{T}(\boldsymbol{\alpha})\mathbf{f} = \mathbf{T}(\boldsymbol{\alpha})\mathbf{K}\mathbf{u} \tag{2.38}$$

where $\boldsymbol{\alpha} = [\alpha_1, ..., \alpha_p]^\top \in \mathbb{R}^p$ is a vector of azimuth angles and $\mathbf{T}(\boldsymbol{\alpha}) \in \mathbb{R}^{n\times r}$ is the thrust configuration matrix that describes the geometry of locations of the r actuators. $\mathbf{K} \in \mathbb{R}^{r\times r}$ is a diagonal force coefficient matrix and $\mathbf{u} \in \mathbb{R}^n$ is a vector of control inputs.

2.3 Autopilot Control Designs

In this section, the methods for design of guidance and control systems for marine craft will be described. Guidance represents the basic methodology concerned with the transient motion behaviour associated with the achievement of motion control objectives. Guidance laws can be used to generate a time-varying *trajectory* or a time-invariant *path* reference. Skjetne (2019) describes four different motion control scenarios for ships:

- *Regulation* - Special case where attitude and position are held constant (e.g Dynamic Positioning).
- *Tracking* - Force a system output $\mathbf{y}(t) \in \mathbb{R}^m$ to track a desired output $\mathbf{y}_d(t) \in \mathbb{R}^m$. Can be achieved be generating a reference model with feasible trajectories given the constraints.
- *Path following* - Follow a predefined path independent of time.

- *Maneuvering* - satisfying both a *geometric* and *dynamic* task. The geometric task is defined as forcing an output y to converge to the desired path $y_d(s)$ for a continuous function $s(t)$. The dynamic task is to force $s(t)$, $\dot{s}(t)$ or $\ddot{s}(t)$ to converge to one or more of the time $\tau(t)$, speed $v(s,t)$ or acceleration $a(\dot{s},s,t)$ assignments.

For surface vessels the most common control system is to combine a heading controller and speed controller in order to track the desired path. The following sections will describe the different control strategies when controlling a vessels heading and velocity.

2.3.1 Reference Frames

Fossen (2016) present the ocean triangle in Figure 2.1 and the equations in (2.39). They define course, heading, crab and sideslip angles, as well as the relevant speeds when a vessel is affected by ocean currents. Here, the ships position is defined as $\mathbf{p}^n = [N,E]^\top = [x,y]^\top \in \mathbb{R}^2$ and its derivatives $\dot{x} = \frac{dx}{dt}$ and $\dot{y} = \frac{dy}{dt}$. Note that without current, $\beta = \beta_r$.

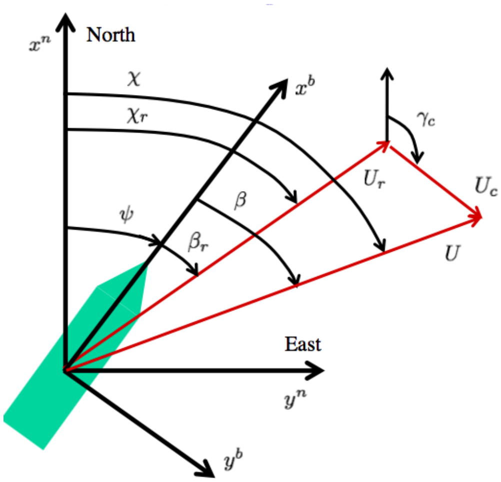

Sideslip angle: $$\beta_r = sin^{-1}\left(\frac{v_r}{U_r}\right) \tag{2.39a}$$

Crab angle: $$\beta := \chi - \psi, \quad \beta = sin^{-1}\left(\frac{v}{U}\right) \tag{2.39b}$$

Course angle: $$\chi := \text{atan2}(\dot{y},\dot{x}) \tag{2.39c}$$

Heading angle: $$\psi \tag{2.39d}$$

Speed over ground: $$U = \sqrt{u^2+v^2}, \quad U = \sqrt{\dot{x}^2+\dot{y}^2} \tag{2.39e}$$

Relative speed $$U_r = \sqrt{{u_r}^2+{v_r}^2} \tag{2.39f}$$

Current speed $$U_c = \sqrt{{u_c}^2+{v_c}^2} \tag{2.39g}$$

Current direction: $$\beta_c \tag{2.39h}$$

Figure 2.1: Reference frames in the horizontal plane. Courtesy: Fossen (2016).

2.3.2 Heading Control

Controlling the heading of a ship is a Single Input Single Output(SISO) control problem, where the rudder is used as actuator for controlling yaw rate, which is integrated in order to obtain heading. The Nomoto model, as first cited in Nomoto and Taguchi (1957), is a natural choice in such a case. There are two main types of Nomoto models for the relation between rudder angle and yaw rate. Both originate from the linearized maneuvering model as shown in (2.2). Picking out the yaw rate r from this model, transforming it to the Laplace plane and integrate to obtain the transfer function for the heading ψ results in the second-order Nomoto model in (2.40):

$$\frac{\psi}{\delta}(s) = \frac{K(1+T_3 s)}{s(1+T_1 s)(1+T_2 s)} \tag{2.40}$$

If the dynamics can be approximated as a first order response, one can define an equivalent time constant $T := T_1 + T_2 - T_3$ to obtain the first-order Nomoto model as shown in (2.41).

$$\frac{\psi}{\delta}(s) = \frac{K}{s(1+Ts)} \tag{2.41}$$

A simple PID-controller can be chosen to control the heading, such that $\lim_{t\to\infty}\tilde{\psi} = 0$ and $\lim_{t\to\infty}\tilde{r} = 0$. The controller can be expressed as in (2.42), using the relationship $\dot{\psi} = r$.

$$\delta_c(t) = -K_p\tilde{\psi}(t) - K_d\tilde{r}(t) - K_i\int_0^t \tilde{\psi}(\tau)d\tau \tag{2.42}$$

Here, the error terms are defined as $\tilde{\psi} := \psi - \psi_d$ and $\tilde{r} := r - r_d$, where ψ_d and r_d are the desired heading and turning rate, respectively. By including an integral term in the controller, this is able to correct for steady-state disturbances and modelling errors. During constant heading hold, current might be treated as a steady-state disturbance. It should however be noted that small errors can be induced by this approach during heading changes when exposed to current.

If we express the transfer function for the controller as H_C and the transfer function of the Nomoto model in (2.40) as H_N we can draw a block diagram for the heading loop as shown in Figure 2.2a. With ocean current, the system is modelled with a constant disturbance d as shown in Figure 2.2b.

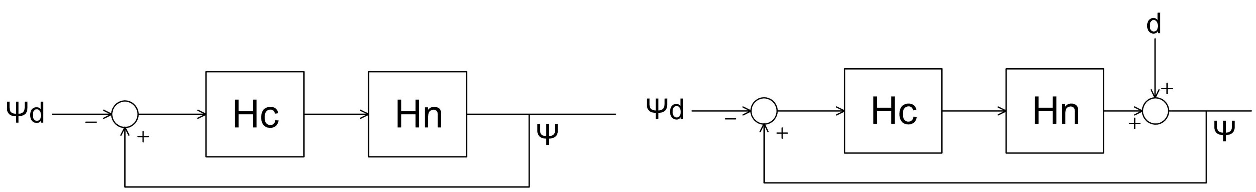

(a) Block diagram of heading hold loop

(b) Block diagram of heading loop with current modelled as a disturbance entering the system after the Nomoto model

Figure 2.2: Block diagrams of heading hold loops

This gives the closed loop transfer function in (2.43), which ensures the heading ψ to converge to the desired heading ψ_d giving $\lim_{t\to\infty}\frac{\psi}{\psi_d} = 1 \implies \lim_{t\to\infty}\psi = \psi_d \implies \lim_{t\to\infty}\tilde{\psi} = 0$.

$$\frac{\psi}{\psi_d}(s) = H_\psi = \frac{-H_C H_N/s}{1 - H_C H_N/s} = \frac{K(K_d s^2 + K_p s + K_i)}{s^3(Ts+1) + K(K_d s^2 + K_p s + K_i)} \tag{2.43}$$

With a step change μ_1 in the disturbance, it can be proven that the heading error $\tilde{\psi}$ still converges towards zero by $\lim_{t\to\infty}\frac{\psi}{d}(t)\mu_1(t) = \lim_{s\to 0} s\frac{\psi}{d}(t)\frac{1}{s} = 0$. It is hereby shown that the controller is able to suppress the effect of a step disturbance entering the feedback loop after the Nomoto model, implying that the effect of constant or slowly varying current will also be suppressed.

This type of controller will be able to control the heading towards a steady value equal to the commanded value, and that it will be able to suppress outer disturbances from modelling errors or constant current. It is thereby not given that it will be able to track a high-frequency time-varying reference signal, or that it will be able to suppress high-frequency disturbances such as quickly varying current (e.g., during a turn, where the BODY-frame current will vary), or wind gusts. In addition, due to the heading ψ, desired heading ψ_d and heading error $\tilde{\psi}$ needs to be disrupted from the point on the circle to the interval $[-\pi, \pi]$, there is no proof for this heading control to be GAS, as there exist more than one equilibrium for the heading error to be zero.

2.3.3 Feedback linearization Speed Control

For a desired surge speed u_d, a speed controller must ensure that the error $\tilde{u} = u - u_d$ will converge towards zero $\lim_{t\to\infty} \tilde{u} = 0$. The controller must be able to withstand external disturbances, such as currents. A proposed method in Fossen (2011) is based on a state feedback linearization using the extracted 1-DOF surge speed maneuvering model in (2.21):

$$\dot{u}_r = -\frac{d_{11}(u_r)}{m_{11}} u_r + \frac{m_{22} r}{m_{11}} v_r + \frac{m_{23}}{m_{11}} r^2 + \frac{1}{m_{11}} \tau_u \tag{2.44}$$

Assuming small relative velocity in sway $v_r \approx 0$, small turning rate $r \approx 0$, slow currents $u_r = u - u_c \approx u$ and neglecting higher order terms such as $X_{uuu} u^2$, the model is simplified to:

$$\dot{u} = \frac{X_u}{m_{11}} u + \frac{X_{|u|u}}{m_{11}} |u| u + \frac{1}{m_{11}} \tau_u \tag{2.45}$$

$$(m - X_{\dot{u}}) \dot{u}_r - X_u u_r - X_{|u|u} |u_r| u_r = \tau_u \tag{2.46}$$

This is dependent on an accurate model, as the nonlinear terms terms can be important, especially at higher speeds. For low speed application, the nonlinear term in this model is often set to zero, but other techniques such as acceleration feedback (Fossen, 2011) by adding nonlinear terms could be chosen. The input to the system is expressed as in (2.47), with the corresponding closed loop transfer function in (2.48).

$$\tau_u(t) = -K_p \tilde{u}(t) - K_i \int_0^t \tilde{u}(\tau) d\tau \Rightarrow H_c(s) = \frac{\tau_1}{\tilde{u}}(s) = -K_p - \frac{K_i}{s} \tag{2.47}$$

$$H_u(s) = \frac{u}{u_d}(s) = \frac{-H_c(s) H_N(s)}{1 - H_c(s) H_N(s)} = \frac{(sK_p + K_i)/(m - X_{\dot{u}})}{s^2 + s(d_1 + K_p)/(m - X_{\dot{u}}) + K_i/(m - X_{\dot{u}})} \tag{2.48}$$

Where $\lim_{t\to\infty} H_u(t) = 1 \implies u \to u_d$. However, the simplifications made in the control design might be significant, and therefore more robust surge speed controller should be designed to account for parametric uncertainties.

Adaptive Backstepping Speed Control

To account for parametric uncertainty in (2.46) and the effect of an unknown current, an adaptive controller for the surge speed can be designed. Inspired by Breivik and Fossen (2007), we can split $\sigma_1(\boldsymbol{v}_r)$ in (2.22a) into a term from the measurable velocities $\boldsymbol{v}$ and leave the effect of the current as an estimate. This gives:

$$
\begin{aligned}
\dot{u}_r &= \sigma_1(\boldsymbol{v}_r) + \frac{1}{m_{11}}\tau_u \\
\dot{u} - \dot{u}_c &= \sigma_1(\boldsymbol{v}) + \boldsymbol{\varphi}(\boldsymbol{v})^\top \boldsymbol{\theta} + \frac{1}{m_{11}}\tau_u
\end{aligned} \tag{2.49}
$$

where $\boldsymbol{\varphi}^\top\boldsymbol{\theta}$ is the effect of the unknown current. Assuming constant current $\dot{u}_c = 0 \implies \dot{u}_r = \dot{u}$ and $u_r = u - u_c$. This leads to

$$
\begin{aligned}
\dot{u} &= \alpha_1(u-u_c) + \alpha_2|u-u_c|(u-u_c) + \sigma_1(\boldsymbol{v}) + \frac{1}{m_{11}}\tau_u \\
&\approx \alpha_1(u-u_c) + \alpha_2(u-u_c)^2 + \sigma_1(\boldsymbol{v}) + \frac{1}{m_{11}}\tau_u \\
&\approx \alpha_1 u + \alpha_2|u|u - \alpha_1 u_c - 2\alpha_2|u|u_c + \alpha_2 u_c^2 + \sigma_1(\boldsymbol{v}) + \frac{1}{m_{11}}\tau_u \\
&= [u, |u|u, |u|, 1]\,[\alpha_1, \alpha_2, -2\alpha_2 u_c, -\alpha_1 u_c - \alpha_2|u_c|u_c]^\top + \sigma_1(\boldsymbol{v}) + \frac{1}{m_{11}}\tau_u \\
&= [\varphi_1, \varphi_2, \varphi_3, \varphi_4]\,[\theta_1, \theta_2, \theta_3, \theta_4]^\top + \sigma_1(\boldsymbol{v}) + \frac{1}{m_{11}}\tau_u \\
&= \boldsymbol{\varphi}^\top\boldsymbol{\theta} + \sigma_1(\boldsymbol{v}) + \frac{1}{m_{11}}\tau_u
\end{aligned} \tag{2.50}
$$

Where the second equality comes from the assumption of $u > 0$ and $u - u_c > 0$. Hence, we have:

$$
\boldsymbol{\theta} = [\alpha_1, \alpha_2, -2\alpha_2 u_c, -\alpha_1 u_c - \alpha_2|u_c|u_c]^\top = [\theta_1, \theta_2, \theta_3, \theta_4]^\top \tag{2.51a}
$$

$$
\boldsymbol{\varphi} = [\varphi_1, \varphi_2, \varphi_3, \varphi_4]^\top = [u, |u|u, |u|, 1]^\top \tag{2.51b}
$$

Where all parameters in $\boldsymbol{\theta}$ are assumed to be constant and is subject to estimation. For a desired surge speed u_d, we can define the error as $e_u = u - u_d$, which gives the error dynamics:

$$
\dot{e}_u = \boldsymbol{\varphi}^\top\boldsymbol{\theta} + \sigma_1(\boldsymbol{v}) + \frac{1}{m_{11}}\tau_u - \dot{u}_d \tag{2.52}
$$

Then we define the Lyapunov function and its derivative:

$$
V_1 = \frac{1}{2} m_{11} e_u^2 \tag{2.53}
$$

$$
\dot{V}_1 = m_{11} e_u \dot{e}_u = e_u\left(\boldsymbol{\varphi}^\top\boldsymbol{\theta} + \sigma_1(\boldsymbol{v}) + \frac{1}{m_{11}}\tau_u - \dot{u}_d\right) \tag{2.54}
$$

with the control

$$
\tau_u = m_{11}\left(-\boldsymbol{\varphi}^\top\hat{\boldsymbol{\theta}} - \sigma_1(\boldsymbol{v}) - K_{pu} e_u + \dot{u}_d\right), \qquad K_{pu} > 0 \tag{2.55}
$$

with $\hat{\boldsymbol{\theta}}$ inserted as the estimate of $\boldsymbol{\theta}$. The estimation error is denoted $\tilde{\boldsymbol{\theta}} = \boldsymbol{\theta} - \hat{\boldsymbol{\theta}}$. Then, (2.54) reduces to:

$$
\dot{V}_1 = -K_{pu} e_u^2 + \boldsymbol{\varphi}^\top\tilde{\boldsymbol{\theta}} e_u \tag{2.56}
$$

Defining Lyapunov function V_2:

$$V_2 = V_1 + \frac{1}{2}\tilde{\boldsymbol{\theta}}^\top \boldsymbol{\Gamma}_u^{-1}\tilde{\boldsymbol{\theta}}, \qquad \boldsymbol{\Gamma}_u = \boldsymbol{\Gamma}_u^\top = \mathrm{diag}(\gamma_{u,1}, \gamma_{u,2}, \gamma_{u,3}, \gamma_{u,4}) > 0, \qquad \dot{\tilde{\boldsymbol{\theta}}} = \dot{\boldsymbol{\theta}} - \dot{\hat{\boldsymbol{\theta}}} = -\dot{\hat{\boldsymbol{\theta}}} \tag{2.57}$$

gives

$$\begin{aligned}
\dot{V}_2 &= \dot{V}_1 + \tilde{\boldsymbol{\theta}}^\top \boldsymbol{\Gamma}_u^{-1}\dot{\tilde{\boldsymbol{\theta}}} \\
&= -K_{pu}e_u^2 + \boldsymbol{\varphi}^\top \tilde{\boldsymbol{\theta}} e_u + \tilde{\boldsymbol{\theta}}^\top \boldsymbol{\Gamma}_u^{-1}\dot{\tilde{\boldsymbol{\theta}}} \\
&= -K_{pu}e_u^2 + \boldsymbol{\varphi}^\top \tilde{\boldsymbol{\theta}} e_u - \tilde{\boldsymbol{\theta}}^\top \boldsymbol{\Gamma}_u^{-1}\dot{\hat{\boldsymbol{\theta}}} \\
&= -K_{pu}e_u^2 + \tilde{\boldsymbol{\theta}}^\top \left(\boldsymbol{\varphi} e_u - \boldsymbol{\Gamma}_u^{-1}\dot{\hat{\boldsymbol{\theta}}}\right)
\end{aligned} \tag{2.58}$$

Then, by defining the estimator dynamics:

$$\dot{\hat{\boldsymbol{\theta}}} = \boldsymbol{\Gamma}_u \boldsymbol{\varphi} e_u \tag{2.59}$$

reduces (2.58) to:

$$\dot{V}_2 = -K_{pu}e_u^2 + \boldsymbol{\theta}^\top \left(\boldsymbol{\varphi} e_u - \boldsymbol{\Gamma}_u^{-1}\boldsymbol{\Gamma}_u \boldsymbol{\varphi} e_u\right) = -K_{pu}e_u^2 < 0 \tag{2.60}$$

Hence, $\dot{V}_2$ is negative semi-definite, and we achieve uniform global stability and convergence of e_u. This controller will be applied in Section 6.

2.3.4 Path Following and Course Control

For a vessel maneuvering at sea, the heading is not the same as the course. The angular difference between course and heading is called *sideslip*, as defined in (2.39a). Therefore, as the control objective often is to control the course to a specific direction, the control system must compensate for this when controlling the heading. Breivik and Fossen (2004) and Fossen et al. (2003) presents a technique for path following for straight lines and circles for underactuated marine surface vessels by sideslip compensation, while recent studies such as Fossen et al. (2015) expands the theory for a curved path with adaptive sideslip compensation with *Line-of-Sight*. The basic principle is as shown below.

Straight-Line Paths
The 2-D position of a surface vessel is defined as $\mathbf{p}^n = [N, E]^\top \in \mathbb{R}^2$. A straight line path is, as the word implies, the straight line between the two points $\mathbf{p}_0^n$ and $\mathbf{p}_1^n$. Where $\mathbf{p}_0^n$ is either the previous waypoint or the current position, and $\mathbf{p}_1^n$ is the next waypoint. The path tangential angle is denoted α_k:

$$\mathbf{p}_0^n = [x_0, y_0]^\top, \qquad \mathbf{p}_1^n = [x_1, y_1]^\top, \qquad \alpha_k = \mathrm{atan2}(y_1 - y_0, x_1 - x_0) \tag{2.61}$$

Line-of-Sight Guidance
Line-of-sight (LOS) is classified as a three-point guidance scheme since it involves a stationary reference point, as well as an interceptor, which is typically the vessel we want to control, and a target that can be either a moving or stationary point. This technique is often used when the vessel

objective is to reach a set of waypoints $\mathbf{p}_k^n$. The cross-track error can be found by rotating the NED-frame coordinates between the vessel position and the previous waypoint by an angle equal to the angle of the active path segment. Hence expressing the distance from the previous waypoint in a path-parallel and a path-normal component. This can be mathematically expressed as in (2.62).

$$\boldsymbol{\epsilon} = \begin{bmatrix} s(t) \\ e(t) \end{bmatrix} = \mathbf{R}^\top(\alpha_k)(\mathbf{p}^n(t) - \mathbf{p}_k^n), \qquad \lim_{t\to\infty} e(t) = 0 \tag{2.62}$$

Here, $s(t)$ denotes the along-track distance from the previous waypoint, and $e(t)$ denotes the cross track error, i.e., the distance from the active path segment as measured normal to it. $\mathbf{p}^n(t)$ denotes the position of the vessel in the NED frame, and $\mathbf{p}_k^n(t)$ denotes the position of the first waypoint in the currently active line segment in the NED frame. The LOS algorithm is used to control the heading of the ship to ensure convergence to a straight-line path, expressed mathematically in (2.62).

The guidance system should construct desired heading ψ_d and surge speed u_d as input to the controllers. Fossen (2011) describes two ways of constructing the desired course angle for path-following on straight line paths between waypoints; *Enclosure-Based Steering* (EBS) and *Lookahead-Based Steering* (LBS). Figure 2.3 shows the EBS setup:

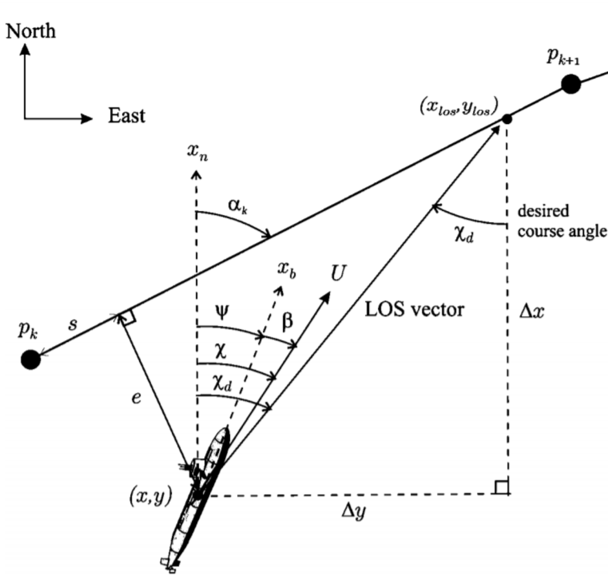

$$\chi_d(t) = \operatorname{atan2}(y_{los} - y(t), x_{los} - x(t)) \tag{2.63a}$$

$$[x_{los} - x(t)]^2 + [y_{los} - y(t)]^2 = R_{EBS}^2 \tag{2.63b}$$

$$\tan(\alpha_k) = \frac{y_{k+1} - y_k}{x_{k+1} - x_k} = \frac{y_{los} - y_k}{x_{los} - x_k} = \text{const} \tag{2.63c}$$

Figure 2.3: Enclosure-based steering setup. Courtesy: Fossen (2011)

EBS relies on enclosing $\mathbf{p}^n$ with a circle with radius R_{EBS} sufficiently large such that the circle will intersect the straight line at two points. By directing the velocity vector towards $\mathbf{p}_{los}^n = [x_{los}, y_{los}]^\top$, we can ensure $e(t) \to 0$ by computing the desired course as in (2.63a), where (x_{los}, y_{los}) is the solution of (2.63b) and (2.63c). See Fossen (2011) for the algebraic solution of (x_{los}, y_{los}).

The other method, LBS, relies on constructing the desired course angle as the sum of the *path-tangential angle* $\chi_p = \alpha_k$ and a *velocity-path relative angle* $\chi_r(e)$. The setup is shown in Figure 2.4.

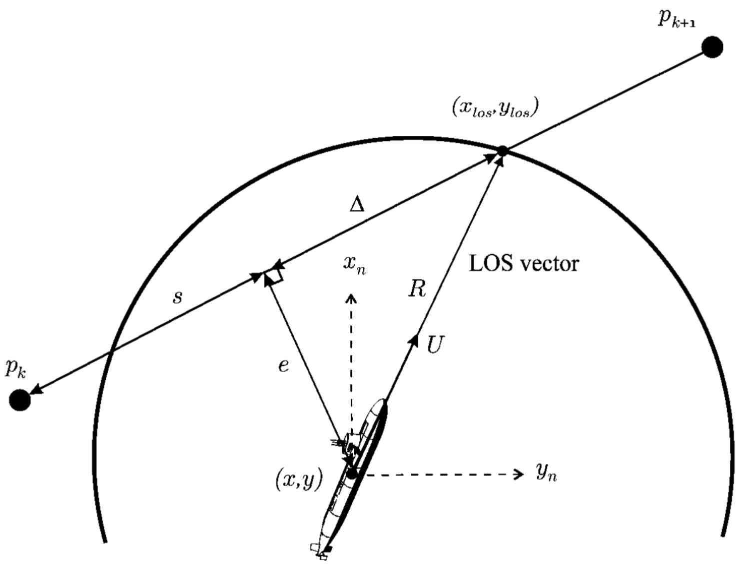

Figure 2.4: Lookahead-based steering setup. Courtesy: Fossen (2011)

$$\chi_d(e) = \chi_p + \chi_r(e) \tag{2.64a}$$
$$\chi_p = \alpha_k \tag{2.64b}$$
$$\chi_r(e) = \arctan\left(\frac{-e(t)}{\Delta_{LBS}(t)}\right) \tag{2.64c}$$
$$\Delta_{LBS}(t) = \sqrt{R_{LBS}^2 - e(t)^2} \tag{2.64d}$$
$$R_{LBS} \geq |e(t)| \tag{2.64e}$$

Here, $\Delta_{LBS}(t)$ denotes a lookahead distance, defined as a desired-path-parallel distance between the projection point of the vessel on to the path and the point toward which one wishes to steer the vessel. Hence, a short lookahead distance yields an aggressive course controller, while a long lookahead distance yields the opposite. It could either be a time varying parameters as in (2.64d), or chosen to be constant, usually between 1.5 – 2.5 of the ships length L_{pp}. Note that in the case of $R_{LBS} < |e(t)|$, other techniques to construct the desired course must be done, such as directing χ_d to be the path-normal projection from its current position, or directly to one of the active waypoints.

Sideslip Compensation
As the course and heading of a ship are not necessarily aligned during turning or due to ocean currents, a sideslip compensation should be done according to (2.65), with β being calculated according to (2.39b). Also, if the control objective is to obtain a speed U_d, the desired surge speed should account for sway velocity according to (2.66).

$$\psi_d = \chi_d - \beta \tag{2.65}$$
$$u_d = \sqrt{U_d^2 - v^2} \tag{2.66}$$

2.3.5 Target Tracking

If there is no trajectory to track, but rather a moving target, the *Target tracking* scheme presented in Breivik (2010) can be used. The goal is to make the controlled vessel, (the *Interceptor*) track another vessel (the *Target*).

A constant bearing guidance scheme is a commonly used scheme for marine applications. Here, the desired velocity $\mathbf{v}_d^n$ is a combination of the bearing velocity and the target velocity. The velocities are rotated in a LOS reference system, relating the lateral distance and cross track error as in (2.62). For the interceptor to keep a relative position behind the target, an additional term,

$\boldsymbol{\epsilon}_d = [s_d, e_d]^\top \in \mathbb{R}^2$ is added to $\boldsymbol{\epsilon}$ in (2.62) to ensure this, showed in (2.67e). The method is based on the equations in (2.67), related to Figure 2.5.

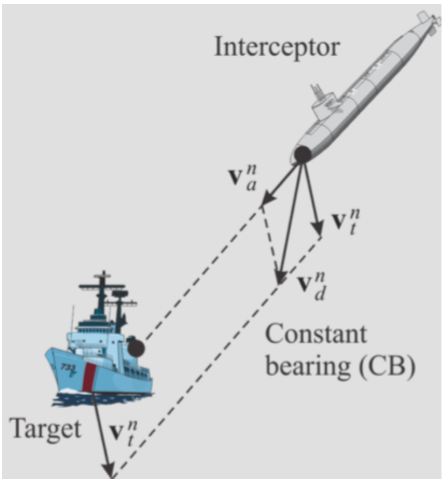

LOS vector between interceptor and target:
$$\tilde{\mathbf{p}}^n := \mathbf{p}^n - \mathbf{p}_t^n \tag{2.67a}$$

Stabilizing term:
$$\kappa = \frac{U_{a,max}||\tilde{\mathbf{p}}^n||}{\sqrt{(\tilde{\mathbf{p}}^n)^\top \tilde{\mathbf{p}}^n + \Delta_{\tilde{p}}^2}} \tag{2.67b}$$

Approach velocity vector:
$$\mathbf{v}_a^n = -\kappa \frac{\tilde{\mathbf{p}}^n}{||\tilde{\mathbf{p}}^n||} \tag{2.67c}$$

Desired velocity/course:
$$\mathbf{v}_d^n = \mathbf{v}_t^n + \mathbf{v}_a^n \tag{2.67d}$$

Cross and alongtrack error:
$$\boldsymbol{\epsilon} = \mathbf{R}^\top(\chi_t)(\mathbf{p}^n(t) - \mathbf{p}_k^n) + \boldsymbol{\epsilon}_d \tag{2.67e}$$

Desired approach speed:
$$U_a = \sqrt{u_a^2 + v_a^2} \tag{2.67f}$$

Desired speed:
$$U_d = ||\mathbf{v}_d^n|| \tag{2.67g}$$

Figure 2.5: Interceptor and target. Courtesy: Fossen (2011)

where $\Delta_{\tilde{p}} > 0$ affects the transient interceptor-target rendezvous behaviour, meaning the larger $\Delta_{\tilde{p}}$, the less aggressive the velocity component pointing directly at the target will be. χ_t denotes the course of the target and $U_{a,max}$ denotes the maximum approach speed toward the target. The desired velocity vector (2.67d) defines both the desired speed and course.

2.3.6 Reference models

In tracking operations, where the ship moves from one position and heading to another, a reference model is needed for achieving a smooth transition. A feasible trajectory means one that is consistent with the vessel dynamics in each degree of freedom. In linear system theory this means that the reference model must have slower eigenvalues compared to the craft dynamics. In a non-linear case like the one presented, this translates to bandwidth of the reference model being lower than the bandwidth of the motion control system in order to obtain satisfactory tracking performance and stability. Fossen (2011) presents a velocity reference model modelled as a *mass-spring-damper* system:

$$\ddot{\boldsymbol{\nu}}_d + 2\boldsymbol{\Delta\Omega}\dot{\boldsymbol{\nu}}_d + \boldsymbol{\Omega}^2\boldsymbol{\nu}_d = \boldsymbol{\Omega}^2\mathbf{r}^b \tag{2.68}$$

where $\boldsymbol{\nu}_d \in \mathbb{R}^n$ is the desired velocity, $\dot{\boldsymbol{\nu}}_d \in \mathbb{R}^n$ the desired acceleration and $\ddot{\boldsymbol{\nu}}_d \in \mathbb{R}^n$ the desired jerk. $\boldsymbol{\Delta} = diag\{\zeta_1, \zeta_2, ..., \zeta_n\} > 0 \in \mathbb{R}^{nxn}$ and $\boldsymbol{\Omega} = diag\{\omega_{n_1}, \omega_{n_2}, ..., \omega_{n_n}\} > 0 \in \mathbb{R}^{nxn}$ denote the relative damping ratios and natural frequencies, respectively. $\mathbf{r}^b \in \mathbb{R}^n$ is the desired velocity.

For a two dimensional velocity reference model in surge and turning rate for a marine vessel, this reduces to:

$$\ddot{u}_d + 2\zeta_u \omega_{n_u} \dot{u}_d + \omega_{n_u}^2 u_d = \omega_{n_u}^2 u_{ref} \tag{2.69a}$$

$$\ddot{r}_d + 2\zeta_r \omega_{n_r} \dot{r}_d + \omega_{n_r}^2 r_d = \omega_{n_r}^2 r_{ref} \tag{2.69b}$$

which results in the transfer functions:

$$\frac{u_d}{u_{ref}}(s) = \frac{\omega_{n_u}^2}{s^2 + 2\zeta_u \omega_{n_u} s + \omega_{n_u}^2} \tag{2.70a}$$

$$\frac{r_d}{r_{ref}}(s) = \frac{\omega_{n_r}^2}{s^2 + 2\zeta_r \omega_{n_r} s + \omega_{n_r}^2} \tag{2.70b}$$

where u_d and r_d is the surge speed and turning rate that is used in the controller. The relative damping ratios ζ_u and ζ_r are often set to one to get a critically damped reference. The natural frequencies ω_{n_u} and ω_{n_r} should be set such that it generate a feasible velocity trajectory for the dynamic system it is applied on.

2.4 Autonomous Marine Control Systems

Extensive research and progress has been made when it comes to autonomous systems the last decades. Lekkas (2018) distinguishes between *automatic* and *autonomous* systems, where an automatic system is a system that does exactly what it is programmed to do, without choice or possibility to act in any different way. Furthermore, a deliberating system is a system that performs actions motivated by some intended objectives, justifiable by sound reasoning with respect to these objectives. An autonomous system is a combination of these two, i.e a system that possesses self-governing characteristics which, ideally, allow it to perform pre-specified tasks/missions without human intervention. To characterize the different types of autonomy, Ludvigsen and Sørensen (2016) present the following four levels of autonomy:

1. ***Automatic operation** (**remote control**) means that even though the system operates automatically, the human operator directs and controls all high-level mission-planning functions, often preprogrammed (**human-in-the-loop/human operated**).*

2. ***Management by consent** (**teleoperation**) means that the system automatically makes recommendations for mission actions related to specific functions, and the system prompts the human operator at important points in time for information or decisions. At this level, the system may have limited communication bandwidth including time delay, due to i.e. distance. The system can perform many functions independently of human control when delegated to do so (**human-delegated**).*

3. ***Semi-autonomous or management by exception** means that the system automatically executes mission-related functions when response times are too short for human intervention. The human may override or change parameters and cancel or redirect actions within defined time lines. The operator attention is only brought to exceptions for certain decisions (**human-supervisory control**).*

4. ***Highly autonomous**, which means that the system automatically executes mission-related functions in an unstructured environment with ability to plan and re-plan the mission. The*

*human may be informed about the progress. The system is independent and "intelligent" (**human-out-of-the loop**)*

For more details, see NIST (2018) and National Research Council (2005).

The complexity of an autonomous system depends on a number of factors such as the human Independence(HI), the mission complexity(MC) and the environment complexity(EC). Figure 2.6 shows the terminology of an autonomous system, while Figure 2.7 characterizes the conceptual autonomous capability according to these factors.

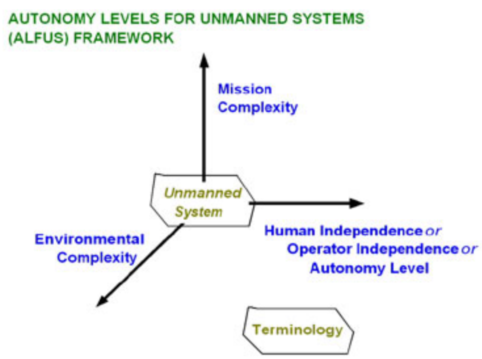

Figure 2.6: Autonomy levels framework. Courtesy: NIST (2018)

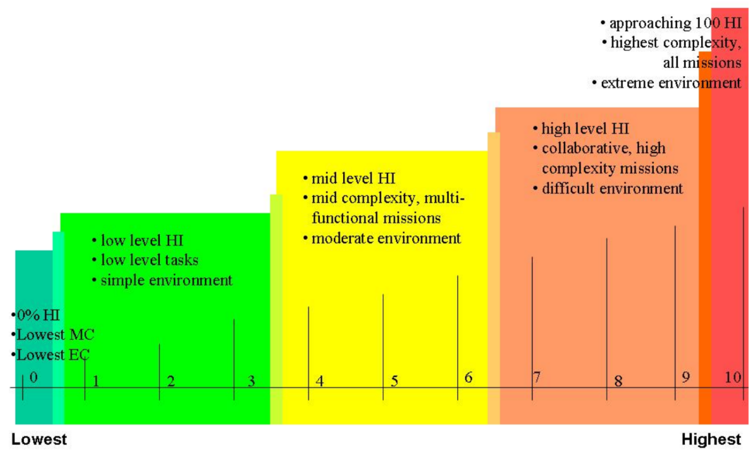

Figure 2.7: Contextual autonomous capability. Courtesy: NIST (2018)

An autonomous system where a human operator is in the loop puts high demands on the human-machine system to be capable of surviving weaknesses in both machine and human functioning. Hence, the robustness and resilience of an autonomous system should be assessed. The resilience of a system represents its ability to return to normal operation in the case of damages or failures, while robustness is the systems ability to function effectively in a range of demanding circumstances. Both these factors plays a key role for the overall performance of a system to be acceptable. Recent studies in Matthews Gerald (2016) addresses the challenges posed by interaction with autonomous systems. This study points out the importance of not only engineering an autonomous system against failures but also such that it can communicate its level of functioning to the human and to adapt to operator status.

Chapter 3

Hybrid Dynamical Systems and Control

A hybrid system is a dynamical system which exist both in discrete time and continuous time. It can either *flow* in continuous time or *jump* in discrete time. A hybrid state is defined as the values in the continuous state and the discrete mode it is in. This section will go through the mathematical preliminaries and conventions for such systems, and exemplify some of the theory as it is presented.

3.1 Preliminaries

In GS, LAS, LES, UGAS, UGES, etc., stands G for Global, L for Local, S for Stable, U for Uniform, A for Asymptotic, and E for Exponential. A diagonal matrix is denoted $\mathrm{diag}\{a_1, \dots, a_n\} \in \mathbb{R}^{n\times n}$. Stacking several vectors into one is denoted $x = \mathrm{col}(x_1, x_2, x_3) := [x_1^\top, x_2^\top, x_3^\top]^\top$, similarly $x^\top = \mathrm{row}(x_1, x_2, x_3)$ is a row vector, and whenever convenient, $|(x_1, x_2, x_3)| = |x|$. The Euclidean vector norm is $|x| := (x^\top x)^{1/2}$. Total time derivatives of $x(t)$ are denoted $\dot{x}$, $\ddot{x}$, $x^{(3)}, \dots, x^{(n)}$. For a function $\alpha : \mathbb{R}^n \to \mathbb{R}$ the gradient is the row vector $\nabla\alpha(x) := \frac{\partial\alpha}{\partial x}$ and for $\alpha : \mathbb{R}^n \to \mathbb{R}^m$ the Jacobian is the matrix $J_\alpha(x) := \mathrm{col}\left(\frac{\partial\alpha_1}{\partial x}, \frac{\partial\alpha_2}{\partial x}, \cdots, \frac{\partial\alpha_m}{\partial x}\right)$.

3.2 General Hybrid Systems Preliminaries

As many dynamical systems combine behaviours typical for both continuous-time dynamical systems and discrete-time events, this section is to generalize the concept of switching between these two events. Rafal Goebel and Teel (2012) presents a general model on the form shown in (3.1).

$$\dot{\mathbf{x}} \in F(\mathbf{x}), \qquad \mathbf{x} \in C \tag{3.1a}$$
$$\mathbf{x}^+ \in G(\mathbf{x}), \qquad \mathbf{x} \in \mathcal{D} \tag{3.1b}$$

The continuous model is described by (3.1a), where $\mathbf{x}$ represents the state in the n-dimensional euclidean space $\mathbb{R}^n$, $F(\mathbf{x})$ the first order differential inclusion and C is a subset of $\mathbb{R}^n$. In the discrete model (3.1b), $\mathbf{x}^+$ denotes the next value of the state through the set-valued mapping $G(\mathbf{x})$ and $\mathcal{D}$ is a subset of $\mathbb{R}^n$. C is called the *flow set*, F the *flow map*, $\mathcal{D}$ the *jump set* and G the *jump map*. The hybrid form of the entire system (3.1) is denoted $\mathcal{H}$.

$$\mathcal{H} = (C, F, \mathcal{D}, G) \tag{3.2}$$

The hybrid time domain is a set $E \subset \mathbb{R}_{\geq 0} \times \mathbb{Z}_{\geq 0}$ such that for each $(T, J) \in E$ the set $E \cap ([0, T] \times \{0, 1, 2, ..., J\})$ is a compact hybrid time domain.

$$E = \bigcup_{j=0}^{J} ([t_i, t_{i+1}] \cup \{i\}) \tag{3.3}$$

for some $J \in \mathbb{Z}_{\geq 0}$ and real numbers $0 = t_0 \leq t_1 \leq t_2 \leq ... \leq t_{J+1}$. Functions in hybrid time domains is called *hybrid arc*, which is a function $x : \text{dom}\, x \to \mathbb{R}^n$ with *dom* x being a hybrid time domain and for each $j \in \mathbb{N}$, $t \mapsto x(t, j)$ is locally absolutely continuous. The solution to a hybrid system $\mathcal{H}$ is a hybrid arc which contains the origin $x(0, 0) \in C \cup \mathcal{D}$ and $\forall j \in \mathbb{N}$ such that $I_j := \{t : (t, j) \in \text{dom}\, x\}$ has nonempty interior

$$\mathbf{x}(t, j) \in C \qquad \text{for all } t \in [\min I_j, \sup I_j) \tag{3.4}$$

$$\dot{\mathbf{x}}(t, j) = \mathbf{F}(\mathbf{x}(t, j)) \qquad \text{for almost all } t \in I_j \tag{3.5}$$

and $\forall (t, j) \in \text{dom}\, x$ such that $(t, j + 1) \in \text{dom}\, x$ and:

$$\mathbf{x}(t, j) \in \mathcal{D}, \mathbf{x}(t, j + 1) \in \mathbf{G}(\mathbf{x}(t, j)) \tag{3.6}$$

Figure 3.1 illustrates different kind of hybrid time domains and arcs.

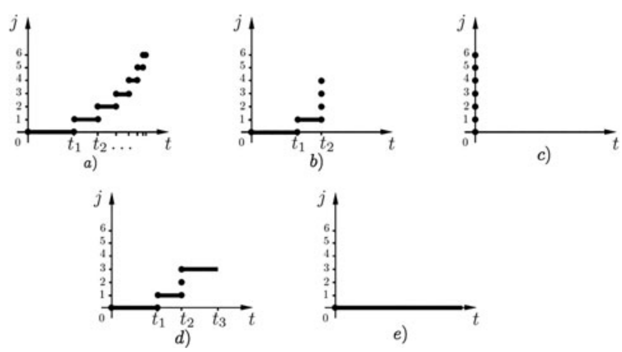

(a) Hybrid time domains associated with different types of solutions of a hybrid system: a) Zeno, b) eventually discrete, c) purely discrete, d) eventually continuous, and e) purely continuous

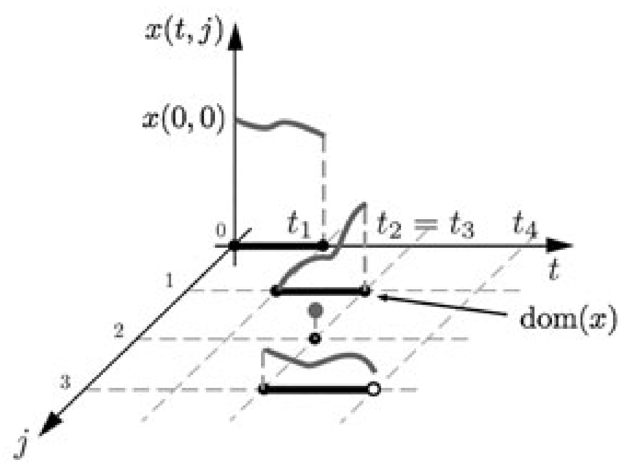

(b) A hybrid arc associated with a hybrid dynamical system

Figure 3.1: Examples of hybrid time domains and a hybrid arc generated by a hybrid dynamical system Courtesy: Rafal Goebel and Teel (2012)

Here, (t, j) are pairs of time t and the number of jumps j. A solution is *nontrivial* if it contains at least one point different from $(0, 0)$. There is no requirement that C and $\mathcal{D}$ does not overlap, so when $C \cap \mathcal{D} \neq \emptyset$, the solution may either jump or flow depending on the jump and flow map.

For a hybrid system to be asymptotically stable, there must exist a compact set $\mathcal{A} \subset \mathbb{R}^n$ which is both *stable* and *attractive* for $\mathcal{H}$, is bounded, and the complete solutions converge to the *basin of attraction* of $\mathcal{A}$. If the basin of attraction cover the entire Euclidean space $\mathbb{R}^n$, the solution is said to be globally asymptotically stable.

An example of a physical system that can be described as a hybrid system is a bouncing ball, where the position and velocity while in air follows dynamical equations in continuous time, while the bouncing event switches sign of the velocity and decreases in absolute value due to energy losses in the bounce. Generalizing the continuous and discrete time-domains as a hybrid system, enables a structured way of handling switching systems while at the same time providing a framework for analyzing robustness and stability.

3.3 Hybrid Control on $\mathbb{S}^1$

Controlling the orientation is a nontrivial task that is subject to topological disruptions, i.e splitting angles evolving on a compact manifold into a defined range (as disrupting $\mathbb{S}^1$ to $[-\pi, \pi]$). With such disruption, a system can not have a globally stabilizing continuous feedback law that has a single globally asymptotically stable equilibrium point. In addition, arbitrary small measurement noise can destroy asymptotic stability.

In order to design a control law that achieves robust global stability of the desired rotation, there must be a class of control laws that can be coordinated such that it removes the need of manually placing a hysteresis or define domains of operation of each controller. This section will present a hybrid control structure for a kinetic point stabilization problem on $\mathbb{S}^1$.

3.3.1 Teel's Notation for $\mathbb{S}^1$ Manipulations

For the topic of this thesis, the aim is to conduct a hybrid system that controls the heading of a ship towards a desired heading. Instead of wrapping the heading and heading errors on to an interval, the idea is to represent angles as points on the unit circle and control these points towards the desired point. In Teel (2018) and Mayhew and Teel (2010), we define the unit circle $\mathbb{S}^1$ and group of planar rotations $SO(2)$ as:

$$\mathbb{S}^1 := \left\{ z \in \mathbb{R}^2 : z^\top z = 1 \right\} \tag{3.7}$$

$$SO(2) := \left\{ R \in \mathbb{R}^{2\times 2} : R^\top R = RR^\top = I, \ \det(R) = 1 \right\} \tag{3.8}$$

where $(\cdot)^\top$ is the transpose and I is the identity matrix. Let $z := \mathrm{col}(z_x, z_y) \in \mathbb{S}^1$, $\mathbf{e}_1 := \mathrm{col}(1, 0) \in \mathbb{S}^1$ and $\mathbf{e}_2 := \mathrm{col}(0, 1) \in \mathbb{S}^1$, and define the matrices

$$S := [\mathbf{e}_2, -\mathbf{e}_1], \qquad J = [\mathbf{e}_1, -\mathbf{e}_2] \tag{3.9}$$

Hence, for a counter-clockwise rotation a on $\mathbb{S}^1$ from the x-axis, the following holds:

$$\left\{\begin{array}{l} z_x^a = \cos a \\ z_y^a = \sin a \end{array}\right\} \Leftrightarrow \left\{\begin{array}{l} a = \operatorname{atan2}\left(z_y^a, z_x^a\right) \\ 1 = (z_x^a)^2 + (z_y^a)^2 \end{array}\right\}, \tag{3.10}$$

$$z^{-a} := Jz^a = \operatorname{col}(z_x^a, -z_y^a) \in \mathbb{S}^1, \qquad R(z) := \left[\begin{array}{cc} z & Sz \end{array}\right], \qquad z = R(z)\mathbf{e}_1 \tag{3.11}$$

$$z^a = \operatorname{col}(z_x^a, z_y^a) \in \mathbb{S}^1, \qquad R(z^a)^\top = \left[\begin{array}{cc} z_x^a & z_y^a \\ -z_y^a & z_x^a \end{array}\right] = R(z^{-a}), \qquad R(z^{-a})R(z^a) = R(z^a)R(z^{-a}) = I \tag{3.12}$$

Note that the way of representing the angle directly on $\mathbb{S}^1$ makes any "*rad2pipi*" mapping of an angle from the $(-\infty, \infty)$ to the $[-\pi, \pi)$ interval in (3.10) unnecessary, and it will not introduce any other discontinuities that may cause robustness or stability issues for a feedback control system. Another advantage of representing an angle on $\mathbb{S}^1$ is that it introduces a convenient way of adding and subtracting angles by multiplication, as well as other rotational relationships:

$$z^a \circ z^b = z^{a+b} = R(z^b)z^a = R(z^a)z^b, \; z^{a-b} = R(z^b)^\top z^a = R(z^{-b})z^a, \; R(z^a)R(z^b) = R(z^b)R(z^a) \in SO(2), \tag{3.13}$$

$$R(z^b)^\top R(z^a)^\top = R(z^a)^\top R(z^b)^\top \in SO(2), \; R(z^a)^\top R(z^b) = R(z^b)R(z^a)^\top \in SO(2) \tag{3.14}$$

Also, the kinematic equation for an angle z^a constrained to move along the unit circle is given as:

$$\dot{z}^a = \omega_a S z^a, \qquad \frac{d}{dt}\left(R(z^a)\right) = \omega_a S R(z^a) \tag{3.15}$$

with $\omega_a \in \mathbb{R}$ being the rotation rate in [rad / s].

In the case of a vector defined as $v = [v_x, v_y] \in \mathbb{R}^2$, where $U = |v| = \sqrt{v^\top v}$ and $a = \operatorname{atan2}(v_y, v_x)$, we can express the angle on $\mathbb{S}^1$ as:

$$z^a = \frac{v}{U} = [v_x/U, v_y/U]^\top \tag{3.16}$$

Then, the velocity vector expressed with an $\mathbb{S}^1$ formulation is then $v = Uz^a$. Manipulating (3.15), we can also express the angular rate as:

$$\omega_a = (z^a)^\top S^\top \dot{z}^a = \frac{v^\top}{U} S^\top \left(\frac{v^\top v I - v v^\top}{U^3}\right)\dot{v} = \frac{v^\top}{U} S^\top \frac{U^2 I}{U^3}\dot{v} = (z^a)^\top S^\top \frac{\dot{v}}{U} \tag{3.17}$$

3.3.2 Example - Robustly Globally Asymptotically Stabilizing a Point on the Circle

To draw parallels to the problem of this thesis, a robust hybrid heading controller of a ship can in a simple way be interpreted as a way to robustly globally asymptotically stabilize a point in the unit circle. We cannot pick a discontinuous function and expect the system to be robust, but we can choose a hybrid feedback and get robustness. The key is to make sure that the point (or course of a ship) points in the desired direction no matter where it starts and the magnitude of the measurement noise. As an example, if a ship is commanded to do a 180 degree turn, you can draw a line from the heading which the ship is pointing and the way it is going. Small perturbations in measurements can confuse the controller on which side of this line it is. This can lead to a chattering behaviour in the control input, and in the worst case it will not reach its reference at all. The hybrid system for point stabilizing control on $\mathbb{S}^1$ can be expressed as in (3.1).

$$\dot{\mathbf{x}} = \begin{bmatrix} \dot{z}_1 \\ \dot{z}_2 \\ \dot{q} \end{bmatrix} = \begin{bmatrix} z_2\omega \\ -z_1\omega \\ 0 \end{bmatrix}, \qquad C = (C_1 \times \{q = 1\}) \cup (C_2 \times \{q = 2\}) \tag{3.18a}$$

$$\mathbf{x}^+ = \begin{bmatrix} z_1^+ \\ z_2^+ \\ q^+ \end{bmatrix} = \begin{bmatrix} z_1 \\ z_2 \\ 3-q \end{bmatrix}, \qquad \mathcal{D} = (\mathcal{D}_1 \times \{q = 1\}) \cup (\mathcal{D}_2 \times \{q = 2\}) \tag{3.18b}$$

Here, the state vector $\mathbf{x} = [z_1, z_2, q]^\top$ with $\mathbf{z} = [z_1, z_2]^\top \in \mathbb{S}^1$ being the vector constrained to the unit circle, and $\omega \in \mathbb{R}$ is the control input controlling the point towards $\mathbf{e}_1$. A logic mode $q \in \{1, 2\}$ can be used to toggle between the flow sets C_1 and C_2.

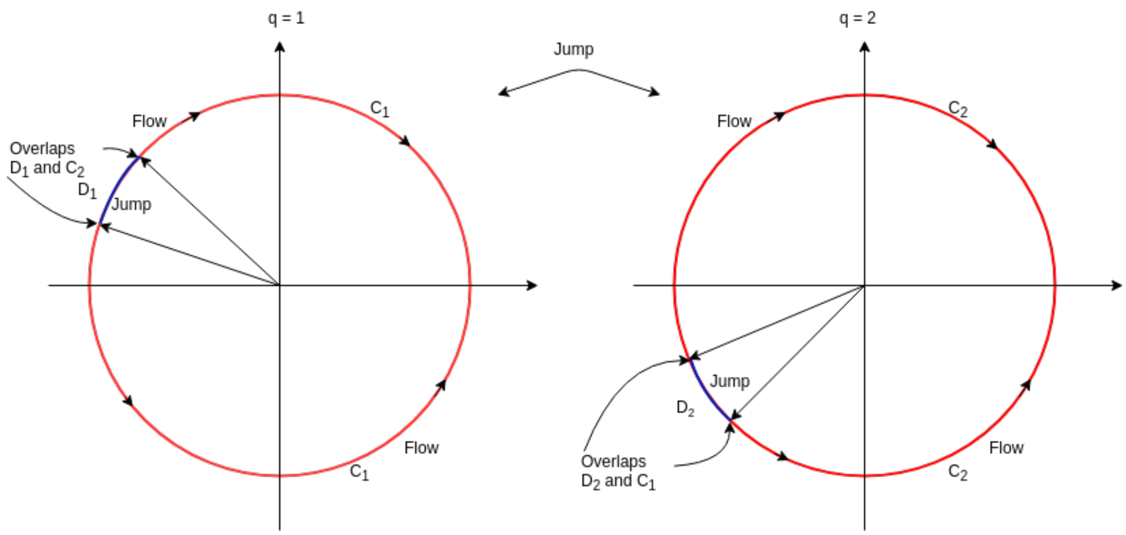

Figure 3.2: Flow and jump sets for stabilizing a point on $\mathbb{S}^1$.

Figure 3.2 illustrates this, where the flow sets C_1 and C_2(in red) are designed to overlap to ensure a closed set C. This means that at these points where they overlap, it will either jump or flow depending on the value of q. In the case of $\mathbf{x} \in \mathcal{D}$(in blue), it will jump and the logic mode q will toggle. Then, assuming the magnitude of the measurement noise is not large enough, it is not close to jumping again and it will flow towards the point. What this does is creating a hysteresis mechanism to make sure it does not revise its decision on which way to go around the circle unless there is a dramatic change in the state. Hence, the controller is hybrid with a logic mode which can not change continuously and guarantees robustness. It is worth mentioning that similar properties can be achieved by having a dwell time in the toggling, where it waits for a small amount of time after toggling before it can toggle again.

The following subsections will describe the necessary conditions and equations for designing the control ω for such system.

3.3.3 Potential Functions and Virtual Controls - Non-hybrid

A technique presented in Mayhew and Teel (2010) shows how to stabilize a point on the unit circle $\mathbb{S}^1$, which is equivalent to stabilizing a group of planar rotations $SO(2)$ using an alternative Lyapunov-based approach that also relies on hysteresis to switch between stabilizing control laws. Lyapunov functions evolving on $\mathbb{S}^1$ will need to have at least one minimum and one maximum on the unit circle. We must therefore have minimum two critical points, whereas one is stable and one is unstable. Therefore, single smooth control laws linked to Lyapunov functions may have critical points where the control law vanishes or is not robust enough. A set of Lyapunov functions with exactly one minimum and one maximum, where the maximum of each Lyapunov function lies within the associated jump set can be defined. Then we can construct stabilizing control laws according to each Lyapunov function, and due to the placement of the unstable equilibrium inside the jump sets, we can achieve robust global stability of the desired rotation.

Let $\mathscr{P}$ be a family of continuous differentiable potential function, with the following properties for every $P \in \mathscr{P}$:

(P1) $P : \mathbb{S}^1 \to [0,1]$ is surjective (meaning for every element $p \in [0,1]$, there is at least one element $z \in \mathbb{S}^1$ such that $P(z) = p$)

(P2) There exist exactly two critical points, $\mathbf{e}_1$ and $\bar{z}_P$ satisfying $P(\mathbf{e}_1) = 0$, $P(\bar{z}_P) = 1$, $\langle \nabla_z P(\mathbf{e}_1), S\,\mathbf{e}_1 \rangle = 0$, $\langle \nabla_z P(\bar{z}_P).S\,\bar{z}_P \rangle = 0$

Where $\langle \nabla_z P(z), Sz \rangle$ denotes the gradient of $P(z) \in \mathscr{P}$ along the manifold $\mathbb{S}^1$, i.e the dot product $\nabla_z P(z)^\top \cdot Sz$, where $\nabla_z = \left[\frac{\partial}{\partial z_x}, \frac{\partial}{\partial z_y}\right]^\top$

Next, define a class of control laws $\mathscr{C}(P)$ corresponding to a potential function $P \in \mathscr{P}$:

(C1) $\langle \nabla_z P(z), Sz \rangle \kappa(z) \leq 0$ for all $z \in \mathbb{S}^1$

(C2) $\langle \nabla_z P(z), Sz \rangle \kappa(z) = 0$ if and only if $\langle \nabla_z P(z), Sz \rangle = 0$

For an objective to drive an angle $z^a \to z^b$, the error between these can be expressed on $\mathbb{S}^1$ as:

$$z = R\left(z^b\right)^\top z^a = z^a \circ z^{-b} \tag{3.19}$$

where $z = \mathbf{e}_1$ is equivalent to $z^a = z^b$. With the kinematics of z^a and z^b expressed as $\dot{z}^a = \omega_a S z^a$ and $\dot{z}^b = \omega_b S z^b$, we have:

$$\dot{z} = (\omega_a - \omega_b) S z = \tilde{\omega} S z \tag{3.20}$$

Where $\tilde{\omega} = \omega_a - \omega_b$.

Hence, for a potential function $P(z) \in \mathscr{P}$ with control law $\kappa(z) \in \mathscr{C}(P)$ that drives $\tilde{\omega} \to 0$, we have:

$$\dot{P}(z) = \nabla_z P(z)^\top \dot{z} = \nabla_z P(z)^\top \tilde{\omega} S z = \nabla_z P(z)^\top \kappa(z) S z = \langle \nabla_z P(z), Sz \rangle \kappa(z) \tag{3.21}$$

Where it is assumed that $\tilde{\omega}$ tracks $\kappa(z)$ perfectly, i.e $\tilde{\omega} = \kappa(z)$.

As shown in Bhat and Bernstein (2000), the states of this system evolves on compact manifolds, and can therefore not have a single GAS equilibrium. Therefore, Mayhew and Teel (2010) presents a hybrid control for $\tilde{\omega}$, by letting $\kappa_{\tilde{\omega}}$ denote the virtual control for $\tilde{\omega}$ that ensures robust global asymptotic stability of the set $\mathcal{A}_0 := \{\mathbf{e}_1\} \times Q$ for the state $\xi := (z, q) \in \mathbb{S}^1 \times Q$, where $Q := \{1, 2\}$ is the allowable values of the logic mode q that switches between the two control laws. Next, define the set $\mathcal{E}_0 := \{(z, q) \in \mathbb{S}^1 \times Q : \langle \nabla_z P(z), Sz \rangle \kappa(z) = 0\}$. To develop a hybrid control law for ξ, one must first find a suitable potential function and control law for all $z \in \mathbb{S}^1 \setminus \{-\mathbf{e}_1\}$, and then use this as a base to design a hybrid control design that guarantees GAS of the set $\mathcal{A}_0$.

A potential function $P_{00}(z) \in \mathscr{P}$ is proposed:

$$P_{00}(z) = \frac{1}{2}(1 - z_x) \tag{3.22}$$

such that $P_{00}(\mathbf{e}_1) = 0$ and $P_{00}(-\mathbf{e}_1) = 1$ and the differential $\nabla_z P_{00}(z) = -\frac{1}{2}\mathbf{e}_1{}^\top$. The gradient along $\mathbb{S}^1$ at $z = \mathbf{e}_1$ and $z = -\mathbf{e}_1$ is then $\nabla_z P_{00}(\mathbf{e}_1)^\top S\,\mathbf{e}_1 = -\frac{1}{2}\mathbf{e}_1{}^\top \mathbf{e}_2 = 0$ and $\nabla_z P_{00}^\top(-\mathbf{e}_1) S(-\mathbf{e}_1) = 0$, respectively. Hence we have two equilibria, one stable and one unstable. To drive $z \to \mathbf{e}_1$ for all $z \in \mathbb{S}^1 \setminus \{-\mathbf{e}_1\}$, we can assume that we can control $\tilde{\omega} \to 0$ by the virtual control $\kappa_{00}(z) \in \mathscr{C}(P_{00})$ in (3.23).

$$\kappa_{00}(z) = -z_y \tag{3.23}$$

Then, we can replace $\tilde{\omega}$ with $\kappa_{00}(z)$ in (3.20). This leads to:

$$\dot{z} = \kappa_{00}(z) S z = -z_y S z = [z_y^2, -z_x z_y]^\top \tag{3.24}$$

And the derivative of $P_{00}(z)$ along $\mathbb{S}^1$ with control $\kappa_{00}(z)$ then becomes:

$$\dot{P}_{00}(z) = \langle \nabla_z P_{00}(z), Sz \rangle \kappa_{00}(z) = \nabla_z P_{00}(z)^\top S z \kappa_{00}(z) = \frac{1}{2}\mathbf{e}_1{}^\top S z z_y = -\frac{1}{2} z_y^2 = -\frac{1}{2}\sin^2\theta \tag{3.25}$$

where the last equality comes from the fact that $z_x = \cos\theta$ and $z_y = \sin\theta$. We observe that for all $z \in \mathbb{S}^1 \setminus \{-\mathbf{e}_1\}$, we have $\dot{P}_{00}(z) < 0$, driving $z \to \mathbf{e}_1$. We can also see that $\dot{z}$ has two equilibrium points, i.e at $z = \pm\mathbf{e}_1(\theta = \{0, \pm\pi\})$, where $z = \mathbf{e}_1$ is stable and $z = -\mathbf{e}_1$ is unstable. Hence, the singularity $z = -\mathbf{e}_1$ must be avoided, which motivates for a hybrid structure with two potential functions where an diffeomorphism is applied on the $\mathbb{S}^1$ manifold to move this unstable equilibrium onto the jump sets of two different control laws. More on this later.

We not only want the point to be stable, but also the convergence rate to be uniformly along the unit circle arc. As $\kappa_{00}(z)$ is very small close to the unstable equilibrium $z = -\mathbf{e}_1$, the rate of convergence is not reflected in the magnitude of the error along the unit circle. Hence, a potential function $P_{01}(z) \in \mathscr{P}$ is proposed:

$$P_{01}(z) = L(\arccos(\lambda \mathbf{e}_1{}^\top z) - \arccos(\lambda)), \qquad L = 1/(\arccos(-\lambda) - \arccos(\lambda)) \tag{3.26}$$

This function is designed to reflect the arc length from z to $\mathbf{e}_1$ along the unit circle, and is scaled by $0 \ll \lambda < 1$ to bound the gradient. Hence, this function satisfies both property (P1) and (P2). Figure 3.3 shows the manifold of $P_{00}(z)$ and $P_{01}(z)$ for angle errors in the range $[-180°, 180°]$:

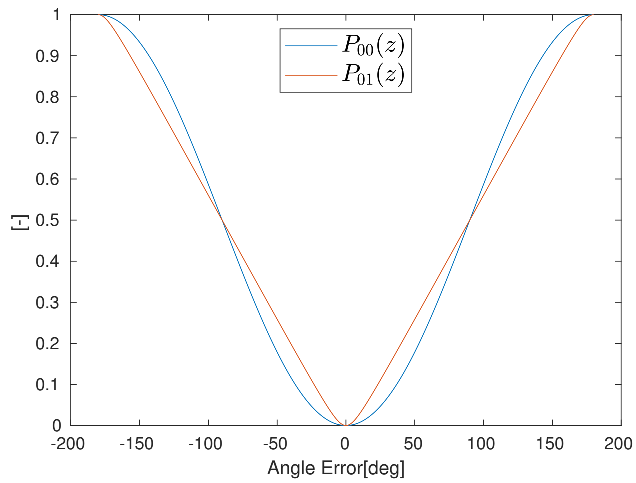

Figure 3.3: Manifold of potential functions P_{00} and P_{01}

Now that we have a potential function that reflects the arc length along the unit circle, we seek to find a control $\kappa \in \mathscr{C}(P_{01})$. One candidate is $\kappa_{01}(z) = -K_p z_y$, $K_p > 0$, or alternatively:

$$\kappa_{02}(z) = -\frac{K_p}{\lambda L}\frac{z_y}{\sqrt{1-\lambda^2 z_x^2}}\sqrt{P_{01}(z)}, \qquad \kappa_{03}(z) = -\frac{K_p}{\lambda L}\frac{z_y}{\sqrt{1-\lambda^2 z_x^2}}P_{01}(z) \tag{3.27}$$

Where κ_{02} and κ_{03} gives linear and exponential convergence, respectively. In these functions, the the term

$$\frac{z_y}{\sqrt{1-\lambda^2 z_x^2}} = \frac{z_y}{\sqrt{1-\lambda^2(1-z_y^2)}} = \frac{z_y}{\sqrt{1-\lambda^2+\lambda^2 z_y^2}} \approx \frac{z_y}{\lambda|z_y|} \approx \operatorname{sign}(z_y) \tag{3.28}$$

with $0 << \lambda < 1$ is a smooth sign-function of z_y that sets the correct sign of the feedback.

Analyzing the potential function P_{01}, the gradient and derivative when combined becomes:

$$\nabla_z P_{01}(z) = \left[\frac{-L\lambda}{\sqrt{1-\lambda^2 z_x^2}}, 0\right]^\top, \qquad \dot{P}_{01}(z) = \nabla_z P_{01}(z)^\top \dot{z} = \frac{-L\lambda}{\sqrt{1-\lambda^2 z_x^2}}\dot{z}_x \tag{3.29}$$

where $\dot{z}_x$ is found by inserting κ_{01}, κ_{02} and κ_{03} for $\tilde{\omega}$ in (3.20). This gives:

$$\dot{z}_{x,\kappa_{01}} = K_p z_y^2, \qquad \dot{z}_{y,\kappa_{01}} = -K_p z_y z_x, \qquad \dot{P}_{01,\kappa_{01}} = K_p\frac{L\lambda z_y^2}{\sqrt{1-\lambda^2 z_x^2}} \tag{3.30a}$$

$$\dot{z}_{x,\kappa_{02}} = \frac{K_p}{\lambda L}\frac{z_y^2\sqrt{P_{01}(z)}}{\sqrt{1-\lambda^2 z_x^2}}, \qquad \dot{z}_{y,\kappa_{02}} = \frac{K_p}{\lambda L}\frac{-z_y z_x\sqrt{P_{01}(z)}}{\sqrt{1-\lambda^2 z_x^2}}, \qquad \dot{P}_{01,\kappa_{02}} = K_p\frac{z_y^2\sqrt{P_{01}(z)}}{1-\lambda^2 z_x^2} \tag{3.30b}$$

$$\dot{z}_{x,\kappa_{03}} = \frac{K_p}{\lambda L}\frac{z_y^2 P_{01}(z)}{\sqrt{1-\lambda^2 z_x^2}}, \qquad \dot{z}_{y,\kappa_{03}} = \frac{K_p}{\lambda L}\frac{-z_y z_x P_{01}(z)}{\sqrt{1-\lambda^2 z_x^2}}, \qquad \dot{P}_{01,\kappa_{03}} = K_p\frac{z_y^2 P_{01}(z)}{1-\lambda^2 z_x^2} \tag{3.30c}$$

where all renders $z = \mathbf{e}_1$ asymptotically stable for (3.20) with region of convergence $\mathbb{S}^1 \setminus \{-\mathbf{e}_1\}$. The manifolds for all virtual controls κ with $K_p = 0.5$ and $\lambda = 0.99$ is shown in Figure 3.4a, and the resulting potential function derivatives is shown in Figure 3.4b.

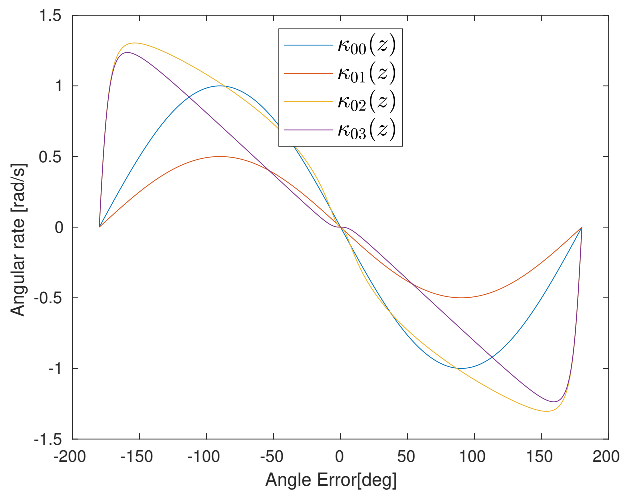

(a) Manifolds for virtual controls

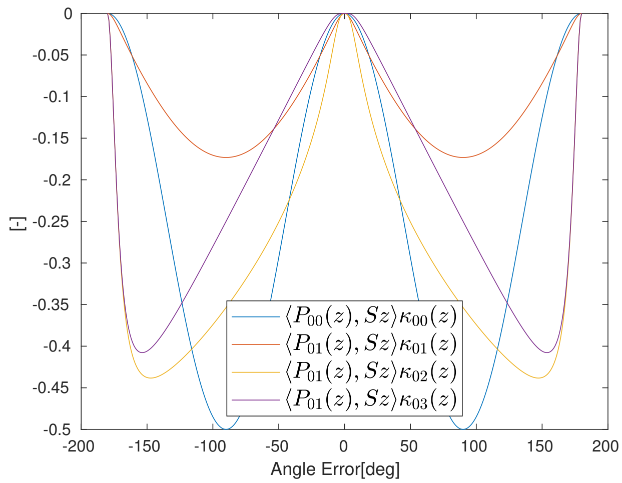

(b) Derivatives of potential functions with different controls

Figure 3.4: Manifolds of virtual controls and their derivatives

The small control signals close to $z = -\mathbf{e}_1$ in κ_{00} and κ_{01} is solved with κ_{02} and κ_{03}. In addition, the derivatives for all controls is negative for all values of $z \in \mathbb{S}^1 \setminus \{\pm\mathbf{e}_1\}$. We can see from κ_{03} that the virtual control signal decreases linearly as the angle goes to zero, but the convergence rate is even larger for κ_{02}. By increasing λ even closer to 1, the steepness of the control signal close to $z = -\mathbf{e}_1$ also increases. Also, the gain $K_p > 0$ sets the magnitude of the angular rate. Hence, both λ and K_p are parameters that can be tuned according to the dynamical system it is applied on.

To illustrate how the different virtual controls affects the change of z along the unit circle, the vector fields for $\dot{z}$ is plotted in Figure 3.5:

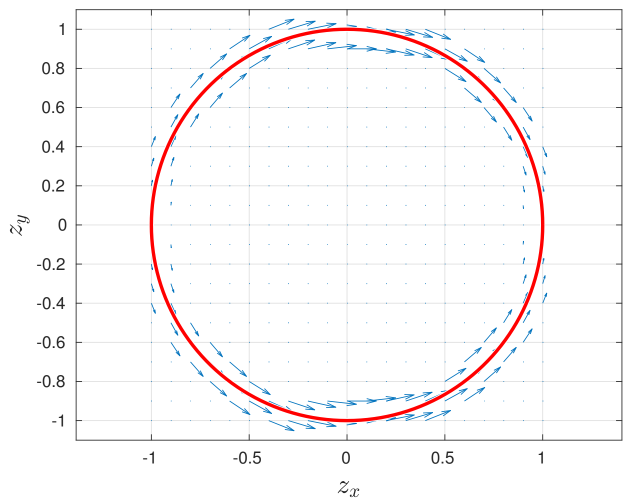

(a) Velocity vector plot of $\dot{z}$ with virtual control κ_{00}

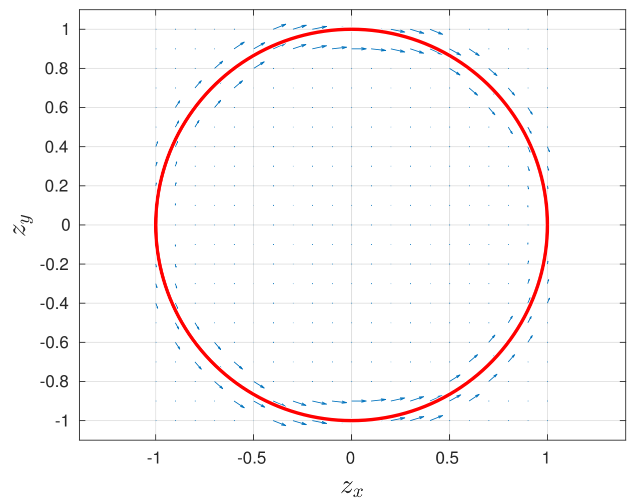

(b) Velocity vector plot of $\dot{z}$ with virtual control κ_{01}

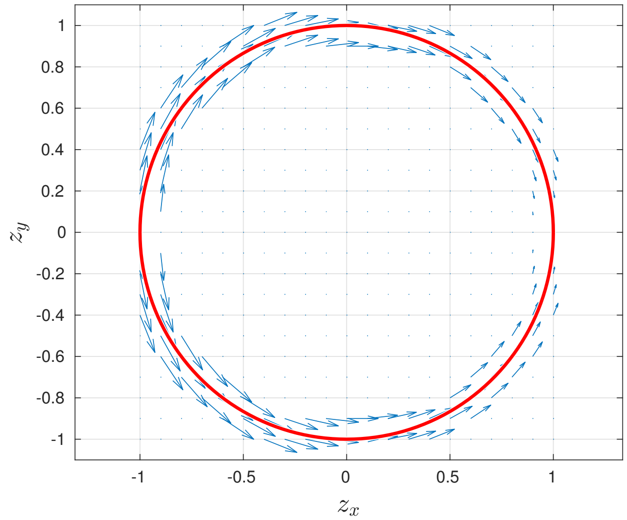

(c) Velocity vector plot of $\dot{z}$ with virtual control κ_{02}

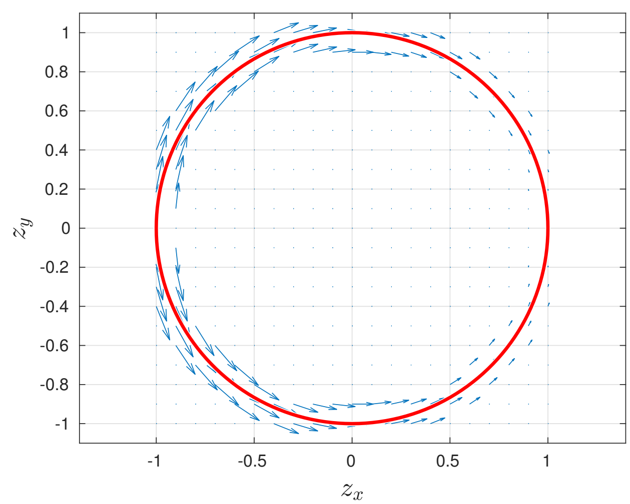

(d) Velocity vector plot of $\dot{z}$ with virtual control κ_{03}

Figure 3.5: Velocity vector fields of the resulting z dynamics for different potential functions

Where $\dot{z}$ is plotted as a vector field in the neighbourhood of $\mathbb{S}^1$ to better illustrate the gradients of z, but in reality the only possible gradients are the one on $\mathbb{S}^1$. When using the virtual control κ_{00} from the potential function P_{00}, we can see that the magnitudes of the gradients are largest for $z = \pm\mathbf{e}_2$, and goes closer to zero in magnitude when moving closer to $\pm\mathbf{e}_1$. This might be unwanted and lead to a slow convergence towards $z = \mathbf{e}_1$ for points in the left half plane, and therefore the potential function P_{01} was introduced. When using P_{01} as the potential function and κ_{02} as virtual control, the resulting gradients for z is proportionally larger the longer along the arc length the point on the circle is from $\mathbf{e}_1$, and will induce larger control forces when included in a control system.

To illustrate this, the feedback controls κ_{00}, κ_{01}, κ_{02} and κ_{03} were applied to a model on $\mathbb{S}^1$ with $K_p = 0.5, \lambda = 0.99 \implies L = 0.3498$ with initial angles in the range $\psi_0 \in [15°, 180°]$ and desired angle $\psi_d = 0°$. This was simulated for 20 seconds to see the difference in the response using the proposed potential functions. The results are shown in Figure 3.6:

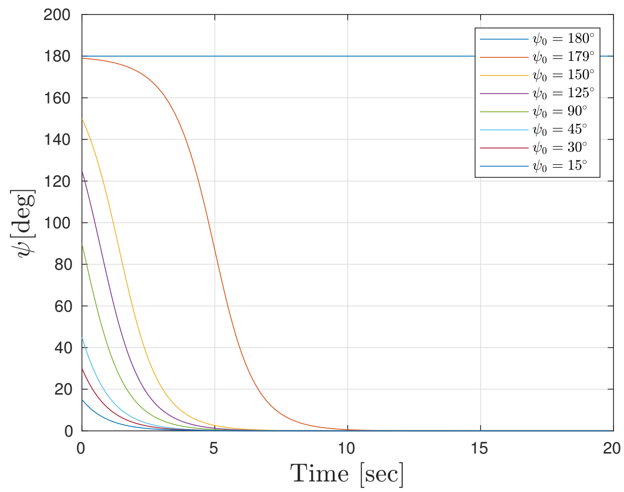

(a) Response when using virtual control κ_{00}

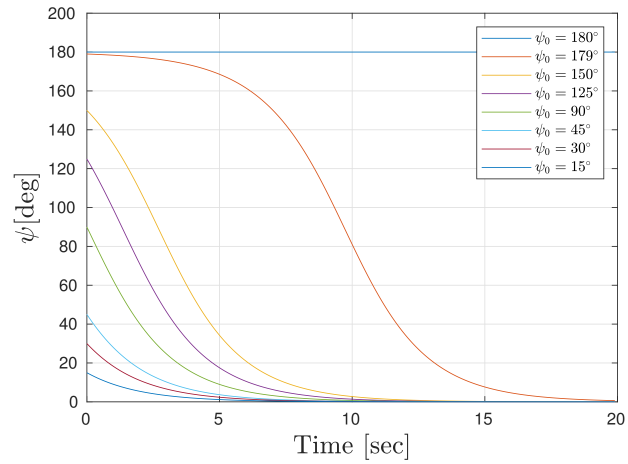

(b) Response when using virtual control κ_{01}

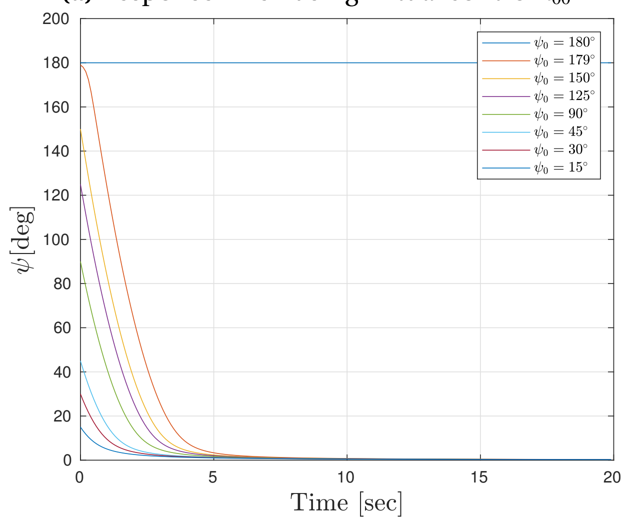

(c) Response when using virtual control κ_{02}

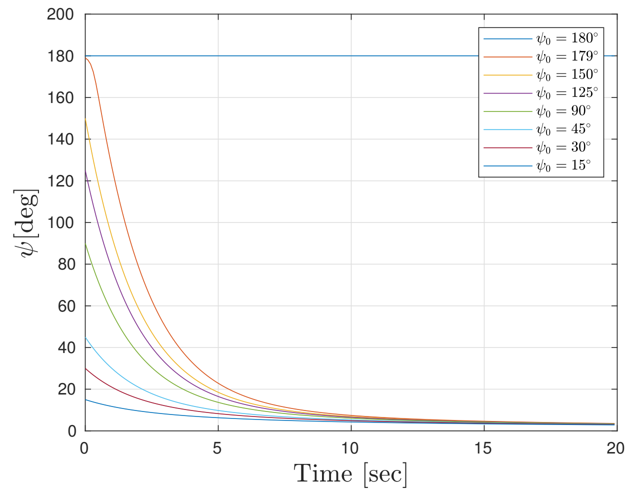

(d) Response when using virtual control κ_{03}

Figure 3.6: Comparison of response from different virtual controls

Where the responses for negative initial angles are the same, but mirrored along the x-axis. This clearly shows the importance of a adequate potential function and virtual control to obtain fast convergence. Note that for the initial angle offset of $180°$, none of the controllers will be able to reach $z = \mathbf{e}_1$. This motivates for a hybrid structure avoiding this unstable equilibrium.

3.3.4 Hybrid Control of Planar Rotations

As seen from the previous subsection, the virtual control which resulted in the most stable response, both in terms of convergence rate and transient response, was κ_{02}. It is therefore chosen to proceed with this control and potential function P_{01} to deduce the hybrid control law from these, as the hybrid control properties will be similar. The idea is to design a hybrid structure as described in section 3.3.2 with two potential functions P_1 and P_2. In these functions, the peak is shifted such that the peak of P_1 is in $\mathcal{D}_1$ and the peak of P_2 is in $\mathcal{D}_2$. By a Lyapunov-based approach that relies on switching between stabilizing control laws, one can make sure that the state *flows* towards one stable equilibrium point on $\mathbb{S}^1$ (i.e $\mathcal{A}_0$) through the flow sets C_1 and C_2.

The design of the control law relies on angular *stretching* of the manifold to form a diffeomorphism that maintains the element's norm and keeps it within its manifold. In order to shift the critical point $\bar{z}_P = -\mathbf{e}_1$ to apply hybrid heading control on $\mathbb{S}^1$, the following functions must be applied, according to Mayhew and Teel (2010):

The amount of rotation is controlled by a gain $k \in \mathbb{R}$ and potential function $P \in \mathscr{P}$. Let $\Phi : \mathbb{S}^1 \times \mathbb{R} \times \mathscr{P} \to \mathrm{SO}(2)$ be the *exponential map* Φ, defined as:

$$\Phi(z,k,P) = \begin{bmatrix} \cos(\omega) & -\sin(\omega) \\ \sin(\omega) & \cos(\omega) \end{bmatrix}, \qquad \omega = kP(z)S \tag{3.31}$$

where k must satisfy a mild bound. Next, define $\mathcal{T} : \mathbb{S}^1 \to \mathbb{S}^1$ as:

$$\mathcal{T}(z,k,P) = \Phi(z,k,P)z \tag{3.32}$$

which applies the rotation to z. For notational simplicity, $\mathcal{T}(z) = \mathcal{T}(z,k,P)$ whenever suitable. Next, define the Jacobian of $\mathcal{T}$ (with some other properties) as:

$$\begin{aligned} \mathcal{J}_{\mathcal{T}}(z,k,P) &= \Phi(z,k,P)(I + kSz\nabla_z P^\top(z)) \\ \det(\mathcal{J}_{\mathcal{T}}(z,k,P)) &= 1 + k\langle \nabla_z P(z), Sz\rangle \\ \mathcal{J}_{\mathcal{T}}(z,k,P)Sz &= \det(\mathcal{J}_{\mathcal{T}}(z))S\mathcal{T}(z) \end{aligned} \tag{3.33}$$

where I is the identity matrix and $\det(\mathcal{J}_{\mathcal{T}}(z))$ denotes the determinant of $\mathcal{J}_{\mathcal{T}}(z)$. We can express the derivative along the unit circle of a modified potential function $(P \circ \mathcal{T}) = P(\mathcal{T}(z,k,P)) : \mathbb{S}^1 \to \mathbb{R}_{\geq 0}$ with a shifted critical point as:

$$\langle \nabla_z (P \circ \mathcal{T})(z), Sz\rangle = \det(\mathcal{J}_{\mathcal{T}}(z))\langle \nabla_z P(\mathcal{T}(z)), S\mathcal{T}(z)\rangle \tag{3.34}$$

So $\mathcal{T}$ is a global diffeomorphism if k satisfies:

$$|k| < \frac{1}{\max\{\|\nabla_z P(z)\| : z \in \mathbb{S}^1\}} \tag{3.35}$$

meaning that $\mathcal{T}$ is a mathematical mapping of a state on the smooth manifold $\mathbb{S}^1$ to $\mathbb{S}^1$ (rotation) such that it is invertible and maps one differentiable manifold to another such that both functions and its inverse are smooth. With this function we can construct new potential functions and control laws for $\mathbb{S}^1$.

The indexed diffeomorphism $\mathcal{T}_q(z) : \mathbb{S}^1 \to \mathbb{S}^1$, the indexed potential function $P_q(z) : \mathbb{S}^1 \to [0,1]$ and its minimum over $\mathcal{Q}$, $\mathcal{M} : \mathbb{S}^1 \to [0,1]$ are defined as:

$$\mathcal{T}_q(z) = \mathcal{T}(z, k_q, P_q^*) \tag{3.36}$$
$$P_q(z) = P(\mathcal{T}_q(z)) \tag{3.37}$$
$$\mathcal{M}(z) = \min\{P_q(z) : q \in Q\} \tag{3.38}$$

Hence, with $P_q^* = P = P_{01}$ as the base potential function, the modified versions of these can be expressed as:

$$\begin{aligned} P_1(z) &= P_{01}(\mathcal{T}_1(z)), \qquad & \mathcal{T}_1(z) &= \mathcal{T}(z, k_1, P_{01}) \\ P_2(z) &= P_{01}(\mathcal{T}_2(z)), \qquad & \mathcal{T}_2(z) &= \mathcal{T}(z, k_2, P_{01}) \end{aligned} \tag{3.39}$$

and since $\max\{\|\nabla_z P_{01}(z)\| : z \in \mathbb{S}^1\} = \frac{\sqrt{1-\lambda^2}}{\lambda L}$, we choose k_1 and k_2 as:

$$k_1 = 0.495\frac{\sqrt{1-\lambda^2}}{\lambda L}, \qquad k_2 = -k_1 \tag{3.40}$$

such that $\mathcal{T}$ is a global diffeomorphism. Then, using $\lambda = 0.99$ gives the potential functions shown in Figure 3.7:

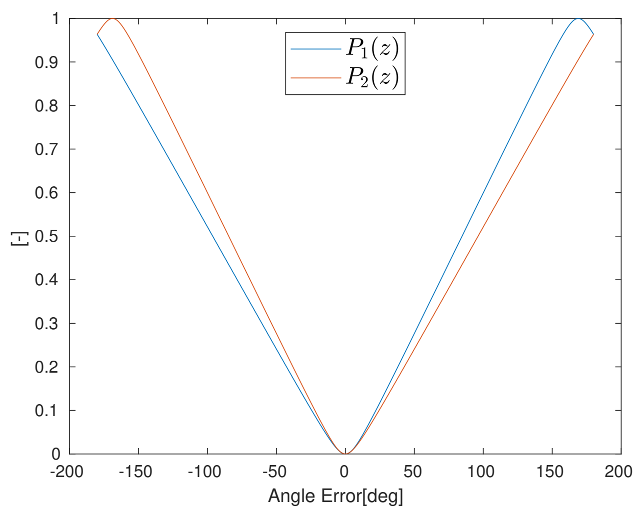

Figure 3.7: Resulting manifold of P_1 and P_2

Here, we can see that the peak of P_1 and P_2 is at approximately $\theta = \pm 169°$, while still having the stable equilibrium at $z = \mathbf{e}_1 (\theta = 0°)$. Now that the hybrid potential functions P_1 and P_2 are defined, the next step is to find the associated controls $\kappa_{\mathcal{T}_1}(z) \in \mathscr{C}(P_1)$ and $\kappa_{\mathcal{T}_2}(z) \in \mathscr{C}(P_2)$ such that the conditions (C1) and (C2) holds. A modification of an original control $\kappa \in \mathscr{C}(P)$ suitable for $(P \circ \mathcal{T})$ is denoted $\kappa_{\mathcal{T}} \in \mathscr{C}(P \circ \mathcal{T})$, and can be expressed as:

$$\kappa_{\mathcal{T}}(z) := \frac{\kappa(\mathcal{T}(z))}{\det(\mathcal{J}_{\mathcal{T}}(z))} \tag{3.41}$$

Hence, a modification of the original control $\kappa_{02} \in \mathscr{C}(P_{01})$ gives a control for $(P_{01} \circ \mathcal{T})$ as $\kappa_{\mathcal{T}} \in \mathscr{C}(P_{01} \circ \mathcal{T})$:

$$\kappa_{\mathcal{T}}(z) = \frac{\kappa_{02}(\mathcal{T}(z))}{\det(\mathcal{J}_{\mathcal{T}}(z))} \tag{3.42}$$

Meaning that for $q \in Q = 1, 2$ we have:

$$\kappa_{\mathcal{T}_q}(z) = \frac{\kappa_{02}(\mathcal{T}_q(z))}{\det(\mathcal{J}_{\mathcal{T}_q}(z))} \tag{3.43}$$

where $\mathcal{T}_q(z) = \mathcal{T}(z, k_q, P_{01})$. A formal definition of such system is defined by letting $\mathscr{D} = \mathscr{P} \times \mathscr{C} \times (\mathbb{R} \times \mathscr{P})^N \times \mathbb{R}_{\geq 0}$. Then, letting $Q = \{1, ..., N\}$ we can define the *tuple* $\mathcal{H}$ as:

$$\mathcal{H} = \left(P, \kappa, \{(k_q, P_q^*)\}_{q=1}^N, \delta\right) \in \mathscr{D} \tag{3.44}$$

The parameter δ is called the *synergy gap*, which must satisfy the bound $0 < \delta < \mu$ in order for $\mathcal{T}_q(z)$ to be a diffeomorphism, where:

$$\mu = 1 - \max_{q \in Q} \mathcal{M}(\mathcal{T}_q^{-1}(P^{-1}(1)) \tag{3.45}$$

Where $P^{-1}(1) = \bar{z}_P$ and $\mathcal{T}_q^{-1}(P^{-1}(1)) = \mathcal{T}_q^{-1}(\bar{z}_P)$ is the solution for z in $\mathcal{T}_q(z) = \bar{z}_P$, which for this application are the points along the unit circle where $P_q(z) = 1$.

Hence, the tuple $\mathcal{H}_{01}$ with potential function $P = P_{01}$, $Q = \{1, 2\}$, control $\kappa = \kappa_{02}$ with k_q as defined in (3.40) with the same base potential functions for both P_1^* and P_2^*, i.e $P_q^* = P_{01}$, is:

$$\mathcal{H}_{01} = (P_{01}, \kappa_{02}, \{k_1, P_{01}\}, \{k_2, P_{01}\}, \delta_{01}) \in \mathscr{D} \tag{3.46}$$

The value of μ for $\mathcal{H}_{01}$ is calculated offline to be $\mu_{01} = 0.0954974$ and therefore $\delta_{01} = 0.09$ is chosen to be the synergy gap for this application.

Placing these conditions in a hybrid structure, yields:

$$C = \{(z, q) \in \mathbb{S}^1 \times Q : \mathcal{M}(z) - P_q(z) \geq -\delta_{01}\} \tag{3.47}$$

$$\mathcal{D} = \{(z, q) \in \mathbb{S}^1 \times Q : \mathcal{M}(z) - P_q(z) \leq -\delta_{01}\} \tag{3.48}$$

Next, we define the set-valued mapping $g(z)$ as $g : \mathbb{S}^1 \rightrightarrows Q$ when $(z, q) \in \mathcal{D}$:

$$g(z) = \{q \in Q : P_q(z) = \mathcal{M}(z)\} \tag{3.49}$$

i.e switching q such that z flows along the flow set with the minimum associated potential function to ensure the potential function is strictly decreasing during flows. Then, the *tuple* $\mathcal{H} \in \mathscr{D}$ generate the dynamic system for $\xi = (z, q)$:

$$\dot{\xi} = F(\xi), \qquad \xi \in C \tag{3.50a}$$

$$\xi^+ \in G(\xi), \qquad \xi \in \mathcal{D} \tag{3.50b}$$

where

$$F(z, q) = \begin{bmatrix} f(z, \kappa_{\mathcal{T}_q}(z)) \\ 0 \end{bmatrix}, \qquad G(z, q) = \begin{bmatrix} z \\ g(z) \end{bmatrix} \tag{3.51}$$

with $f(z, \kappa_{\mathcal{T}_q}(z)) = \kappa_{\mathcal{T}_q}(z) S z$. Figure 3.8 shows the synergy gap $\delta_{01} = 0.09$ with $\mathcal{M}(z) - P_q(z)$ for $Q = \{1, 2\}$.

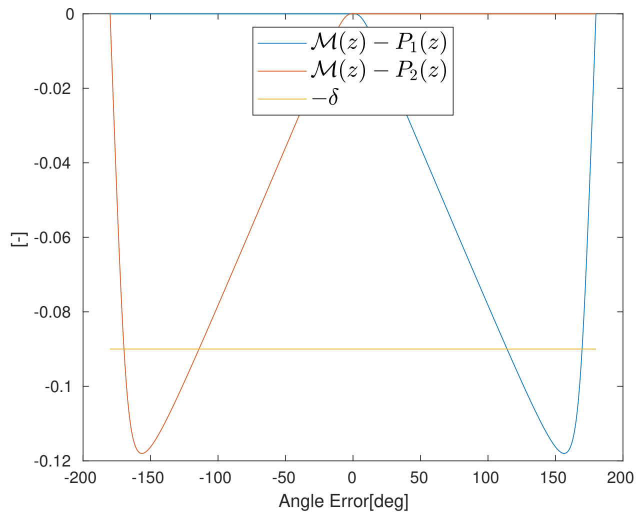

Figure 3.8: Manifold of $\mathcal{M}(z) - P_q(z)$ for $Q \in \{1, 2\}$

We can see that for $\{\theta \in [114, 170]) \times (q = 1)\}$, the value of q will switch from 1 to 2, and for $\{\theta \in [-170, -114]) \times (q = 2)\}$, the value of q will switch from 2 to 1. We therefore avoid the unstable equilibria for $P_1(z)$ and $P_2(z)$, which were located at approximately $\pm 169°$. Hence, we can define the potential function $V_0(z, q)$ and control $\kappa_0(z, q)$ as:

$$V_0(z, q) = P_q(z), \qquad \kappa_0(z, q) = \kappa_{\mathcal{T}_q}(z) \tag{3.52}$$

We can compute the change in V_0 along flows as in (3.53), which by the definition in (3.41) satisfies (C1) and (C2) is negative for all $z \in C \setminus \{\mathbf{e}_1\}$, and zero for $z = \mathbf{e}_1$:

$$\dot{V}_0(z, q) = \langle \nabla_z V_0(\xi), F(\xi) \rangle = \langle \nabla_z (P_{01} \circ \mathcal{T}_q)(z), S z \rangle \kappa_{\mathcal{T}_q}(z) \begin{cases} < 0, & (z, q) \in C \setminus \mathcal{A}_0 \\ = 0, & (z, q) \in \mathcal{A}_0 \end{cases} \tag{3.53}$$

Furthermore, defining $\mathcal{E}_{01} := \{(z, q) \in \mathbb{S}^1 \times Q : \langle \nabla_z V_0(\xi), F(\xi) \rangle \kappa_0(\xi) = 0\}$, we see that the set $\mathcal{E}_{01} \cap C = \mathcal{A}_0$. Hence, $\mathcal{A}_0$ is stable during flows. Evaluating the change of $V_0(z, q)$ over jumps, it follows that

$$V_0(G(\xi)) - V_0(\xi) = \mathcal{M}(z) - V_0(z, q) \tag{3.54}$$

and by definition of $\mathcal{D}$, it follows that $V_0(G(\xi)) - V_0(\xi) \leq -\delta_{01}$ for all $\xi \in \mathcal{D}$. Hence, we can assert that $\mathcal{A}_0$ is globally asymptotically stable (G. Sanfelice et al. (2008), Corollary 7.7).

To shorter further notation, we define

$$\left.\begin{matrix} \dot{V}_0(z, q) \\ V_0(z, q)^+ \end{matrix}\right\} = -\rho_0(z, q) < 0, \qquad (z, q) \in (C \cup \mathcal{D}) \setminus \mathcal{A}_0 \tag{3.55}$$

The control along the unit circle for $(z, q) \in \mathbb{S}^1 \times Q$ with $K_p = 0.5$ and $\lambda = 0.99$ is shown in Figure 3.9a, and the resulting potential function derivatives in Figure 3.9b.

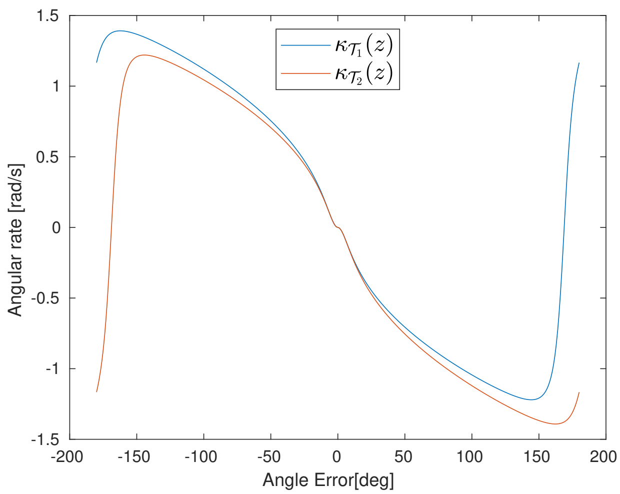

(a) Manifold of modified κ for $Q \in \{1, 2\}$

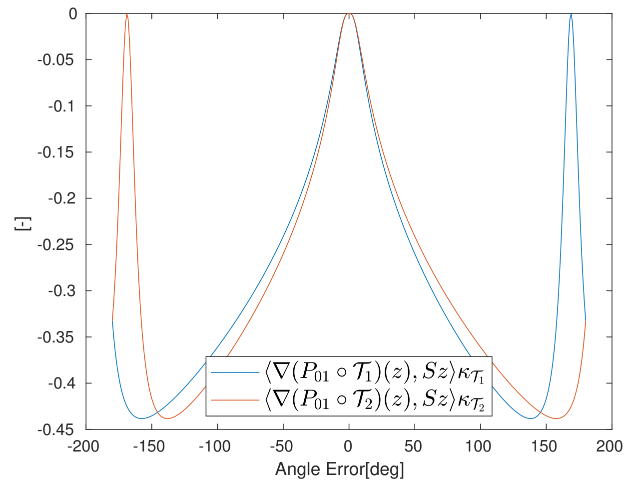

(b) Derivatives of potential functions with different controls

Figure 3.9: Manifolds of hybrid virtual controls and their derivatives

Here, $\kappa_{\mathcal{T}_1}(z)$ and $\kappa_{\mathcal{T}_2}(z)$ are continuous differentiable functions on $\mathbb{S}^1$. Compared to $\kappa_{02}(z)$ in Figure 3.4a we can see that the virtual control signal at the original unstable equilibrium at $z = -\mathbf{e}_1$ now has a value different from 0, which means it will flow either way along the unit circle towards the stable equilibrium $z = \mathbf{e}_1$, depending on the value of q. Figure 3.9b illustrates this, where we can observe that $\dot{P}_q(z)$ is zero inside the jump set illustrated in Figure 3.8, and we will therefore always have $\dot{P}_q < 0$(except in the stable equilibrium where $\dot{P}_q = 0$) during all flows. The resulting velocity vector plots together with the bounds between the jump- and flow sets are shown in Figure 3.10:

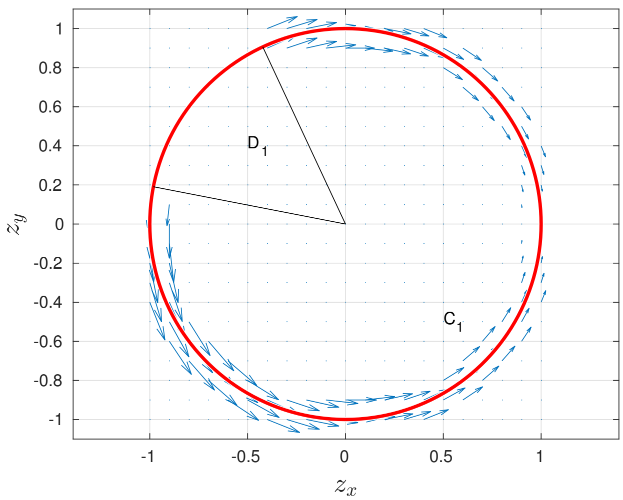

(a) Velocity vector plot of $\dot{z}$ with virtual control $\kappa_{\mathcal{T}_1}$

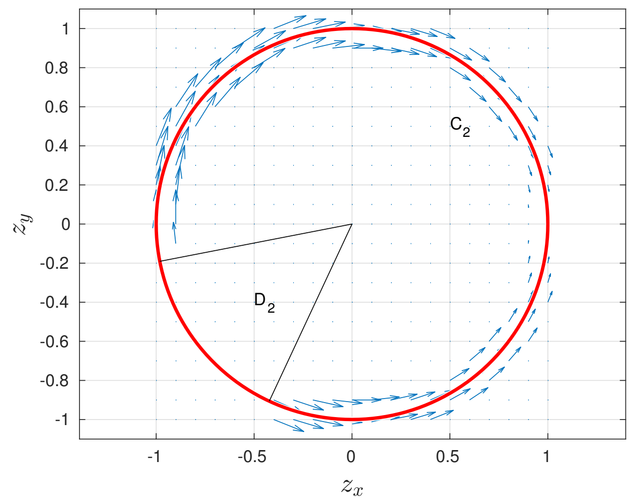

(b) Velocity vector plot of $\dot{z}$ with virtual control $\kappa_{\mathcal{T}_2}$

Figure 3.10: Velocity vector fields of the resulting z dynamics for κ_1 and κ_2

Therefore, we can conclude this subsection with having defined a hybrid system that ensures $\mathcal{A}_0$ to be globally asymptotically stable for all $\xi = (z,q) \in \mathbb{S}^1 \times Q$. However, as the hybrid feedback $\kappa_0(z,q) = \kappa_{\mathcal{T}_q}$ is discontinuous during jumps, it cannot be directly applicable to a dynamical system to induce control forces, torques and derivatives of these. The following section will introduce a way of "smoothning" the feedback, while still retain the GAS properties.

3.4 Synergistic Lyapunov Functions

The use of synergistic potential functions can be used to design smooth hybrid feedback laws that achieves global asymptotic stabilization of a point on a compact manifold such as $\mathbb{S}^1$, $\mathbb{S}^2$ and $SO(3)$. By using a family of synergistic potential functions, simple hybrid controllers can be designed by choosing the corresponding feedback control law to the potential function with the lowest value as a type of hysteresis to ensure global asymptotic stability.

3.4.1 Synergistic Lyapunov Function and Feedback

Mayhew et al. (2011) generalizes these functions into synergistic Lyapunov functions which enables "smoothing" hybrid feedback such that point stabilization for non-contractible spaces is possible. These Lyapunov functions need to decrease both during jumps and flows, also in the case of arbitrary switching. Such function can be designed for the control system

$$\left.\begin{aligned} \dot{z} &= \phi(z,q) + \psi(z,q)\kappa(z,q) \\ \dot{q} &= 0 \end{aligned}\right\} (z,q) \in M_0 \times Q \tag{3.56}$$

with ϕ and ψ being smooth functions, $\kappa \in \mathbb{R}^m$ is the control input, the set $M_0 \subset \mathbb{R}^n$ is closed, and Q is discrete. A smooth Lyapunov function which maps values from the state into a non-negative real number $V : M_0 \times Q \to \mathbb{R}_{\geq 0}$ and feedback $\omega = \kappa : M_0 \times Q \to \mathbb{R}^m$ forms a *synergistic Lyapunov and feedback pair candidate* relative to the compact set $\mathcal{A}_0 \subset M_0 \times Q$ if:

- $\forall r \geq 0$, $\{(z,q) \in M_0 \times Q : V(z,q) \leq r\}$ is compact
- V is positive definite with respect to $\mathcal{A}$
- For all possible states $(z,q) \in M_0 \times Q$, the Lyapunov function is not increasing $\langle \nabla_z V(z,q), \phi(z,q) + \psi(z,q)\kappa(z,q)\rangle \leq 0$

As the gradient of the Lyapunov function can be zero, we define $\mathcal{W}_0$ to be the set where the gradient $\nabla_z V(z,q)$ is zero, that is,

$$\mathcal{W}_0 := \left\{(z,q) \in M \times Q : \psi(z,q)^\top \nabla_z V(z,q) = 0\right\} \tag{3.57}$$

and if the combination of $\phi(z,q)$ and $\psi(z,q)\kappa$ gives a derivative of $V(z,q)$ to be zero:

$$\mathcal{E}_0 := \{(z,q) \in M_0 \times Q : \langle \nabla_z V(z,q), \phi(z,q) + \psi(z,q)\kappa(z,q)\rangle = 0\} \tag{3.58}$$

Note that for the system described in (3.50), we have $\phi(z,q) = 0$, $\psi(z,q) = Sz$, $m = 1$, $\kappa(z,q) = \kappa_0(z,q)$, $M_0 = \mathbb{S}^1$, $Q = \{1,2\}$, $r = 1$, $V = V_0(z,q)$, $\mathcal{E}_0 = \mathcal{W}_0 = \mathcal{E}_{01}$. This will be applied in Section 5.2.

This pair (V,κ) is called the *synergistic Lyapunov function feedback pair* if $\mu(V,\kappa) > \delta > 0$, as defined in the previous section. Hence, (V_0,κ_0) is a synergistic Lyapunov function feedback pair with the synergy gap μ_{01} exceeding δ_{01}.

3.4.2 Backstepping

This section will present a way of smoothing $\kappa_0(z,q)$ before introducing it as a virtual control in a dynamical system with backstepping to deduce the control input. The deduced state $p \in \mathbb{R}^L$ acts as a smoothing replacement of q.

Defining the state $\zeta = (z,\omega,p)$ with controls $u \in \mathbb{R}^m$, we consider the control system:

$$\left.\begin{aligned} \dot{\zeta} &= \phi_1(\zeta,q) + \psi_1(\zeta,q)u \\ \dot{q} &= 0 \end{aligned}\right\} \qquad (\zeta,q) \in M_1 \times Q \tag{3.59}$$

Where ϕ_1 and ψ_1 are defined as:

$$\phi_1(\zeta,q) = \begin{bmatrix} \phi_0(z,q) + \psi_0(z,q)\omega \\ 0 \\ v(z,p,q) \end{bmatrix}, \qquad \psi_1(\zeta,q) = \begin{bmatrix} 0 \\ 1 \\ 0 \end{bmatrix} \tag{3.60}$$

We can construct a new synergistic Lyapunov function and feedback pair (V_1,κ_1) with synergy gap exceeding $\delta > 0$ by reducing the system to

$$\left.\begin{aligned} \dot{z} &= \phi_0(z,q) + \psi_0(z,q)\omega \\ \dot{q} &= 0 \end{aligned}\right\} \qquad (z,q) \in M_0 \times Q \tag{3.61}$$

with controls $\omega \in \mathbb{R}^m$. For a synergistic Lyapunov function and feedback pair (V_0,κ_0) relative to the compact set $\mathcal{A}_0 \subset M_0 \times Q$, we assume that $\kappa_0 : M_0 \times Q \to \mathbb{R}^m$ wan be written as linear in some function of q. By letting $\vartheta(q) : M_0 \to \mathbb{R}^{m\times L}$ be a smooth function and $\sigma : Q \to \mathbb{R}^L$, where $L \geq 1$, we have

$$\kappa_0(z,q) = \vartheta(z)\sigma(q) \tag{3.62}$$

Hence, by letting $\sigma(q) = \mathbf{e}_q$ be the q'th unit vector and $\vartheta(z) = [\kappa_0(z,1),...,\kappa_0(z,N)]$, (3.62) holds. The new set we now want to be stable is:

$$\mathcal{A}_1 := \{(\zeta,q) \in M_1 \times Q : (z,q) \in \mathcal{A}_0, p = \sigma(q), \omega = \kappa_0(z,q)\} \tag{3.63}$$

We then define the Lyapunov function

$$V_1(\zeta,q) := V_0(z,q) + \frac{1}{2}|p-\sigma(q)|^2_{\Gamma_1} + \frac{1}{2}|\omega - \vartheta(z)p|^2_{\Gamma_2} \tag{3.64}$$

where $|\xi|^2_\Gamma = \xi^\top \Gamma \xi$ for a symmetric, positive definite matrix Γ. $\Gamma_1 \in \mathbb{R}^{L\times L}$ and $\Gamma_2 \in \mathbb{R}^{m\times m}$ must be defined such that

$$\mu_{\mathcal{W}}(V_0, \kappa_0) - \frac{1}{2}\lambda_{max}(\Gamma_1) \max_{s,q\in Q} |\sigma(s) - \sigma(q)|^2 > \delta \tag{3.65}$$

Where $\lambda_{max}(\Gamma_1)$ denotes the largest eigenvalue for Γ_1. Then, let $\theta_1, \theta_2 : \mathbb{R}_{\geq 0} \to \mathbb{R}_{\geq 0}$ be continous, positive definite functions, and let the smooth functions $\Theta_1 : \mathbb{R}^L \to \mathbb{R}^L$ and $\Theta_2 : \mathbb{R}^m \to \mathbb{R}^m$ satisfy

$$v^\top \Gamma_i \Theta_i(v) + \Theta_i(v)^\top \Gamma_i v \leq -\theta_i(|v|), \qquad \forall i \in \{1, 2\} \tag{3.66}$$

Let $\vartheta_i(z) = \vartheta(z)\mathbf{e}_i$ and define:

$$\begin{aligned}
\kappa_1(\zeta, q) =&\Theta_2(\omega - \vartheta(z)p) - \Gamma_2^{-1}\psi_0(z, q)^\top \nabla_z V_0(z, q) \\
&+ \sum_{i=1}^{L} \mathbf{e}_i^\top p \mathscr{D}\vartheta_i(z)(\phi_0(z, q) + \psi_0(z, q)\omega) + \vartheta(z)v(z, p, q) \\
v(z, p, q) =&\Theta_1(p - \sigma(q)) - \Gamma_1^{-1}\vartheta(z)^\top \psi_0(z, q)^\top \nabla_z V_0(z, q)
\end{aligned} \tag{3.67}$$

Where $\mathscr{D}$ denote the Jacobian matrix, where for a smooth function $\alpha(z, q)$, the ij-th entry is $\frac{\partial \alpha_i(z,q)}{\partial z_j}$. We get that for all $(\zeta, q) \in M_1 \times Q$, the following holds:

$$\begin{aligned}
\dot{V}_1 =&\langle \nabla_\zeta V_1(\zeta, q), \phi_1(\zeta, q) + \psi_1(\zeta, q)\kappa_1(\zeta, q)\rangle \\
=&\langle \nabla_z V_0(z, q), \phi_0(z, q) + \psi_0(z, q)\omega\rangle - \frac{1}{2}\theta_1(|p - \sigma(q)|) - \frac{1}{2}\theta_2(|\omega - \vartheta(z)p|) \\
&- \langle \nabla_z V_0(z, q), \psi_0(z, q)\vartheta(z)(p - \sigma(q))\rangle - \langle \nabla_z V_0(z, q), \psi_0(z, q)(\omega - \vartheta(z)p)\rangle \\
=&\langle \nabla_z V_0(z, q), \phi_0(z, q) + \psi_0(z, q)\vartheta(z)\sigma(q)\rangle - \frac{1}{2}\theta_1(|p - \sigma(q)|) - \frac{1}{2}\theta_2(|\omega - \vartheta(z)p|) \\
\leq&0
\end{aligned} \tag{3.68}$$

The synergy gap is then:

$$\mu(V_1, \kappa_1) = \mu_{\mathcal{W}}(V_0, \kappa_0) - \frac{1}{2}\lambda_{max}(\Gamma_1) \max_{s,q\in Q} |\sigma(s) - \sigma(q)|^2 > \delta \tag{3.69}$$

Thus, the pair (V_1,κ_1) is a synergistic Lyapunov function and feedback pair relative to the compact set $\mathcal{A}_1$ with a synergy gap exceeding δ.

Chapter 4

Simulations and Experimental Setup

In this chapter the procedure and setup for testing of the hybrid control system is described. During the project, the testing has been done in four ways, in this order:

- MATLAB simulations where it is assumed that the desired velocities are achieved
- MATLAB simulations where it is assumed that the desired thrust is achieved. The forces are applied to a 3DOF mathematical vessel model of CSAD
- Hardware In The Loop(HIL) tests with actuator dynamics and thrust allocation of CSAD
- Physical experiments in the Marine Cybernetics Laboratory with CSAD

4.1 MATLAB and Simulink Simulations

The kinetic and kinematic equations in (2.2) and (2.21) are implemented in Simulink and used for testing of the control algorithms. The Simulink diagram of the dynamics is shown in Figure 4.1. The numeric parameters used for the mass, damping and Coriolis matrices are found in Appendix A.1.

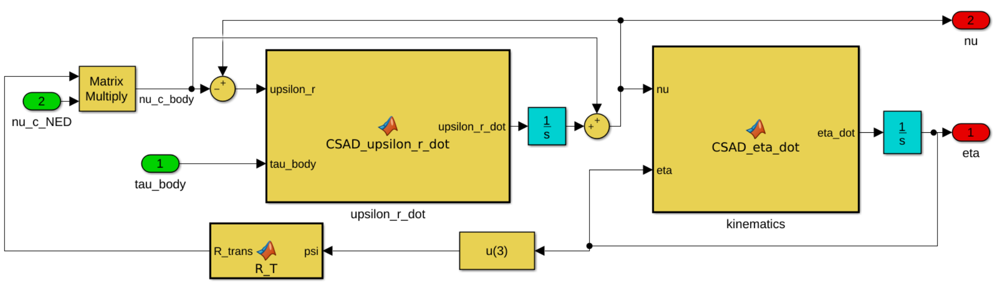

Figure 4.1: 3DOF Simulink model

4.2 Hardware-in-the-loop Simulations

After making sure the controller works in the simulation environment with Simulink, the controller is prepared to fit the laboratory vessel by performing HIL-simulations. Simulink models can be used as a code generator to fit the on-board computer on the vessel. By building the Simulink system to code in the programming language C, the system can be run in real time. The custom Veristand in- and out-ports in Simulink is used to transfer data in and out of the control system. For HIL-testing, the in and out-ports of the 3DOF vessel model is mapped as Veristand ports, and redirected back to the Simulink diagram as position and heading measurements through the Veristand interface. In theory, a single Simulink diagram could be used for HIL-simulations with an easy mapping, but this complicates the procedure to prepare the system for physical experiments, as it is time consuming to ensure all mappings are correct. To emulate the physical vessel, a HIL-box is used, as shown in Figure 4.2. The generated C-code is uploaded to the box and uses the Veristand in and out-ports to function. A custom monitoring station for starting and stopping simulations, tuning gains plotting and logging is developed in order to control and record the tests. The setup is shown in Figure 4.3.

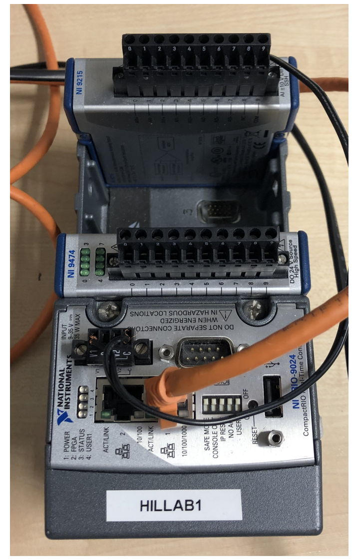

Figure 4.2: HIL box

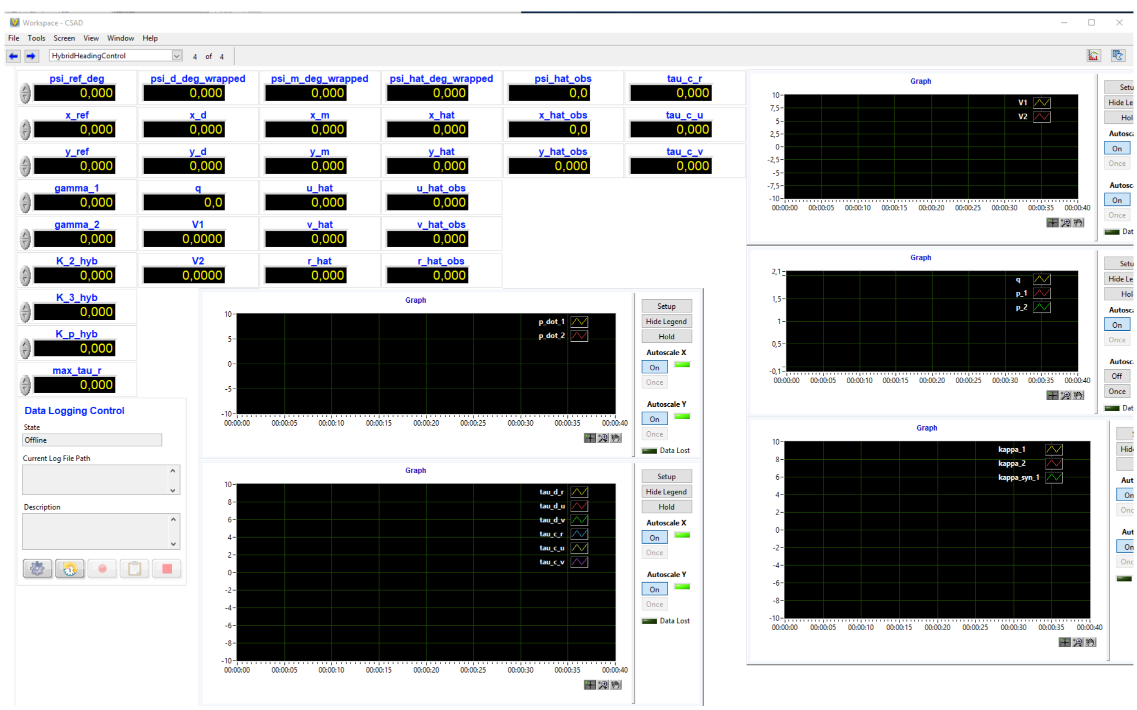

Figure 4.3: Screenshot of the workbench used for monitoring HIL simulations and lab experiments

4.3 Physical Experiments at the Marine Cybernetics Laboratory

The Marine Cybernetics laboratory (MCL, 2017) is a small ocean basin laboratory at the Department of Marine Technology at NTNU. It is relatively small, but suitable for tests of motion control system for model-scale surface vessels, but could also do more specialized hydrodynamic experiments as towing tests. It is equipped with a movable bridge with positioning cameras capable of measuring 6DOF movements of models, as well as a wave maker and two cameras for filming purposes. The basin measures $40[m] \times 6.45[m] \times 1.5[m]$ in length, breadth and depth, respectively, and is displayed in Figure 4.4 together with CSAD.

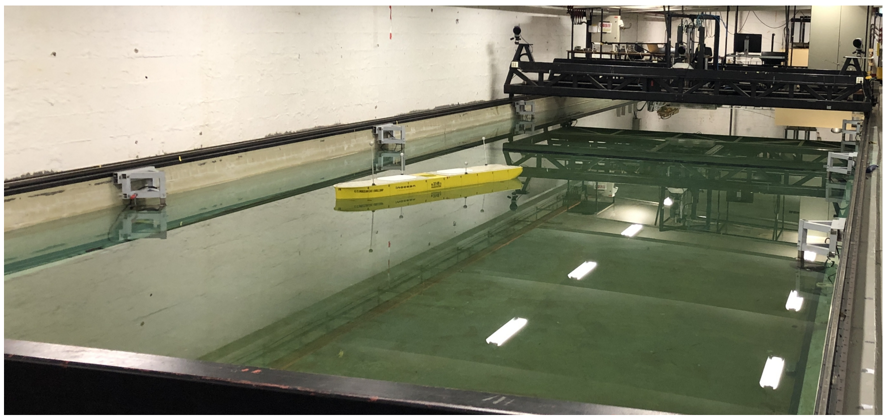

Figure 4.4: The Marine Cybernetics Laboratory

4.3.1 Laboratory Hardware

The lab is equipped with the real-time positioning system Qualisys. It supplies a range of hardware and software products for motion capture and analysis of movement data. The key components are the Oqus cameras and the Qualisys Track Manager (QTM) software. The Oqus system in the lab has three high-speed infrared (IR) cameras, which tracks the IR reflectors orbs fitted on the model scale ships. The experiments can be supervised from the control room with a computer dedicated for the QTM system and a TV connected to the two cameras in the lab. The internal communication between the systems are done over IP on a dedicated WLAN network to allow wireless control of the model-scale ships and transferring of experimental data from the on-board computer. The ship is equipped with a National Instrument CompactRIO (cRIO) embedded computer system for control computation. In addition, a PlayStation 3 (PS3) hand controller is used for manual control or for switching between different control algorithms.

4.3.2 Laboratory Software

In order to communicate with the ship, the lab is equipped with laptops dedicated for each vessel. These laptops have installed LABView Full Development System, MATLAB and Simulink package, as well as the National Instruments complete Veristand software package. Figure 4.5 shows the topology of the communication between the HW and SW components.

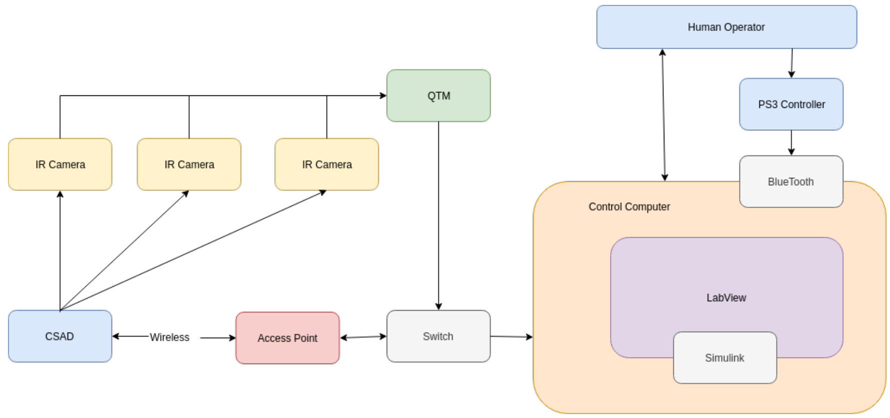

Figure 4.5: Topology of the HW and SW

4.3.3 Experiments with CyberShip Arctic Drillship Model Vessel

The vessel used for experiments in the MCL is the CyberShip Arctic Drillship(NTNU, 2017). The vessel is a 1:90 scale model of Equinor Cat I Arctic Drillship. It is equipped with 6 azimuth thrusters (3 fore and 3 aft), in addition to a moon-pool for turret and mooring lines. The thruster positions are shown in Figure 4.6, the x/y-positions and thrust coefficients K_T and K_Q for each thrusters are shown in Table 4.1, and its main dimensions in Table 4.2.

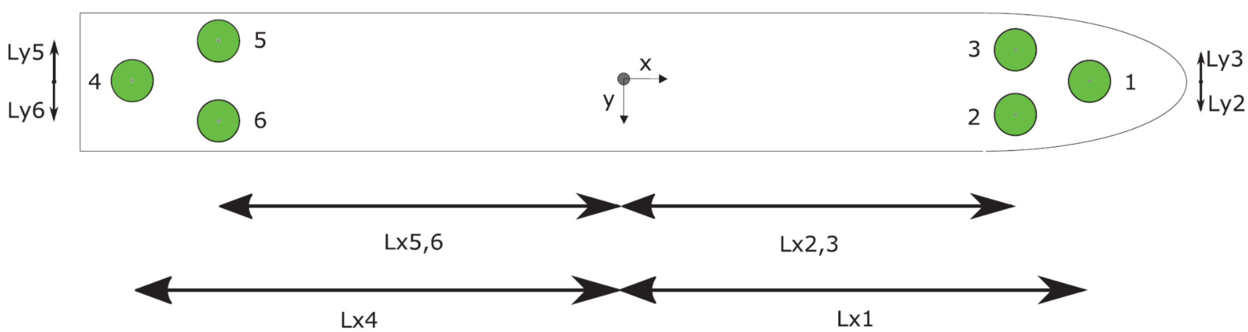

Figure 4.6: Illustration of thruster positions

Table 4.1: Thruster positions and coefficients

Thruster	**Position X**[m]	**Position Y**[m]	K_T	K_Q
Thruster 1	1.0678	0.0	0.3763	0.0113
Thruster 2	0.9344	0.11	0.3901	0.0117
Thruster 3	0.9344	-0.11	0.3776	0.0113
Thruster 4	-1.1644	0.0	0.5641	0.0169
Thruster 5	-0.9911	-0.1644	0.4799	0.0144
Thruster 6	-0.9911	0.1644	0.5588	0.0168

Table 4.2: Main dimensions of CSAD

Dimension	**Value**
LOA	2.578[m]
B	0.440[m]
D	0.211[m]
T	0.133[m]
Δ	127.92[kg]
λ	90

The thrust coefficients was obtained from model tests in Frederich (2016). In this thesis a constrained optimal thrust allocation was developed, and will be the thrust allocation applied in the physical experiments in this thesis. In short, the torque Q_a and thrust T_a obtained from the thrusters can be written as a conventional quadratic thruster characteristics described by Carlton (2012):

$$Q_a = \text{sign}(n) K_Q \rho D^5 n^2 \tag{4.1a}$$

$$T_a = \text{sign}(n) K_T \rho D^4 n^2 \tag{4.1b}$$

where n is the propeller shaft speed, ρ is the water density, and D is the propeller diameter. In a way, this thrust allocation is a "black box", but seemed to work for the purpose of this thesis. For a more detailed explanation on the thrust allocation applied, the reader is referred to Frederich (2016).

After having performed HIL testing, the control system is ready to be tested on board the actual model of the vessel. The setup is the same as in the HIL-simulations. The only difference is the mapping of position and heading measurements, as Qualisys now supplies these. However, what Qualisys does not supply are the velocities. In addition, it become clear that the measurements was highly dependent on a sufficient calibrated camera system. The position and heading measurements had often drop outs and signal freezing, and thus affected the controller performance. Initially it was chosen to apply a Nonlinear Passive Observer(NPO) as described in Fossen (2011), but through both testing in simulations and physical experiments, it falsely estimated the velocities and especially the turning rate. This might have to do with the choosing of gains in the observer, but through many different combinations it turned out to still not be satisfactory enough to use. It was therefore attempted to instead use an Extended Kalman Filter (EKF)(also described in Fossen (2011)) which turned out to provide accurate velocity estimated after a bit of tuning in the noise and covariance matrices. It was also implemented a way to reject false heading measurements, as the Qualisys system sometimes misinterpreted the positions of the four IR orbs in a way that lead to a jumps in the heading measurements. As this is not the main focus of this thesis, it will not be further explained.

Chapter 5

Heading Control on $\mathbb{S}^1$

In this section, a heading control allocation is derived by implementing the synergistic Lyapunov function and feedback laws from Section 3.3. This will be combined with the DP controller in surge and sway as described in Section 2.2 when introduced to physical scale model tests.

5.1 Control Objective

The overall control objective for heading control is to ensure that the heading converges to the desired heading:

$$\lim_{t\to\infty} |\psi(t) - \psi_d(t)| = 0 \tag{5.1}$$

However, this control objective has more than one solution, as $\psi = \psi_d + n360°, n \in \{..., -2, -1, 0, 1, 2, ...\}$ results in the same heading. Therefore, reformulating the control objective to $\mathbb{S}^1$, we have:

$$\lim_{t\to\infty} \left(z^{\psi}(t) - z^{\psi_d}(t)\right) = [0, 0]^\top \iff \lim_{t\to\infty} R\left(z^{\psi_d}(t)\right)^\top z^{\psi}(t) = \mathbf{e}_1 \tag{5.2}$$

which has only one equilibrium.

5.2 Control Design

A simplified kinetic equation for the heading of a ship can be expressed as:

$$\begin{aligned} \dot{\psi} &= r \\ \dot{r} &= \tau_r \end{aligned} \tag{5.3}$$

Where ψ is the heading angle, r is the turning rate and τ_r is the control force in yaw. To implement a hybrid controller for the heading of a vessel on $\mathbb{S}^1$, we define the heading and desired heading on $\mathbb{S}^1$ as z^{ψ} and z^{ψ_d}. The objective is to drive $z^{\psi} \to z^{\psi_d}$, and the heading error is defined on $\mathbb{S}^1$ as $z = R(z^{\psi_d})^\top z^{\psi}$. The kinematic equations then becomes $\dot{z}^{\psi} = Szr$ and $\dot{z}^{\psi_d} = Szr_d$, where r and r_d are the turning rate and desired turning rate of the ship. Defining $\tilde{r} = r - r_d$, the kinematic equation for the error is then $\dot{z} = Sz\tilde{r}$. Choosing the same hybrid setup as in Section 3.3 with the tuple $\mathcal{H}_{01}$ derived from Section 3.3.3, gives the synergistic Lyapunov and feedback pair (V_0, κ_0) with the synergy gap μ_{01} exceeding δ_{01}.

To derive a backstepping controller from this, we use the steps presented in 3.4.2. We note that $\phi_0(z,q) = 0$, $\psi_0(z,q) = Sz$, $u = \tau_r - \dot{r}_d$, $\omega = \tilde{r}$, $M_0 = \mathbb{S}^1$, $Q = \{1,2\}$, $m = 1$ and $L = 2$. The combined system is then:

$$\begin{bmatrix} \dot{\zeta} \\ \dot{q} \end{bmatrix} = \begin{bmatrix} \dot{z} \\ \dot{\tilde{r}} \\ \dot{p} \\ \dot{q} \end{bmatrix} = \left.\begin{bmatrix} Sz\tilde{r} \\ \tau_r - \dot{r}_d \\ v(z,p,q) \\ 0 \end{bmatrix}\right\} \qquad (z,\tilde{r},p,q) \in \mathbb{S}^1 \times \mathbb{R} \times \mathbb{R}^2 \times Q \tag{5.4}$$

Expressing $\kappa_0(z,q)$ according to (3.62):

$$\kappa_0(z,q) = \vartheta(z)\sigma(q) = [\kappa_{\mathcal{T}_1}(z), \kappa_{\mathcal{T}_2}(z)][2-q, q-1]^\top = (2-q)\kappa_{\mathcal{T}_1}(z) + (q-1)\kappa_{\mathcal{T}_2}(z) \tag{5.5}$$

Next, we define the error:

$$\Upsilon_2 = \tilde{r} - \vartheta(z)p \in \mathbb{R} \implies \tilde{r} = \Upsilon_2 + \vartheta(z)p \tag{5.6}$$

And as we want do drive $p \to \sigma(q)$, the error in p is:

$$\tilde{p} = p - \sigma(q) \tag{5.7}$$

$$\dot{\tilde{p}} = \dot{p} - \frac{\partial \sigma(q)}{\partial q}\dot{q} = \dot{p} = v(z,p,q) \tag{5.8}$$

Which gives the error dynamics:

$$\dot{\Upsilon}_2 = \dot{\tilde{r}} - \nabla_z \vartheta(z)\dot{z}p - \vartheta(z)\dot{p} \tag{5.9}$$

Defining the Lyapunov function:

$$V_1(z,q) = V_0(z,q) + \frac{1}{2}\tilde{p}\Gamma_1\tilde{p} + \frac{1}{2}\gamma_2\Upsilon_2^2 \geq 0 \tag{5.10}$$

with $\Gamma_1 = \gamma_1 I^{2\times 2} \implies \Gamma_1^{-1} = \frac{1}{\gamma_1}I$ gives the derivative of V_1 as:

$$\begin{aligned} \dot{V}_1(z,q) &= \nabla_z V_0(z,q) Sz\tilde{r} + \gamma_1 \tilde{p}^\top \dot{\tilde{p}} + \gamma_2 \Upsilon_2 \dot{\Upsilon}_2 \\ &= \nabla_z V_0(z,q) Sz(\Upsilon_2 + \vartheta(z)p) + \gamma_1 \tilde{p}^\top v(z,p,q) + \gamma_2 \Upsilon_2(\dot{\tilde{r}} - \nabla_z \vartheta(z)\dot{z}p - \vartheta(z)\dot{p}) \end{aligned} \tag{5.11}$$

Since $p = \tilde{p} + \sigma(q)$, $\dot{\tilde{r}} = \tau_r - \dot{r}_d$ and $\dot{z} = Sz\tilde{r}$, we get:

$$
\begin{aligned}
\dot{V}_1(z,q) =& \nabla_z V_0(z,q) S z(\Upsilon_2 + \vartheta(z)\tilde{p} + \overbrace{\vartheta(z)\sigma(q)}^{\kappa_0(z,q)}) \\
&+ \gamma_1 \tilde{p}^\top v(z,p,q) + \gamma_2 \Upsilon_2(\tau_r - \dot{r}_d - \nabla_z \vartheta(z) S z \tilde{r} p - \vartheta(z) v(z,p,q)) \\
=& \nabla_z V_0(z,q) S z \kappa_0(z,q) \\
&+ \Upsilon_2(\nabla_z V_0(z,q) S z + \gamma_2(\tau_r - \dot{r}_d - \nabla_z \vartheta(z) S z \tilde{r} p - \vartheta(z)\dot{p})) \\
&+ \tilde{p}^\top(\gamma_1 v(z,p,q) + \vartheta(z)^\top)
\end{aligned}
\tag{5.12}
$$

We recognize $\nabla_z V_0(z,q) S z \kappa_0(z,q)$ as $-\rho(z,q)$ from (3.55). Then, by choosing $v(z,p,q)$ and τ_r as:

$$
v(z,p,q) = \frac{1}{\gamma_1}(-\vartheta(z)^\top - K_3 \tilde{p}), \qquad K_3 > 0 \tag{5.13}
$$

$$
\tau_r = \dot{r}_d + \nabla_z \vartheta(z) S z \tilde{r} p + \vartheta(z) v(z,p,q) - \frac{1}{\gamma_2}\nabla_z V_0(z,q) S z - \frac{1}{\gamma_2} K_2 \Upsilon_2, \qquad K_2 > 0 \tag{5.14}
$$

we get:

$$
\dot{V}_1(z,q) = -\rho_0(z,q) - K_2 \Upsilon_2^2 - K_3 \tilde{p}^\top \tilde{p} < 0, \qquad (z,q) \in (\mathcal{C} \cup \mathcal{D}) \setminus \mathcal{A}_1 \tag{5.15}
$$

Hence, as the Lyapunov function also is strictly decreasing during jumps. $\mathcal{A}_1$ is GAS, and we have defined a global asymptotically stable feedback law for driving an angle $z^\psi \to z^{\psi_d}$. To emulate an underactuated ship, the sway force can be chosen as:

$$
\tau_v = \frac{m_{23}}{m_{33}} \tau_r \tag{5.16}
$$

Next, the parameters γ_1 and K_3 must be set to design the switching rate convergence of p. By choosing $\gamma_1 = 50$ and $K_3 = 50$, we get an approximate convergence of p in 5 seconds, and is considered to be a sufficient smoothing of the switch. Figure 5.1 shows the effect of generating the smooth switch p.

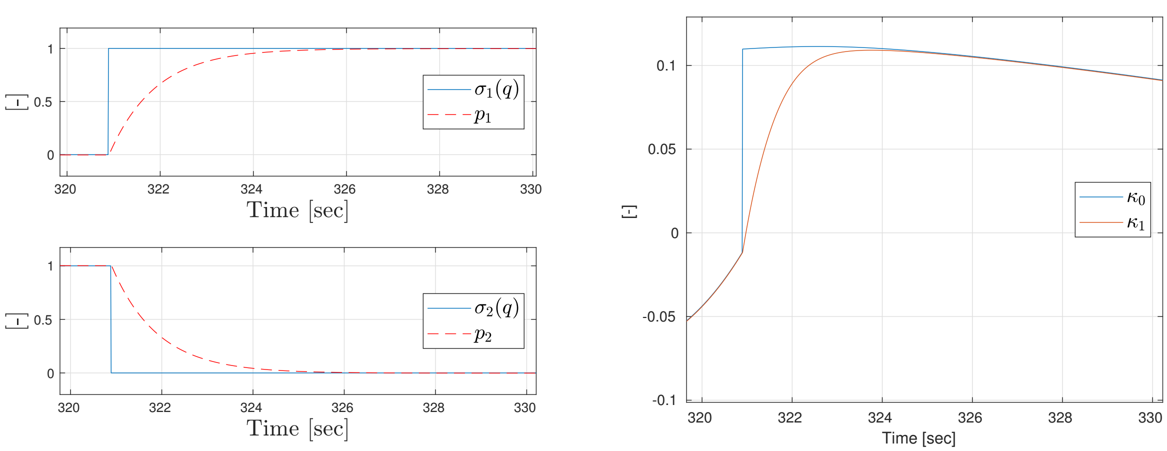

(a) Generation of smooth switch p

(b) Resulting virtual control from smooth switch

Figure 5.1: Effect of smooth switch

We can see from Figure 5.1b that the virtual control κ_1 is smoothed compared to κ_0. The effect of this is that the control τ_r also is smooth, and can more easily be applied to a dynamical system.

Remark 1 Other dynamics for $\dot{r}$ can be considered such as $\dot{r} = \tau_r = N_\delta\delta$(where N_δ is a gain and δ is the rudder angle), or $\dot{r} = -\frac{1}{T}r + \frac{K}{T}\delta$(Nomoto model with rudder as input). The backstepping procedure will be similar, but replacing τ_r with either $N_\delta\delta$ or $-\frac{1}{T}r + \frac{K}{T}\delta$ and solve for δ to get the rudder angle as input. Due to uncertainties of the parameters K and T in the Nomoto model, it was chosen not to proceed with the Nomoto model for the test cases. In stead the vessel is emulated to be underactuated, and the response is assumed to be similar to a CDM based on the Nomoto model.

Remark 2 The procedure for backstepping the non-hybrid control design will be similar. The resulting desired yaw moment is then:

$$\tau_{r,non-hyb} = \dot{r}_d + \nabla_z\kappa_{02}(z)Sz - \nabla_z P_{01}(z)Sz - K_2(\tilde{r} - \kappa_{02}(z)) \tag{5.17}$$

Remark 3 Due to the complexity of the algebraic expressions $\nabla_z\vartheta(z)$ and $\nabla_z\kappa_{02}(z)$, they are not derived in the main part of this thesis, but rather included in Appendix A.2.

5.3 Physical Experiments

As the simulations of this control allocation is quite simple as we only control 1DOF, the simulation results to test the control design is omitted. In stead, experimental results in the MC-lab will be presented. The hybrid heading controller was combined with the DP controller described in Section 2.2 in surge and sway. The chosen bandwidth was $\omega_b = 0.1$, which by applying (2.36) and the diagonal numerical values for $\mathbf{M}$ and $\mathbf{D}_L$ from (A.2) and (A.3) gave the following gains(where the gains in yaw is set to zero because the hybrid heading controller controls the heading):

$$\mathbf{K}_p = \begin{bmatrix} 3.3672 & 0 & 0 \\ 0 & 5.6865 & 0 \\ 0 & 0 & 0 \end{bmatrix}, \quad \mathbf{K}_i = \begin{bmatrix} 0.0526 & 0 & 0 \\ 0 & 0.0889 & 0 \\ 0 & 0 & 0 \end{bmatrix}, \quad \mathbf{K}_d = \begin{bmatrix} 37.75 & 0 & 0 \\ 0 & 62.5875 & 0 \\ 0 & 0 & 0 \end{bmatrix} \tag{5.18a}$$

$$\lambda = 0.99, \qquad K_p = 0.04, \qquad \gamma_1 = 50, \qquad \gamma_2 = 2, \qquad K_2 = 40, \qquad K_3 = 50 \tag{5.18b}$$

As the only goal for this experiment was to check the behaviour of the 1DOF heading controller, it was not attempted to do positional changes, but rather use the DP controller for stationkeeping while controlling the heading to a setpoint. For all experiments, the vessel was controlled to the origin with initial heading $\psi_0 = 0°$. Then three different setpoints of $\psi_d = \{-170°, 180°, 170°\}$ was sent to the heading controller with initial logic modes $q_0 = \{1, 2\}$. Hence, the experiment was divided into six cases. Figure 5.2 shows the results, where the left figures shows the heading, and the right figures shows the logic mode $\sigma(q)$ and smooth switch p.

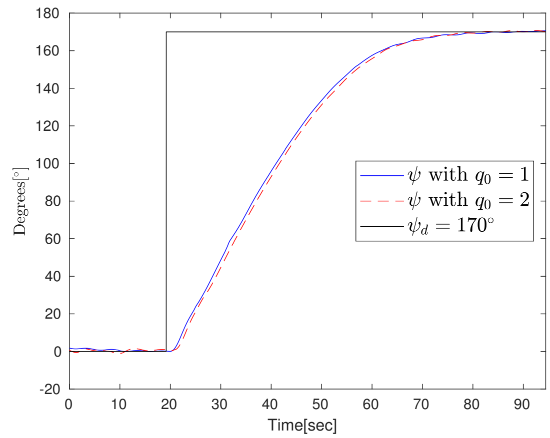

(a) Heading

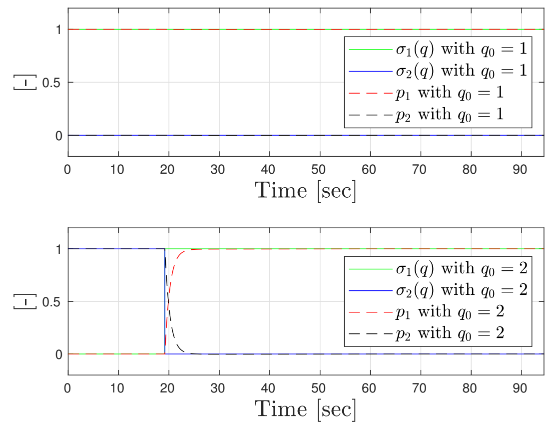

(b) Logic mode

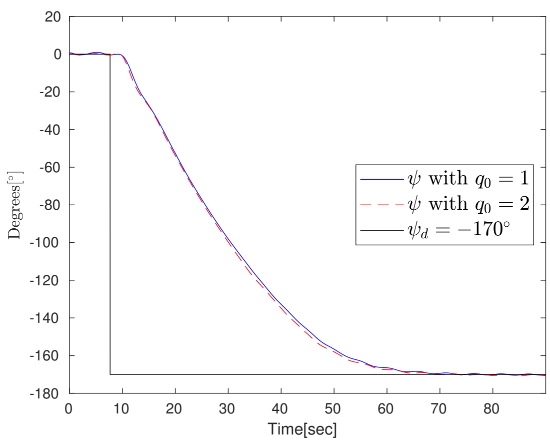

(c) Heading

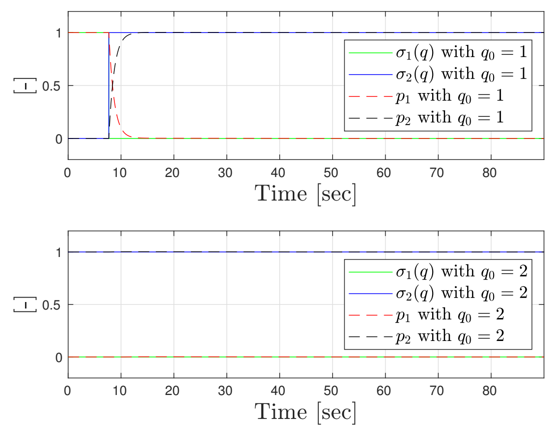

(d) Logic mode

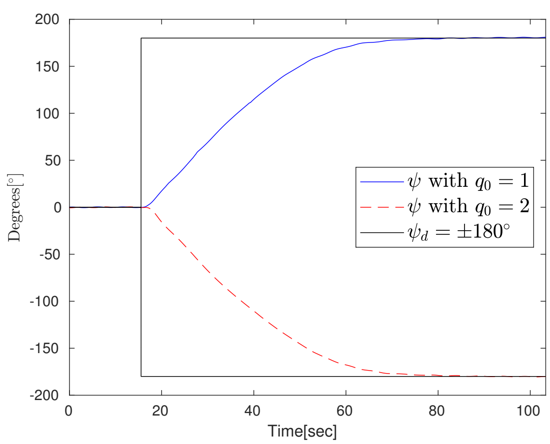

(e) Heading

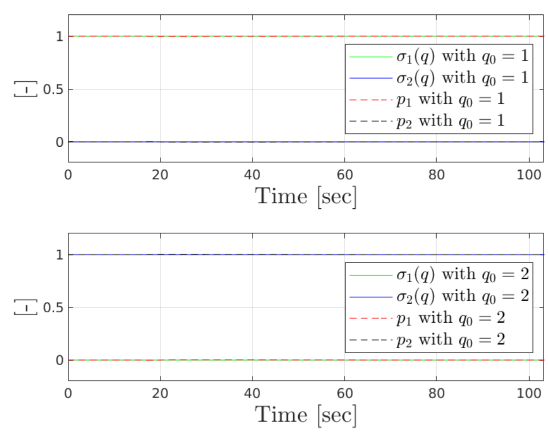

(f) Logic mode

Figure 5.2: Physical DP experiments of CSAD with different heading setpoints

Figures 5.2a and 5.2b shows the response when the setpoint is at $\psi_d = 170°$. It is observed that the logic mode toggles for $q_0 = 2$, but not for $q_0 = 1$. This happens due to the error maps inside the jump set $\mathcal{D}_2$, and the vessel will rotate clockwise. The same effect occurs when $q_0 = 1$ and $\psi_d = -170°$ as shown in Figure 5.2c and 5.2d. In this case, the error maps into the jump set of $\mathcal{D}_1$, and the vessel will rotate counter-clockwise. The last test was to command the vessel to do a 180° turn, which is shown in figure 5.2e. As the error does not lie within neither of the jump sets $\mathcal{D}_1$ or $\mathcal{D}_2$ the logic mode will not switch, as shown in Figure 5.2f. The rotational direction is now determined by the initial value of q. We see that for $q_0 = 1$, the vessel will rotate clockwise, while when $q_0 = 2$, the vessel will rotate counter-clockwise. We therefore have full control of the rotational direction and it will converge to the desired setpoint in a robust and stable manner.

5.3.1 Video of Experiment

The experiments in the MC-lab were recorded and a link to the video can be found in appendix B

5.4 Discussion

The 1DOF hybrid heading controller developed in this chapter gives promising results. As proven, the control allocation guarantees robust convergence to the desired heading with smooth control signals even when the logic mode switches. As experienced in the lab, the turning rate (and control forces) was quite large when the vessel received a setpoint that generated an error close to the ±180° range, but became very low close to the setpoint. This might be due to the lack of reference model, since this design reroutes $\psi_{ref} = \psi_d$. However, as large errors in the ±180° range induced larger values for τ_r than physically achievable for the model vessel when the gain $K_p > 0.04$, it was chosen to keep the gain at this value. If a reference model was to be designed, it could not have the same design as traditional reference models, as these would try to wrap towards the shortest rotation and possibly disrupt the whole purpose of the robust hybrid design. If a reference model was to be implemented, it would have needed to have a similar dynamics as $\dot{z}$ with possibly a synchronization of the logic mode. However this is not implemented, but should be further investigated.

Chapter 6

Velocity Vector Control on $\mathbb{S}^1$

6.1 $\mathbb{S}^1$ Formulation of Angles and Current

We consider planar motions of a marine surface vessel with position $p^n := col(x, y) \in \mathbb{R}^2$ in {n}-frame. The surge and sway velocities in {b}-frame are $\nu = col(u, v) \in \mathbb{R}^2$, and yaw rate $r = \dot{\psi}$. The three other DOF's roll, pitch and heave are disregarded, as these are considered to be self-stabilizing.

The vessels heading expressed on $\mathbb{S}^1$ is $z^\psi \in \mathbb{S}^1$. If the vessel is exposed to an irrotational constant current the global frame, this can be defined as $\nu_c^n = [V_c \cos(\beta_c), V_c \sin(\beta_c)]^\top = V_c z^{\beta_c} \in \mathbb{R}^2$, with z^{β_c} being the $\mathbb{S}^1$ representation of the direction of a current flowing with an angle β_c relative to the north axis. Rotating the {n}-composed current velocity vector to {b} yields $\nu_c^b = R(z^\psi)^\top \nu_c^n$, and the relative velocity $\nu_r \in \{b\}$ becomes:

$$\nu_r = \nu - \nu_c^b = \nu - R(z^\psi)^\top \nu_c^n \tag{6.1}$$

The vessels global and relative speed is defined as $U := |\dot{p}^n| = |\nu|$ and $U_r = |\nu_r|$ respectively. Next, we define the course angle as $z^\chi \in \mathbb{S}^1$, crab angle $z^\beta \in \mathbb{S}^1$ and sideslip angle $z^{\beta_r} \in \mathbb{S}^1$. The sideslip and crab angles occur due the the drag forces of ships, where ocean currents and hydrodynamic forces due to relative velocities make the heading not being equal to the course. The angles are derived from the relationships in (2.39) and (3.16):

$$z^\chi := \frac{\dot{p}}{U}, \qquad z^\beta = \frac{\nu}{U}, \qquad z^{\beta_r} = \frac{\nu_r}{U_r} \tag{6.2}$$

Such that $z^\chi = R(z^\psi) z^\beta \implies \dot{p}^n = U z^\chi = U R(z^\beta) z^\psi = R(z^\psi)\nu$. Furthermore, using (3.15) and (3.17) gives:

$$\dot{z}^\beta = \omega_\beta S z^\beta, \qquad \omega_\beta = \left(z^\beta\right)^\top S^\top \frac{\dot{\nu}}{U} \tag{6.3}$$

$$\dot{z}^\chi = \left(r + \omega_\beta\right) S z^\chi \tag{6.4}$$

Note that, for a zero motion $U = 0$, the crab, sideslip and course angles have no physical meaning, while the heading z^ψ always have a physical meaning.

6.2 Control Objective

With the kinematics

$$\dot{p}^n = R(z^\psi)v = UR(z^\beta)z^\psi = Uz^\chi \tag{6.5}$$

$$\dot{z}^\psi = rS\,z^\psi \tag{6.6}$$

and kinetics

$$\dot{u} = \sigma_1(\boldsymbol{v}) + \frac{1}{m_{11}}\tau_u + \varphi_1(\boldsymbol{v})^\top\theta \tag{6.7a}$$

$$\dot{v}_r = \sigma_2(\boldsymbol{v}_r) \tag{6.7b}$$

$$\dot{r} = \sigma_3(\boldsymbol{v}) + \frac{1}{m_{33}}\tau_r + \varphi_3(\boldsymbol{v})^\top\theta \tag{6.7c}$$

and the control objective to track some velocity vector $\dot{p}^n_d(t) = U_d(t)z^{\chi_d}(t) \in \mathbb{R}^2$, the velocity tracking problem is to design a control law for (τ_u, τ_r) such that:

$$\lim_{t\to\infty}[\dot{p}^n(t) - \dot{p}^n_d(t)] = 0 \tag{6.8}$$

Note that if $v^n_c \neq U_d z^{\chi_d}$, then there are exactly two solutions for $z^\beta \in \mathbb{S}^1$ that gives a feasible velocity tracking. The ship could either choose to head against the direction of travel if $U_d >> V_c$, or against the current if $V_c > U_d$ and "slide backwards" with the current while tracking the desired velocity vector. Hence, the crab angle may converge to the two solutions corresponding to $z^\beta_x \in [0,1]$ or $z^\beta_x \in [-1,0]$, depending on the operation. For simplicity, we constrain the surge velocity to be positive according to (6.9):

$$u_d(t)^2 = \max\left\{|\dot{p}_d(t)|^2 - v(t)^2, \varepsilon^2\right\}, \tag{6.9}$$

where $\varepsilon > 0$ is a small number corresponding the the minimum surge speed. Then, z^β_x will converge to the interval $[0,1]$. As it is the course and not the heading itself we want to control, we redefine z and $\dot{z}$ to be the course error and derivative of the course error:

$$z = R(z^{\chi_d})^\top z^\chi = R(z^{\chi_d})^\top R(z^\psi)z^\beta \tag{6.10a}$$

$$\dot{z} = R(z^{\chi_d})^\top[R(z^\psi)\dot{z}^\beta + rR(z^\beta)S\,z^\psi] \tag{6.10b}$$

$$= R(z^{\chi_d})^\top R(z^\psi)[\dot{z}^\beta + rS\,z^\beta] \tag{6.10c}$$

where the goal is to achieve $z \to \mathbf{e}_1$. For a time varying desired velocity vector, we have:

$$\dot{z}^{\chi_d} = \omega_{\dot{p}_d}S\,z^{\chi_d}, \qquad \omega_{\dot{p}_d} = (z^{\chi_d})^\top\,S^\top\frac{\ddot{p}_d}{U_d}. \tag{6.11}$$

and error dynamics:

$$\dot{z} = \left(r + \omega_\beta - \omega_{\dot{p}_d}\right) S z \tag{6.12}$$

Hence, inserting $r_d = -\omega_\beta + \omega_{\dot{p}_d}$ and $\dot{r}_d = -\dot{\omega}_\beta + \dot{\omega}_{\dot{p}_d}$ in (5.14) will ensure $z^\chi \to z^{\chi_d}$.

Assuming a constant velocity tracking signal $\dot{p}_d$, we have $\ddot{p}_d = 0$ such that $\omega_{\dot{p}_d} = 0$. Then the closed loop system (assuming $u(t) = u_d(t)$) becomes:

$$\dot{z} = \kappa_1(\zeta, q) S z \tag{6.13}$$

$$\dot{v}_r = \sigma_2(\upsilon_r), \tag{6.14}$$

$$v = v_r + R(z^\psi)^\top v_c^n \tag{6.15}$$

$$u = \sqrt{\max\left\{U_d^2 - v^2, \varepsilon^2\right\}} \tag{6.16}$$

It follows that at $z = \mathbf{e}_1$ and $v_r = 0$ we get

$$r = 0, \tag{6.17}$$

$$\dot{z} = 0 \tag{6.18}$$

$$\dot{v}_r = 0, \tag{6.19}$$

$$\dot{v} = \dot{v}_r - rR(z^\psi)^\top v_c^n z = 0 \tag{6.20}$$

$$\dot{u} = 0 \tag{6.21}$$

$$\omega_\beta = \left(z^\beta\right)^\top S^\top \frac{\dot{v}}{U} = 0, \tag{6.22}$$

$$v = R(z^\psi)^\top v_c^n \tag{6.23}$$

$$U^2 = u^2 + v^2 = \begin{cases} U_d^2 & v^2 < U_d^2 - \varepsilon^2 \\ \varepsilon^2 + v^2 & v^2 > U_d^2 - \varepsilon^2 \end{cases} \tag{6.24}$$

6.3 Control Design

The resulting Control Design for velocity vector control for an underactuated vessel is done according to (2.55), (5.14), (5.16) and (5.17), where the control in yaw can either be hybrid or non-hybrid. These are restated in (6.25):

$$\tau_{u,d} = m_{11}\left(-\boldsymbol{\varphi}^\top \hat{\boldsymbol{\theta}} - \sigma_1(\boldsymbol{\upsilon}) - K_{pu} e_u + \dot{u}_d\right), \qquad K_{pu} > 0 \tag{6.25a}$$

$$\tau_{v,d} = \frac{m_{23}}{m_{33}} \tau_{r,d} \tag{6.25b}$$

$$\tau_{r,d} = -\dot{\omega}_\beta + \dot{\omega}_{\dot{p}_d} + \nabla_z \vartheta(z) S z \tilde{r} p + \vartheta(z) v(z, p, q) - \frac{1}{\gamma_2} \nabla_z V_0(z, q) S z - \frac{1}{\gamma_2} K_2 \Upsilon_2, \qquad K_2 > 0 \tag{6.25c}$$

$$\tau_{r,d,non-hyb} = -\dot{\omega}_\beta + \dot{\omega}_{\dot{p}_d} + \nabla_z \kappa_{02}(z) S z - \nabla_z P_{01}(z) S z - K_2(\tilde{r} - \kappa_{02}(z)) \tag{6.25d}$$

with

$$\tilde{r} = r + \omega_\beta - \omega_{\dot{p}_d} \tag{6.26}$$

As the desired thrust might be larger than achievable for the vessel it is applied on, it was chosen to take these constraints into consideration. According to the CSAD User Manual (NTNU, 2017), the maximum achievable thrust in surge sway and yaw is approximately $\tau_{u,max} = 9[N], \tau_{v,max} = 9[N], \tau_{r,max} = 6[Nm]$. It was therefore chosen to constrain the forces to be lower than these in order to obtain a set of control forces which is possible. As these maximums can not be achieved simultaneously, the commanded saturated forces is set to be lower, according to:

$$\tau_{u,c} = sat(\tau_{u,d}, 3), \qquad \tau_{v,c} = sat(\tau_{v,d}, 3), \qquad \tau_{r,c} = sat(\tau_{r,d}, 2) \tag{6.27}$$

These forces are applied to the model shown in Figure 4.1 with the relative velocities calculated according to (2.21), both with and without the effect of current, where the body fixed velocities are found according to (6.1). The numerical values for the vessel parameters is found in Appendix A.1. The various gains for the controllers and estimators are chosen as in Table 6.1.

Table 6.1: Test parameters for velocity vector control

Parameter	Value
K_p	0.04
λ	0.99
L	$1/(\arccos(-\lambda) - \arccos(\lambda)) \approx 0.3498$
k_1	$0.495\sqrt{1-\lambda^2}/(\lambda L) \approx 0.20162$
k_2	$-k_1$
K_{pu}	0.7
Γ_u	$0.1\boldsymbol{I}^{4x4}$
γ_1	50
γ_2	2
K_2	40
K_3	50
q_0	1 or 2
ε	0.01

6.4 Simulations

This section will present a number of various cases where a desired velocity vector is to be achieved. Simulations of the non-hybrid and hybrid designs are tested, both with and without current. The desired course χ_d and speed over ground U_d will be included within the figure as a constant or function of time. This also applies to the current velocity V_c and angle β_c whenever there is current present. For the hybrid case, the initial and final value of q, i.e $q_0, q_f \in \{1, 2\}$ are also included. It is assumed full knowledge of all positions (x, y), velocities $(u, v, r, \dot{x}, \dot{y})$ and angles (χ, ψ, β) either obtained directly from the output of the Simulink model in Figure 4.1, or deduced from these. In addition, we consider the desired thrust to be achieved, so there is no thrust allocation or thruster dynamics used. For all cases, the initial angle is $\psi_0 = 0°$, and velocities $u_{r,0} = v_{r,0} = r_0 = 0$. Without current, we also have $u_0 = v_0 = 0$, and with current $[u_0, v_0]^\top = R(z^{\psi_0})^\top v_c^n$.

6.4.1 Without current

First, the non-hybrid and hybrid control are tested without current. The desired course and speed is set to $\chi_d = 90°$ and $U_d = 0.1[m/s]$. The results for the non-hybrid control is shown in Figure 6.1, and hybrid control in Figure 6.2. For the path plots in Figure 6.1a and 6.2a, the vessel with its position and orientation for each 10'th second is shown.

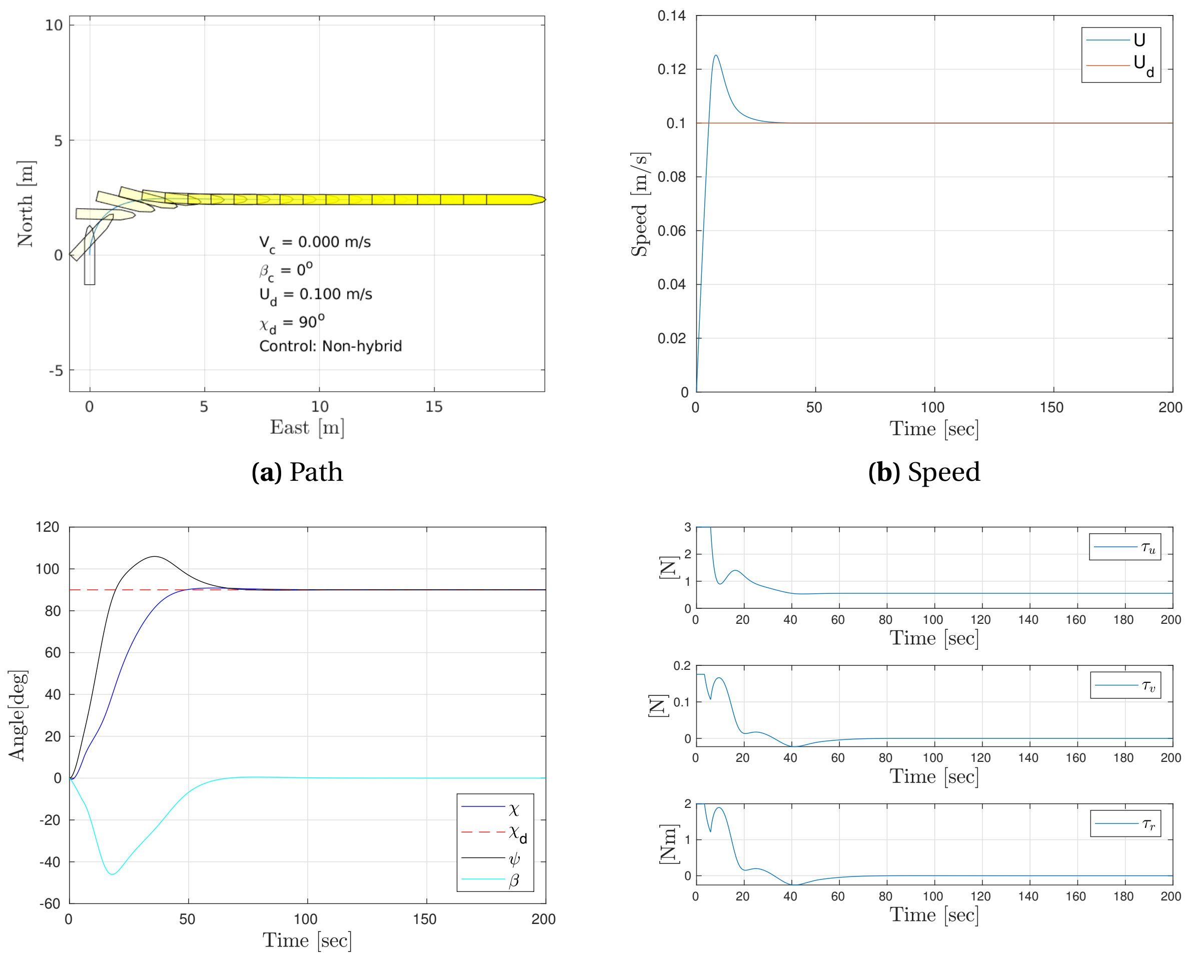

(a) Path

(b) Speed

(c) Angles

(d) Control forces

Figure 6.1: Non-hybrid velocity vector control simulation with $\chi_d = 90°$, $U_d = 0.1[m/s]$

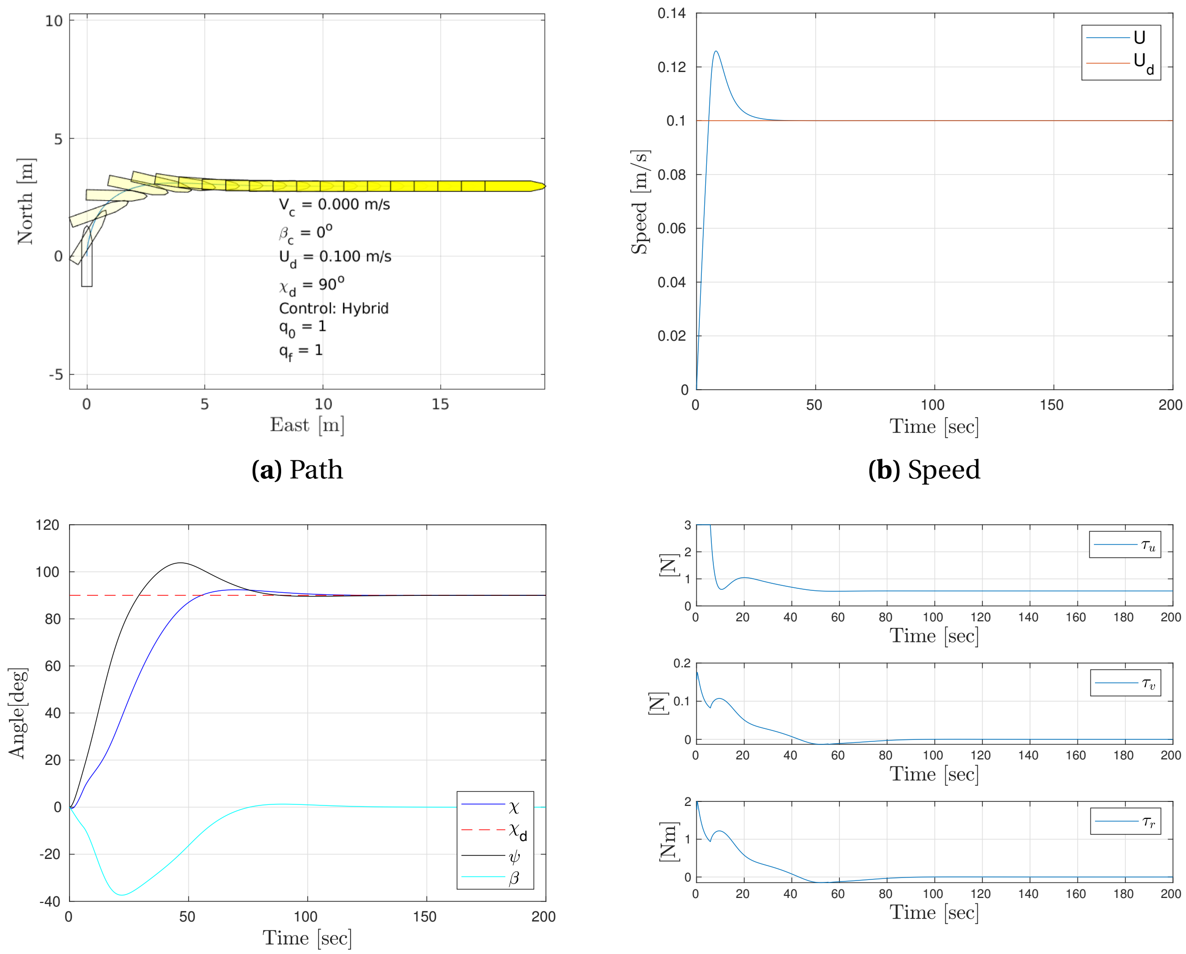

(a) Path **(b)** Speed

(c) Angles **(d)** Control forces

Figure 6.2: Hybrid velocity vector control simulation with $\chi_d = 90°$, $U_d = 0.1[m/s]$

As expected, both the non-hybrid and hybrid control ensures the course and speed to converge to their desired values, as the commanded course is not close to generate an error near $\pm 180°$. The crab angle β also converges to zero as there is no current present, and the course and heading will be equal once the desired course is reached. We notice that the control forces in 6.1d and 6.2d are saturated at their maximum values at the start according to (6.27). This is natural, as there is no reference model to generate a smooth desired speed, and the controller will react to a step from 0 to $U_d = 0.1$. In the following figures, the speed, angles and control forces are not presented, as the path plots as in Figure 6.1a and 6.2a illustrates the overall behaviour.

Next, we test the controllers for a desired course as $\chi_d = \pm 170°$ and initial logic mode $q_0 = \{1, 2\}$ similar to the DP experiments in Section 5.3. The results are shown in Figure 6.3.

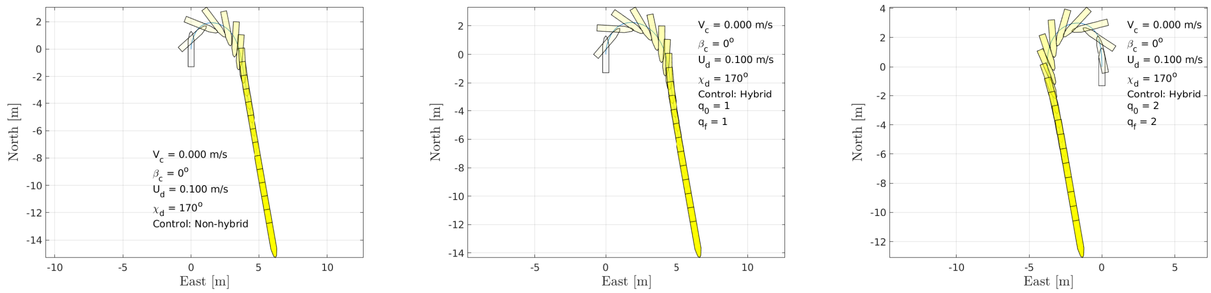

(a) Non-hybrid control **(b)** Hybrid control $q_0 = 1$ **(c)** Hybrid control $q_0 = 2$

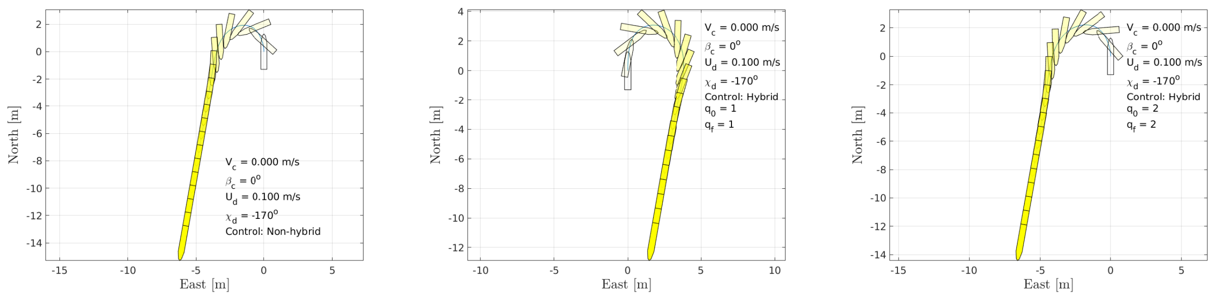

(d) Non-hybrid control **(e)** Hybrid control $q_0 = 1$ **(f)** Hybrid control $q_0 = 2$

Figure 6.3: Velocity vector control simulation with $\chi_d = \pm 170°$, $U_d = 0.1[m/s]$, $q_0 = \{1, 2\}$

Here, we observe the effect of the initial value of q. As the non-hybrid control in Figure 6.3a and 6.3d will rotate according to the shortest rotation, the hybrid controller can choose to rotate in the other direction depending on the value of q_0 as shown in Figure 6.3c and 6.3e. However, when the course error is at $\pm 180°$, the hybrid controller has a much more robust behaviour and will ensure a more desirable response, as shown in Figure 6.4.

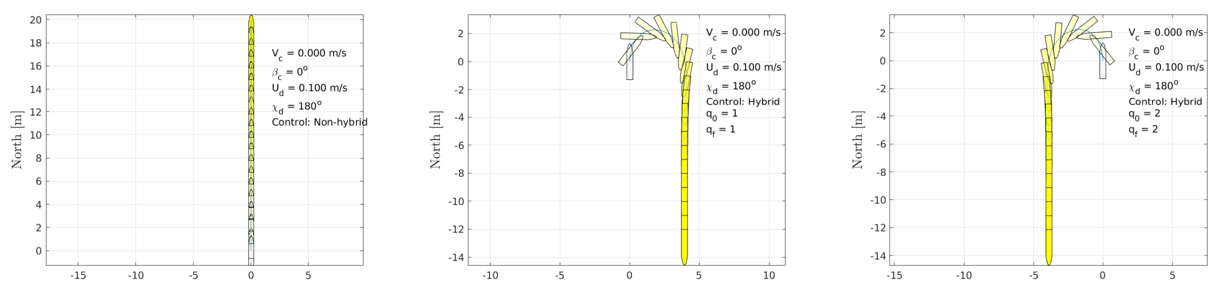

(a) Non-hybrid control **(b)** Hybrid control $q_0 = 1$ **(c)** Hybrid control $q_0 = 2$

Figure 6.4: Velocity vector control simulation with $\chi_d = 180°$, $U_d = 0.1[m/s]$, $q_0 = \{1, 2\}$

Here we can see that the non-hybrid controller fails to induce a control force in yaw to reach the control objective. The hybrid controller however is able to do the desired 180° turn, either clockwise or counter-clockwise according to q_0. It is therefore both stable and robust.

To test the hybrid controller for time varying desired course signals, we consider a linearly increasing (initiated after 100 seconds) $\chi_d(t) = 0.5°t$ to generate a circular path, and a sinusoidal $\chi_d(t) = 90° \sin\left(\frac{2\pi t}{200}\right)$ to generate a path that varies harmonically between +90° and −90° with a period of 200[s]. The results are shown in Figure 6.5.

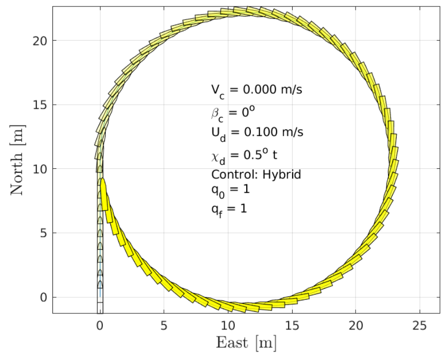

(a) Path for linearly increasing χ_d

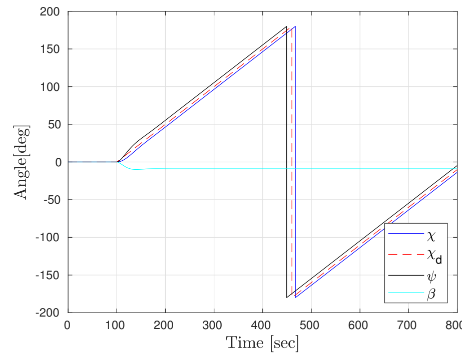

(b) Angles

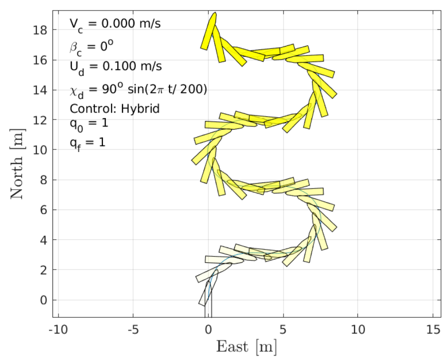

(c) Path for harmonically varying χ_d

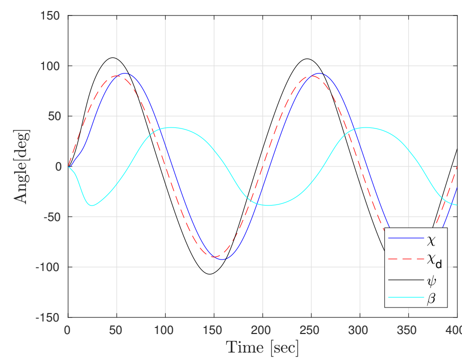

(d) Angles

Figure 6.5: Velocity vector control simulation for time varying χ_d, $U_d = 0.1[m/s]$, $q_0 = 1$

We see that the achieved velocity vector follows the reference nicely, only with a small time delay. Next the control allocation will be tested when there is ocean currents present, and from now on the only control design considered is the hybrid controller.

6.4.2 With current

It is chosen to still test the control design for a desired speed $U_d = 0.1[m/s]$. The ocean current is set to have a speed $V_c = 0.03[m/s]$ and direction $\beta_c = -135°$. Figure 6.6 shows the response with a desired course $\chi_d = 90°$ and logic mode $q_0 = 1$:

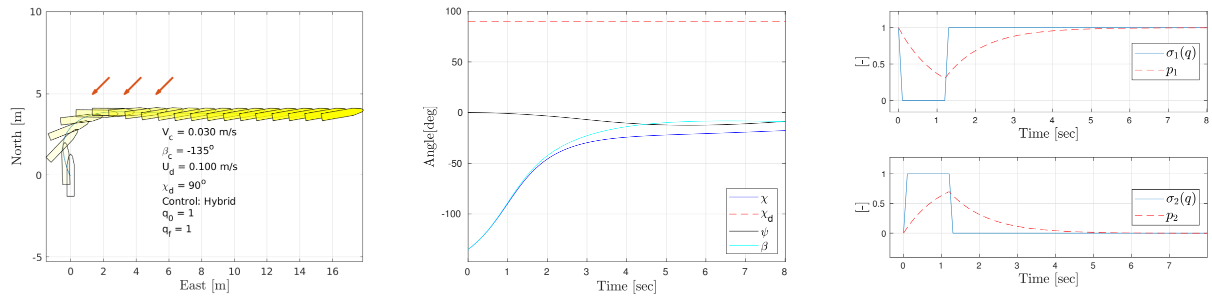

(a) Path **(b)** Angles first 8 seconds **(c)** Logic mode first 8 seconds

Figure 6.6: Velocity vector control simulation with $\chi_d = 90°$, $U_d = 0.1[m/s]$, $q_0 = 1$, $V_c = 0.03[m/s]$, $\beta_c = -135°$

As there now are ocean currents present, the initial course will be equal to the current direction $\beta_c = -135°$, as seen in Figure 6.6b. What this does is to trigger q to switch from 1 to 2, as the course angle error ends up inside the jump set $\mathcal{D}_1$. However, when the surge velocity controller ensures a positive surge velocity, it will switch back to $q = 1$, as shown in Figure 6.6c. Despite the toggling of the logic mode, this will not affect the overall behavior, and we still achieve the desired course. Note that with ocean currents, the crab angle will converge to a nonzero value, as seen in Figure 6.6a. In addition, as the logic mode when $q_0 = 1$ toggles immediately upon initialization, it will in practice result in a very similar response if the initial logic mode was $q_0 = 2$.

Next, the response for other desired course angles are tested. Figure 6.7 shows the response for $\chi_d = \{145°, 150°\}$.

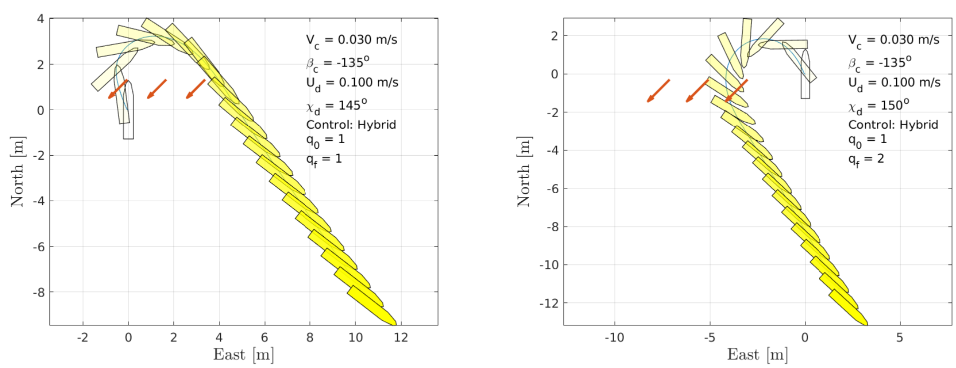

(a) Path $\chi_d = 145°$ **(b)** Path $\chi_d = 150°$

Figure 6.7: Velocity vector control simulation with $\chi_d = \{145°, 150°\}$, $U_d = 0.1[m/s]$, $q_0 = 1$, $V_c = 0.03[m/s]$, $\beta_c = -135°$

This shows that for a desired course of $\chi_d = 145°$, the same toggle as in Figure 6.6c will occur, and the hybrid controller will choose to rotate clockwise. On the other hand, for $\chi_d = 150°$ the logic mode stays at $q = 2$ after the initial toggle, and will rotate counter-clockwise to achieve the desired course. Next, we test the VVC on the time varying desired courses with the same current speed and angle. The results are shown in Figure 6.8.

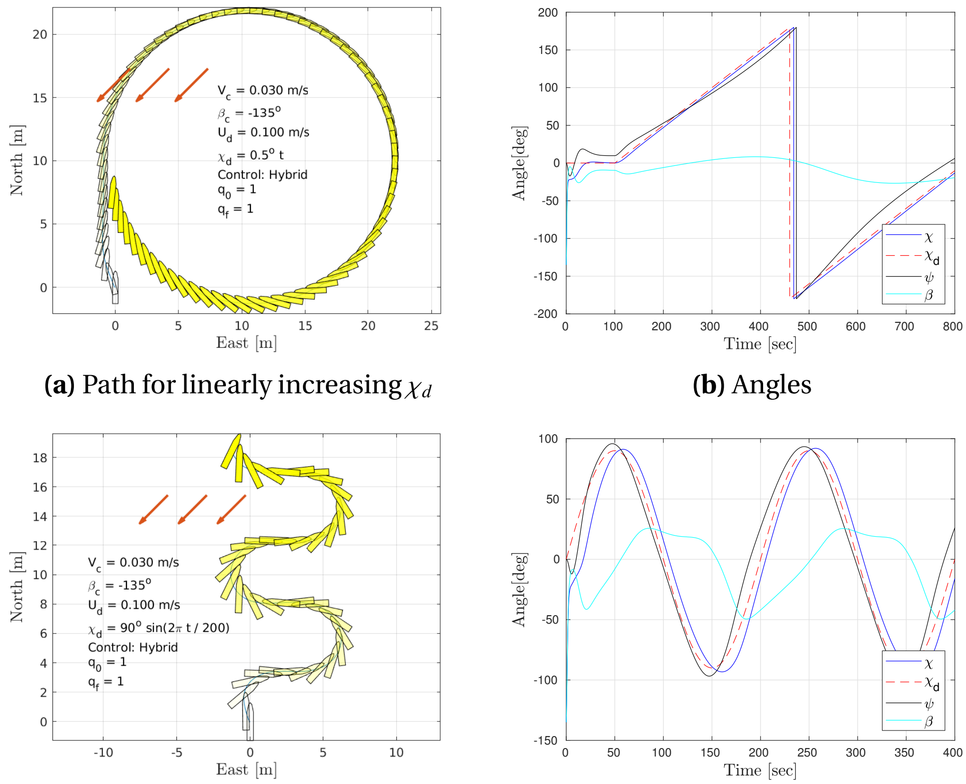

(a) Path for linearly increasing χ_d

(b) Angles

(c) Path for harmonically varying χ_d

(d) Angles

Figure 6.8: Velocity vector control simulation for time varying χ_d, $U_d = 0.1[m/s]$, $q_0 = 1$, $V_c = 0.03[m/s]$, $\beta_c = -135°$

We see that the vessels behaviour is similar, but struggles a bit more to obtain the desired course. However, it still manages to obtain a response similar to the one showed in Figure 6.5. The current is amplified to $V_c = 0.09[m/s]$ to investigate if it is able to withstand increasing environmental disturbances. These results are shown in Figure 6.9.

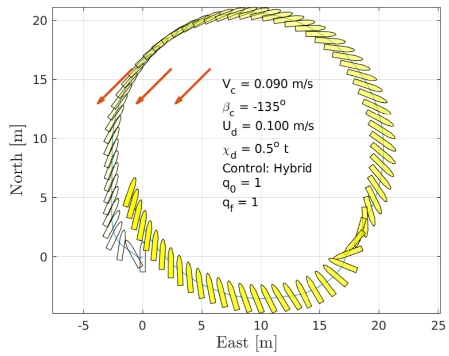

(a) Path for linearly increasing χ_d

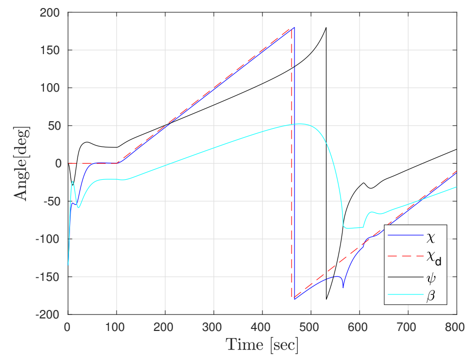

(b) Angles

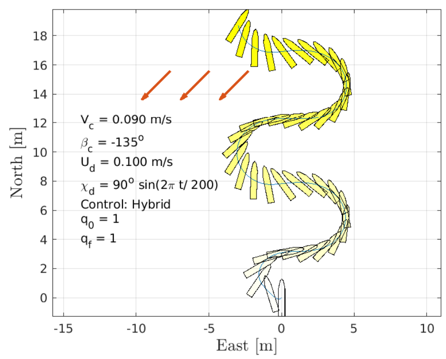

(c) Path for harmonically varying χ_d

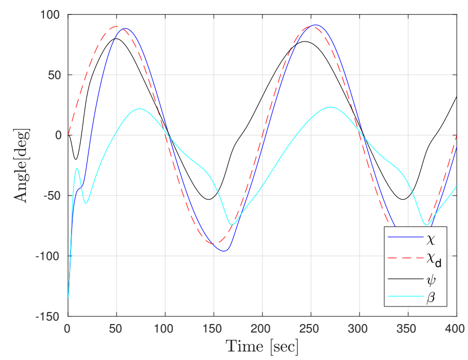

(d) Angles

Figure 6.9: Velocity vector control simulation for time varying χ_d, $U_d = 0.1[m/s]$, $q_0 = 1$, $V_c = 0.09[m/s]$, $\beta_c = -135°$

It is observed that the controllers struggles a bit more to achieve the desired velocity vector. An interesting behaviour occurs in Figure 6.9a, where the heading drastically changes once the ocean current is aligned with the direction of travel. This can be seen in Figure 6.9b as a "drop" in the course angle at approximately 580[s]. However, once the vessel has performed the turn, it quickly converges to again reach the desired course. Note that, as opposed to path following, the vessel does not compensate for the sudden increase of course error and does not try to reach the circle path it had initially in Figure 6.5a. For the harmonically varying course command, a similar occurrence happens at about 160[s]. Here the vessels heading is about $\psi = -45°$, which means that the ocean current is pushing the vessel directly from the starboard side. Therefore, due to the underactuation in sway, the vessel needs to first orient itself more against the current to be able to turn.

6.5 Discussion

In this part, the VVC problem with HHC seems to give promising results, both with and without current. The direction of turn when the course error in within the range $\{-180, -170\} \cup \{170, 180\}$ is similar to what was presented in section 3.3. In addition, the adaptive surge speed controller ensures the desired velocity is achieved, and converges nicely to its desired value. The lack of reference model in surge is also present here, and could also be implemented to obtain a more smooth convergence towards the desired speed. On the time changing course maneuvers, it is observed that the course is a bit behind its reference. Again, this suggest for a larger value of K_p or to add an integral state in the design for a better tracking performance. However, the overall result shows that it is able to converge to the desired course, both with and without the influence of current.

Chapter 7

Path-following Control on $\mathbb{S}^1$

In this section, the VVC problem is extended to Path-Following Control.

7.1 Control Objective

If the vessel is to follow a path with an either constant or varying speed along the path, the control objective is now to satisfy a *geometric* task and a *dynamic* task (Skjetne, 2005):

1. **Geometric Task**: For any continuous function $s(t)$, force the output y, to converge to the designated path $y_d(s)$, that is
$$\lim_{t\to\infty} |y(t) - y_d(s(t))| = 0$$
2. **Dynamic Task**: Satisfy one or more of the assignments:
   - *Time Assignment:* Force s to converge to a desired time assignment $\tau(t)$
$$\lim_{t\to\infty} |s(t) - \tau(t)| = 0 \tag{7.1}$$
   - *Speed Assignment:* Force $\dot{s}$ to converge to a desired speed assignment $v(s,t)$,
$$\lim_{t\to\infty} |\dot{s}(t) - v(s(t),t)| = 0 \tag{7.2}$$
   - *Acceleration Assignment:* Force $\ddot{s}$ to converge to a desired acceleration assignment $\alpha(\dot{s}(t), s(t), t)$,
$$\lim_{t\to\infty} |\ddot{s}(t) - \alpha(\dot{s}(t), s(t), t)| = 0 \tag{7.3}$$

The objective is for the ship to enter and stay on a path $\mathcal{P}$. These paths can either be piecewise linear (C^0), curved with continuous derivatives at intersections of sub-paths (C^1) or paths with higher order of differentiability (C^T). The needed differentiability is dependent on the application.

7.2 Path Generation

A path could either be a discrete, continuous or hybrid parameterization. Skjetne (2005) presents the general case for generating a C^T path for a set of n waypoints(WP) in $\mathbb{R}^2$ as:

$$\begin{aligned}
&\text{Overall desired curve:} && p_d(s) = \mathrm{col}(x_d(s), y_d(s)), && s \in [0, n] && (7.4a)\\
&\text{Subpaths:} && p_{d,i}(s) = \mathrm{col}(x_{d,i}(s), y_{d,i}(s)), && i \in \mathcal{I} = \{1, 2, ..., n\} && (7.4b)\\
&\text{Way-points:} && p_i = \mathrm{col}(x_i, y_i), && i \in \mathcal{I} \cup \{n+1\} && (7.4c)
\end{aligned}$$

To ensure that at all intersections between sub-paths, the derivatives up to the k'th derivative must be equal. This is equivalent to solving a linear set of $(k+1) \cdot 2n$ unknown coefficients to generate the path:

$$x_{d,i}(s) = a_{k,i}s^k + ... + a_{1,i}s + a_{0,i} \tag{7.5a}$$

$$y_{d,i}(s) = b_{k,i}s^k + ... + b_{1,i}s + b_{0,i} \tag{7.5b}$$

Where we sort the equations as a linear system

$$A\phi = b, \qquad \phi^\top = \left[a^\top, b^\top\right] \tag{7.6}$$

and solve for ϕ. You could also scale the slopes/curvatures at the intermediate WPs by a factor λ by setting the first derivatives as $x^s_{d,i} = \lambda(x_{i+1} - x_{i-1})$ and $y^s_{d,i} = \lambda(y_{i+1} - y_{i-1})$ at each WP. Figure 7.1 shows four different generated paths from the WPs:

$$\mathrm{WP} = \begin{bmatrix} 20 & 10 & 20 & 30 & 40 & 70 & 80 & 70 \\ 20 & 30 & 40 & 45 & 15 & 20 & 30 & 40 \end{bmatrix} \tag{7.7}$$

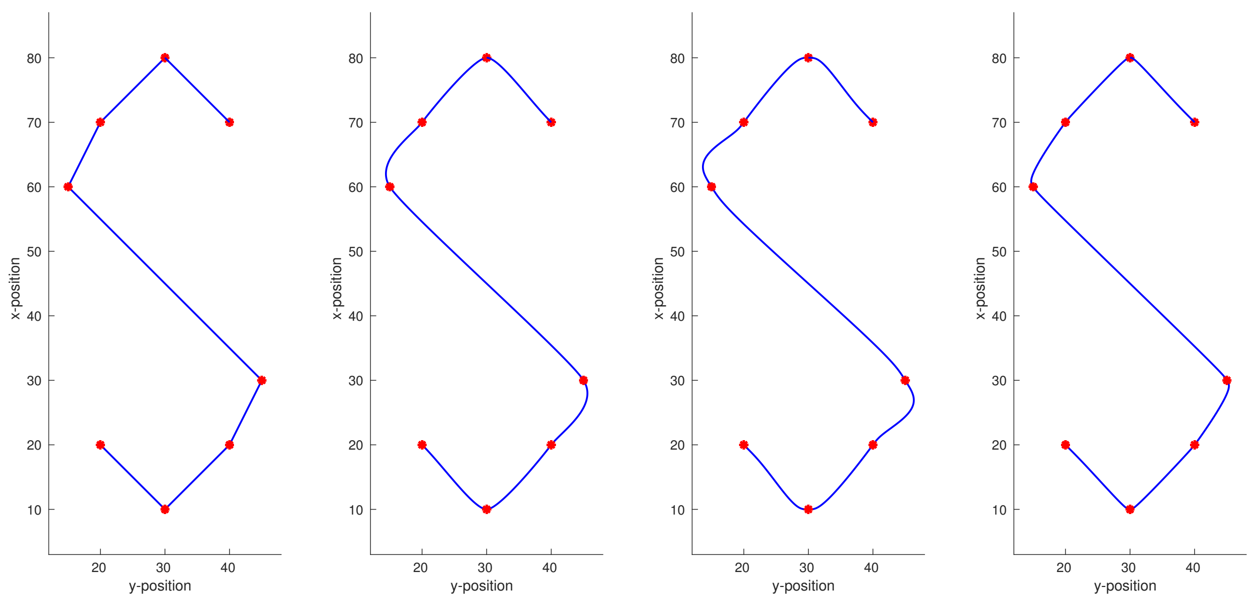

(a) C^0 path **(b)** C^1 path with $\lambda = 0.3$ **(c)** C^3 path with $\lambda = 0.3$ **(d)** C^3 path with $\lambda = 0.1$

Figure 7.1: Different path generations from a set of WPs

Here we can see the effect of the order of differentiability. The C^0 is simply sets of straight line sub-paths, while the C^1 path has continuous derivatives at the intersection of sub-paths, and hence generates a more smooth path. A typical differentiability for vessel tracking is to choose a C^3 path, which will be applied in Section 7.5.

7.3 Path-Following on Straight Line Paths

The path following guidance for surface vessels as described in Section 2.3.4 will now be implemented with angles represented on $\mathbb{S}^1$ and tested together with the underactuated VVC. For simplicity, we consider path-following on the straight-line path

$$\mathcal{P} = \left\{ p \in \mathbb{R}^2 : \exists s \in \mathbb{R} s.t. p = (1-s)p_k + sp_{k+1} \right\} \tag{7.8}$$

defined by N WPs $(p_1, p_2, ..., p_N)$. To achieve this, the vessels' course needs to be aligned with the angle of the current path segment, where α_k in (2.61) is reformulated on $\mathbb{S}^1$ as:

$$z^{\chi_k} := \frac{p_{k+1} - p_k}{|p_{k+1} - p_k|} \tag{7.9}$$

Defining a path reference frame centered at p_k with its x-axis towards p_{k+1}, we can define the *along-track* distance $e_{k,x}(p^n)$ and *cross-track error* $e_{k,y}(p^n)$ for a vessel in position p^n as:

$$e_k(p^n) = col(e_{k,x}(p^n), e_{k,y}(p^n)) = R(z^{\chi_k})^\top (p^n - p_k) \tag{7.10}$$

Hence, the path-following problem for an underactuated vessel is to design control laws for (τ_u, τ_r) to ensure that:

$$\lim_{t\to\infty} e_{k,y}(p^n(t)) = 0 \quad \text{and} \quad \lim_{t\to\infty} \left[U(t) - U_p \right] = 0 \tag{7.11}$$

For a desired speed U_p along the path. As the adaptive surge speed controller combined with the hybrid heading controller is compensating for ocean currents, the only thing needed to solve this problem is to find a suitable combination of (U_d, z^{χ_d}) to track a path.

7.4 Line of Sight Guidance - Straight Line Paths

The LOS guidance scheme in Section 2.3.4 is modified to fit the $\mathbb{S}^1$ representation of angles. For the LBS design, we have:

$$z^{\chi_r} = \left[\cos\left(\frac{-e_{k,y}(t)}{\Delta_{LBS}(t)} \right), \sin\left(\frac{-e_{k,y}(t)}{\Delta_{LBS}(t)} \right) \right]^\top \tag{7.12a}$$

$$z^{\chi_d}_{LBS} = R(z^{\chi_k}) z^{\chi_r} \tag{7.12b}$$

And for EBS:

$$z^{\chi_d}_{EBS} = \left[\cos\left(\frac{y_{los} - y}{x_{los} - x} \right), \sin\left(\frac{y_{los} - y}{x_{los} - x} \right) \right]^\top \tag{7.13}$$

Where the switching of WP's is done according to the circle of acceptance:

$$[x_{k+1} - x(t)]^2 + [y_{k+1} - y(t)]^2 \leq R_{k+1}^2 \tag{7.14}$$

The EBS and LBS is tested in to follow the same eight WP's as in (7.7)(corresponding to the C^0 path in Figure 7.1a) and with an radius of acceptance for each WP of $R_k = 2L_{pp}$, where L_{pp} is the length of CSAD. This . The starting position and velocities of the vessel as well as the controller parameters are the same as in Section 6. The desired velocity along the path is chosen to be $U_d = 0.1[m/s]$. The LBS and EBS parameters are chosen as:

$$R_{EBS} = 2L_{pp}, \qquad R_{LBS} = 2L_{pp} \tag{7.15}$$

The following sections will present the results from simulations with and without ocean currents.

7.4.1 Simulations - Without Current

Initially, the path following for LBS and EBS was tested without currents. Figure 7.2a and 7.2b shows the achieved path, while 7.2c and 7.2d shows the cross-track error. For simplicity, $\Delta_{LBS}(t) = 2L_{pp}$ was chosen to be constant to obtain a more stable response.

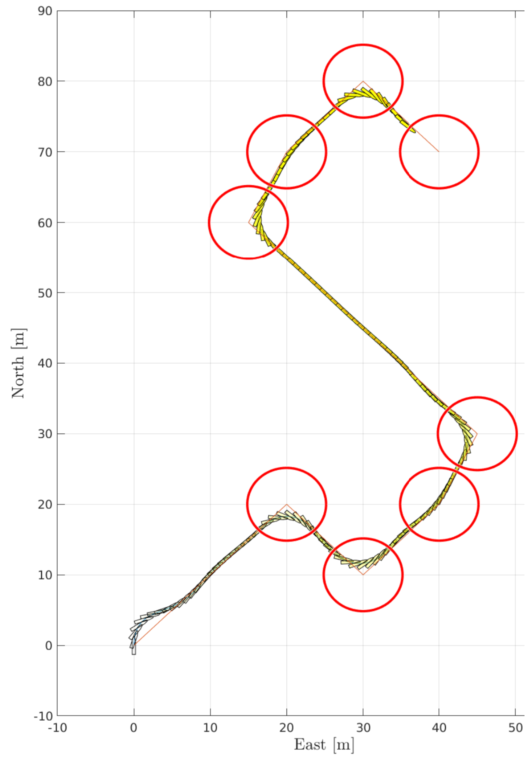

(a) Path - EBS

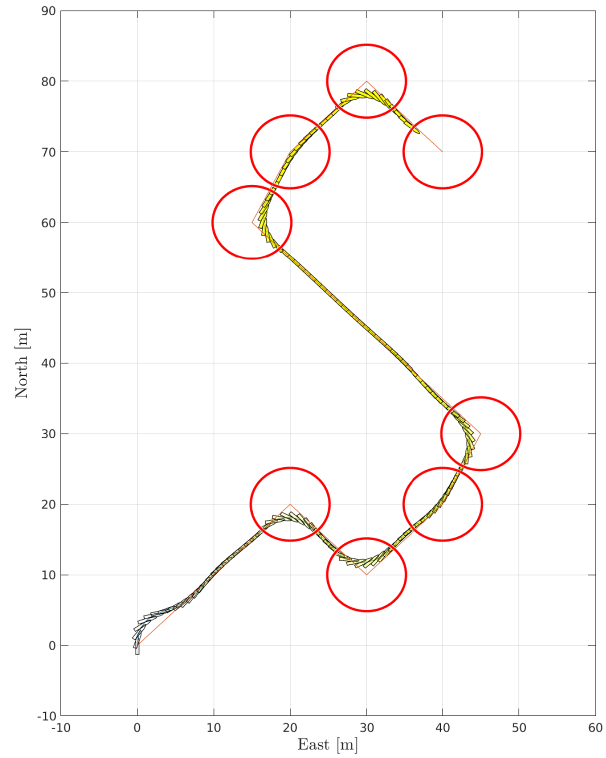

(b) Path - LBS

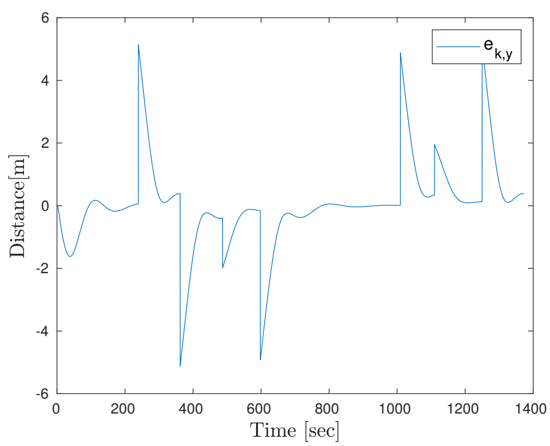

(c) Cross track error - EBS

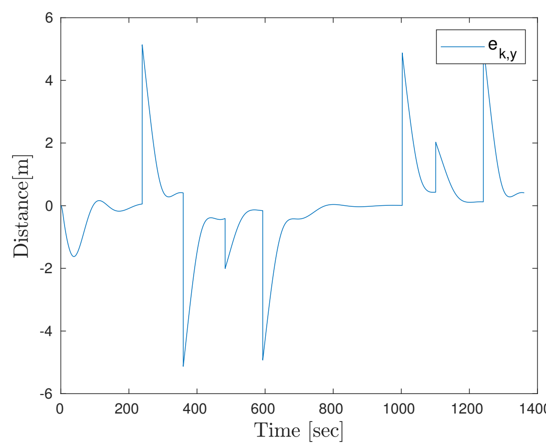

(d) Cross track error - LBS

Figure 7.2: Path plot of LOS Guidance with EBS & LBS for straight line paths - without current

It is observed that both tracking schemes achieves approximately the same result. This is natural, as $R_{LBS} = R_{EBS}$ and the LOS-vectors points approximately in the same directions. The Cross-Track-Error plots shows that both goes to zero in a stable manner, and thus makes sure the vessels position converges to a point along the path. Next, the LOS guidance with EBS and LBS is tested with currents.

7.4.2 Simulations - With Current

In these simulations, we set a relatively large ocean current(relative to the desired velocity $U_d = 0.1[m/s]$) to be $V_c = 0.09[m/s]$ with a direction of $\beta_c = -135°$ to put the LOS guidance and controllers to the test. The performance is shown in Figure 7.3

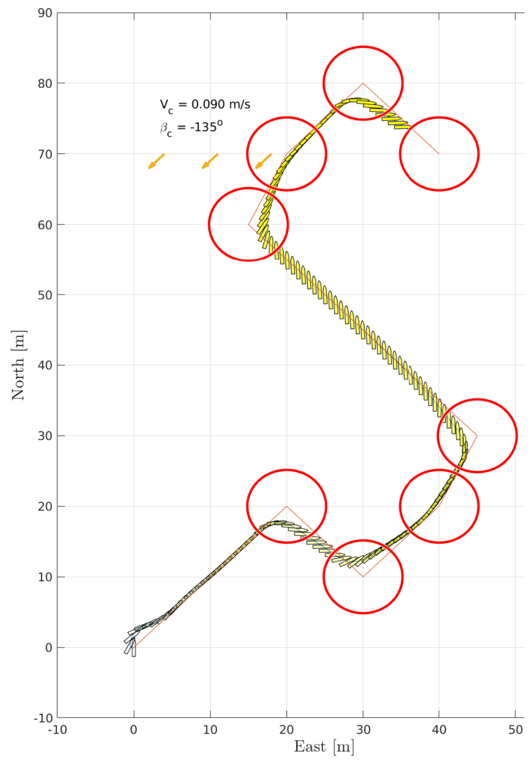

(a) Path - EBS

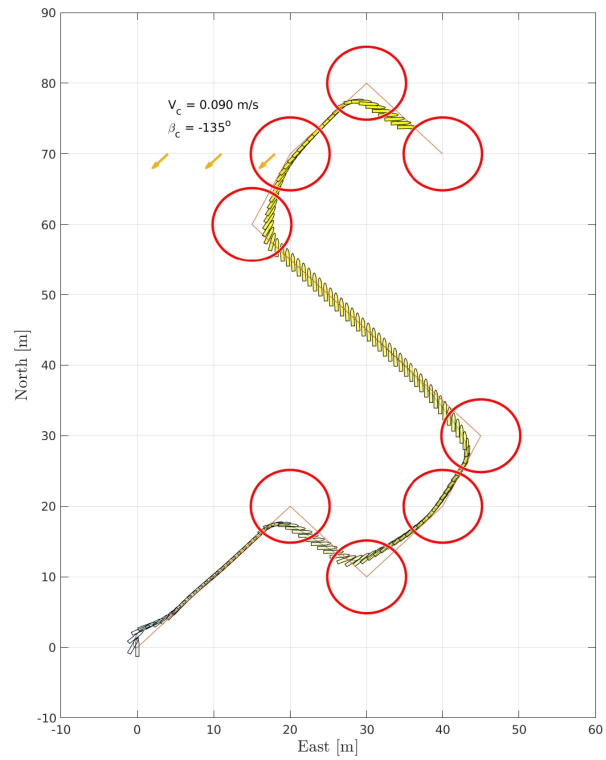

(b) Path - LBS

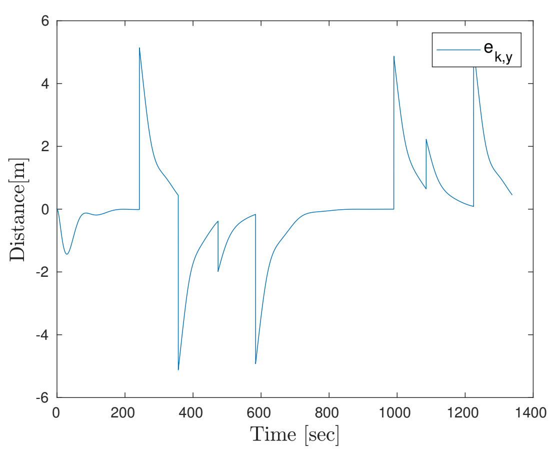

(c) Cross track error - EBS

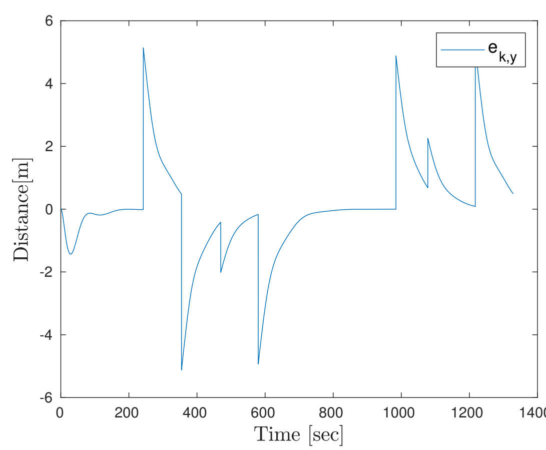

(d) Cross track error - LBS

Figure 7.3: Path plot of LOS guidance with EBS & LBS for straight line paths - with current $V_c = 0.09[m/s]$, $\beta_c = -135°$

Here, we see that despite the large currents, the vessel is able to track the path nicely. Both the heading controller and surge speed controller is able to compensate for the ocean currents. However, it struggles a bit more in sharp turns, but manages to converge to the path in a similar way as in Figure 7.2.

7.5 Line of Sight Guidance - Curved Paths

Now the LOS guidance is extended to track a parameterized path in stead of straight line paths with WP switching logic. In this section we will try to track the C^3 path as shown in Figure 7.1c. According to Skjetne (2005), the objective is now to track the path:

$$\mathcal{P} = \left\{(p, \psi, \upsilon) \in \mathbb{R}^2 \times \mathbb{S}^1 \times \mathbb{R}^3 : \exists s \in \mathbb{R} s.t. p = p_d(s), \psi = \psi_p(s)\right\} \tag{7.16}$$

Where ψ_p is the path-tangential angle we want the heading to converge to. Note that with ocean currents, the objective is to track $\chi \rightarrow \psi_p$, and not $\psi \rightarrow \psi_p$. Therefore, we replace ψ with χ and aim to guide the course to the path-tangential angle in stead of the heading. Note that as crab angle compensation already is performed by the hybrid controller, the output from this guidance scheme will be the derired course, and not heading. We now want to solve the dynamic task

$$\lim_{t\to\infty} |\dot{s}(t) - v_s(s(t), t)| = 0, \qquad v_s(s, t) = \frac{U_d(t)}{\left|p_d^s(s)\right|} \tag{7.17}$$

Next, we define

$$\epsilon(p^n, s) = R(z_{PF}^{\chi_p}(s))^\top (p^n - p_d(s)) = \mathrm{col}(\epsilon_t, \epsilon_n) \tag{7.18}$$

where $p^n \in \mathbb{R}^2$ is the position of the vessel and ϵ_t and ϵ_n denotes the along-track and cross-track distance, respectively. χ_p is the path-tangential angle and is found as:

$$\chi_p(s) = \mathrm{atan2}(p_{d,y}^s(s), p_{d,x}^s(s)) \tag{7.19}$$

Where the generated path-positions $p_d(s)$ and first derivatives $p_d^s(s)$ are found by solving (7.6) with the WPs in (7.7) and differentiate the solution once to obtain the derivative as a function of s. By applying an approach similar to LBS, we have

$$z_{PF}^{\chi_d} = R(z^{\chi_p}) z^{\chi_r}, \qquad z^{\chi_r} = \left[\cos\left(\frac{-\epsilon_n(p^n, s)}{\Delta_{PF}(t)}\right), \sin\left(\frac{-\epsilon_n(p^n, s)}{\Delta_{PF}(t)}\right)\right]^\top \tag{7.20}$$

and the path-parameter s is driven by

$$\dot{s} = \frac{\Delta_{PF}}{\sqrt{\epsilon_n(p, s)^2 + \Delta_{PF}^2}} v_s(s, t) + \mu \frac{p_d^s(s)^\top}{\left|p_d^s(s)\right|}(p - p_d(s)), \qquad \mu > 0, \quad \Delta_{PF} > 0 \tag{7.21}$$

The combination of these equations will ensure the vessel to follow the path and ensures $\epsilon \rightarrow 0$.

7.5.1 Simulations - Without Current

We simulate the path following scheme with the path shown in Figure 7.1c. The desired speed is chosen to be $U_d = 0.1[m/s]$, $R_{PF} = 2L_{pp}$, $\Delta_{PF}(t) = \sqrt{R_{PF}^2 - \epsilon_n(p,s)^2}$, $\mu = 0.01$. The initial attempt in Figure 7.4a turned out to be promising. It was however noticed that the heading controller underperformed in achieving the desired course. Therefore, the gain K_p in the heading controller was amplified from $K_p = 0.04$ to $K_p = 0.12$ such that it induced larger control forces in yaw. The resulting path following plot is shown in Figure 7.4b.

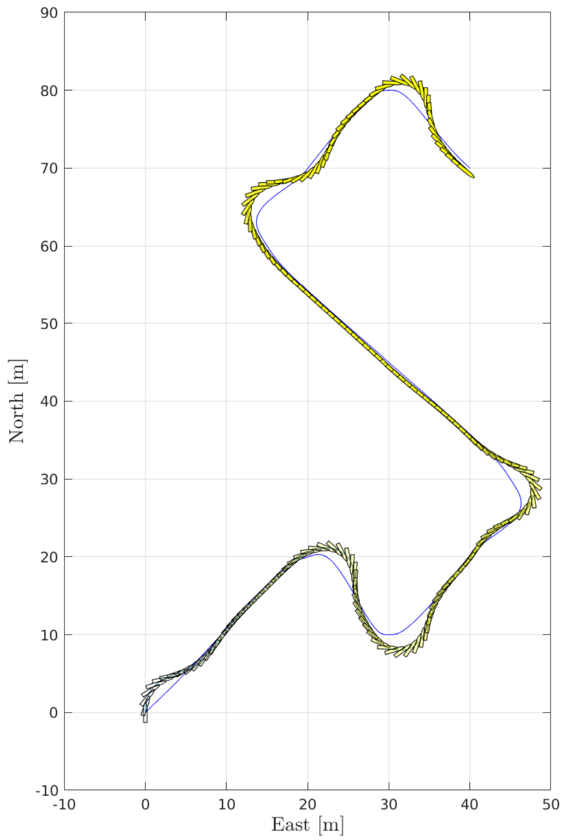

(a) Path - $K_p = 0.04$

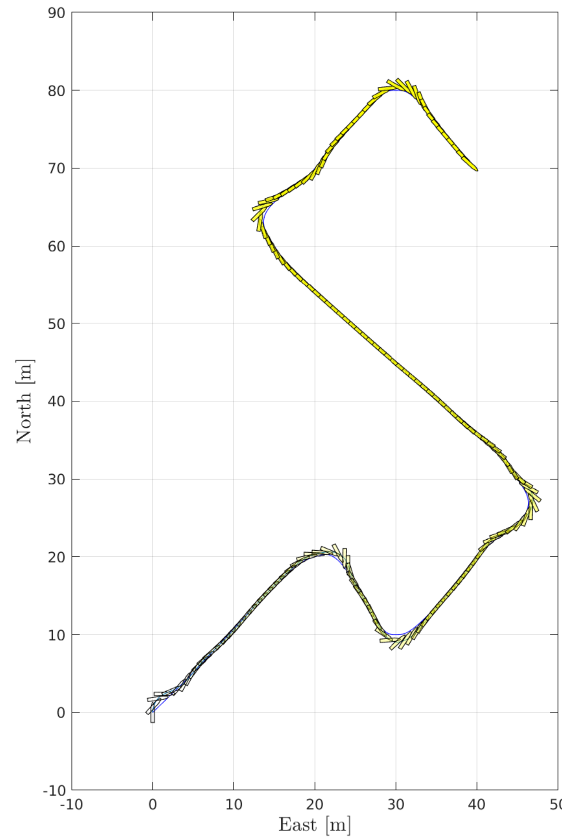

(b) Path - $K_p = 0.12$

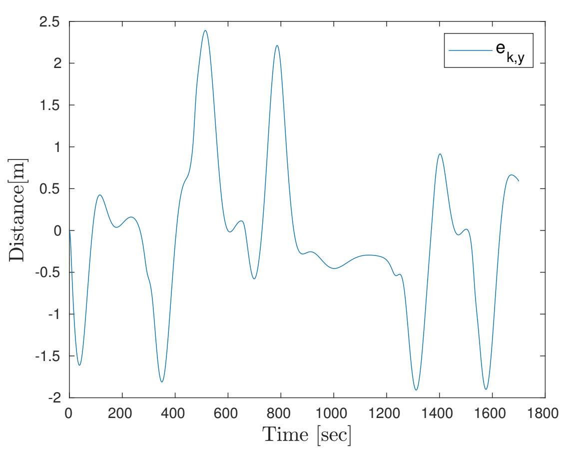

(c) Cross track error - $K_p = 0.04$

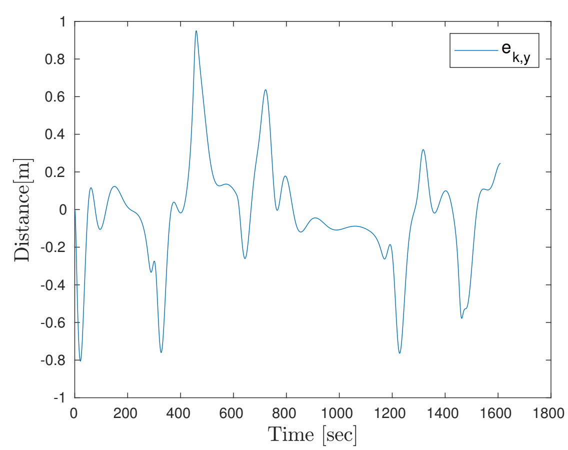

(d) Cross track error - $K_p = 0.12$

Figure 7.4: Path plot of LOS Guidance with path following of curved paths

We can see there is a noticeable difference in the cross track error minimization when amplifying the heading controller gain. With the increased gain, the heading and surge speed controllers were able to follow the desired trajectory generated by the LOS guidance for the curved path. The results are promising and shows that hybrid heading control is adaptable to conventional ways of path following. The next section will present a guidance scheme to guide a vessels trajectory relative to a moving target.

7.6 Target Tracking

This section will extend the target tracking methodology from Section 2.3.5 such that it is suitable for $\mathbb{S}^1$ control. Inspired by Breivik and Fossen (2007), we define a moving target vessels position $p_t(t)$, driven by $\dot{p}_t(t) = U_t(t)z^{\chi_t}(t), U_t > 0$. The target tracking problem is to design a control law (τ_u, τ_r) such that

$$\lim_{t\to\infty} [p^n(t) - p_t(t)] = 0 \tag{7.22}$$

is behaving well and is stable. Different guidance schemes such as *pure pursuit*(PP), *constant bearing*(CB) and LOS are common for solving the target tracking(TT) problem. Focusing on the CG scheme, we let $\tilde{p} = p^n - p_t$, and define the desired velocity by:

$$v_d = U_t z^{\chi_t} - U_a \frac{\tilde{p}}{\sqrt{\tilde{p}^\top \tilde{p} + \Delta_{CB}^2}}, \qquad U_a < U_t \tag{7.23}$$

where the first term is a feedforward term to force the vessel to move with the same velocity vector as the target, and the second is a feedback term that brings the vessel to the target with an approach speed U_a. The parameter $\Delta_{CB} > 0$ is a gain to affect the rendezvous behaviour towards the target vessel. From (7.23) we can define the desired course and speed according to:

$$z_{TT}^{\chi_d} = \frac{v_d}{|v_d|}, \qquad U_d = |v_d| \tag{7.24}$$

Note that if the tracking problem is to obtain and track a relative along- and cross-track position from the target, we can define $\epsilon_d = [e_d, s_d]^\top$ and subtract this from $\tilde{p}$ such that $\tilde{p} = p - p_t - \epsilon_d$ before applying (7.23). The next subsections will present case studies for testing the surge- and heading controller for target tracking purposes.

7.6.1 Simulations

Using $\Delta_{CB} = 2$ and $U_a = 0.05[m/s]$, we initiate a targets position at $p_t(0) = \text{col}(10, 0)$ with a constant velocity $U_t = 0.1[m/s]$ and course $z^{\chi_t} = \mathbf{e}_2(90°)$. The controlled vessel has an initial position at the origin and zero speed. Figure 7.5 shows the vessel and target positions when varying the desired relative positions ϵ_d.

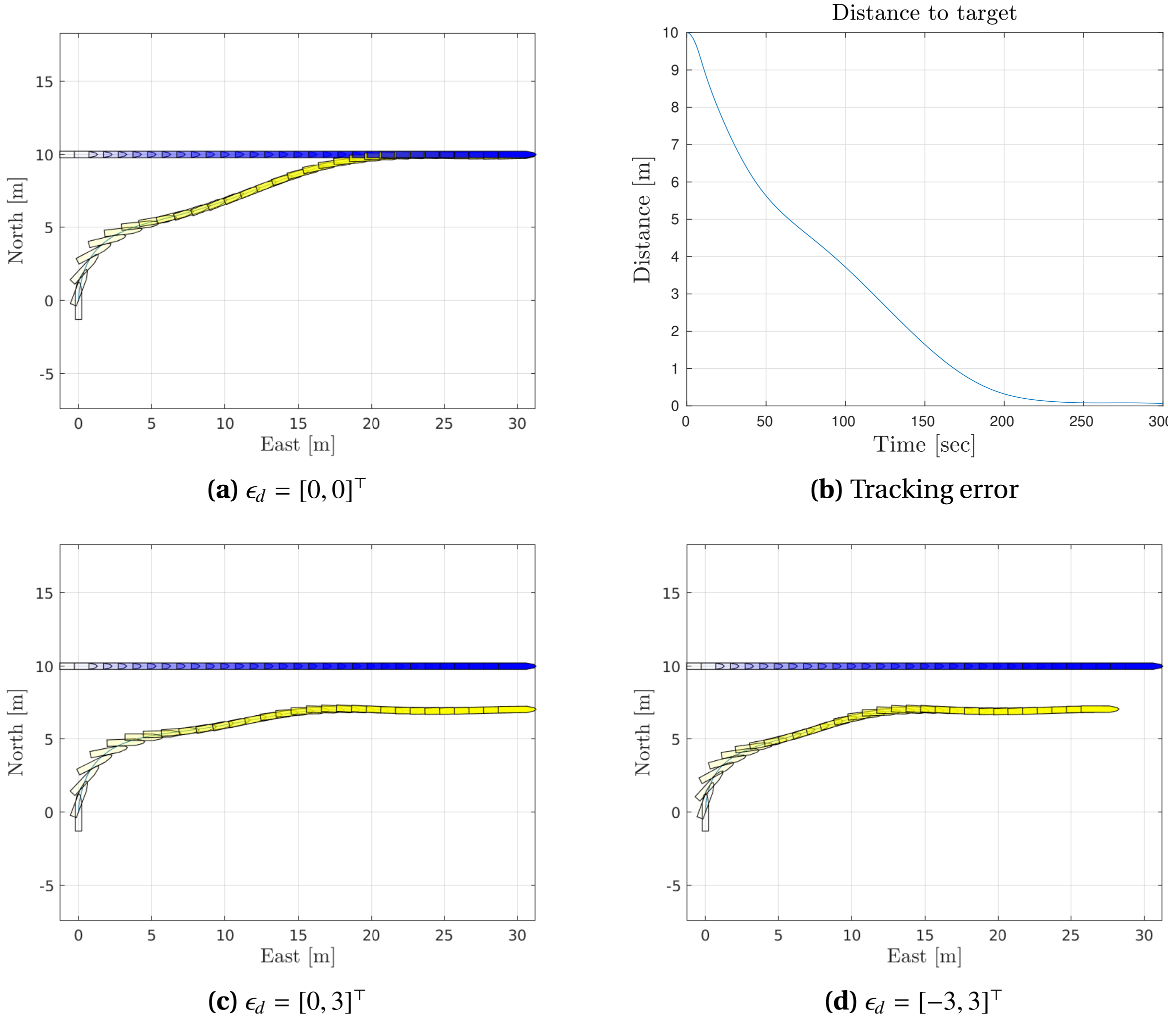

(a) $\epsilon_d = [0, 0]^\top$

(b) Tracking error

(c) $\epsilon_d = [0, 3]^\top$

(d) $\epsilon_d = [-3, 3]^\top$

Figure 7.5: Target tracking with different desired relative positions ϵ_d

We see that the guidance scheme makes sure that the vessel position itself nicely according to the desired relative position to the target vessel. Next, the vessel is tested to track a moving target with time-varying course and speed according to the two cases:

- Case 1:

$$U_t(t) = 0.1 + 0.05 \sin\left(\frac{2\pi t}{400}\right) [m/s], \qquad \chi_t(t) = 90^\circ + 45^\circ \sin\left(\frac{2\pi t}{800}\right) \tag{7.25}$$

- Case 2:

$$U_t(t) = 0.1 + 0.05 \sin\left(\frac{2\pi t}{400}\right) [m/s], \qquad \chi_t(t) = 90^\circ + 90^\circ \sin\left(\frac{2\pi t}{800}\right) \tag{7.26}$$

In both cases, the desired relative position is set to be $\epsilon_d = [-3, 3]^\top$. Figure 7.6 shows the results from Case 1, both with and without current. The vessels positions are now plotted for each 40th second.

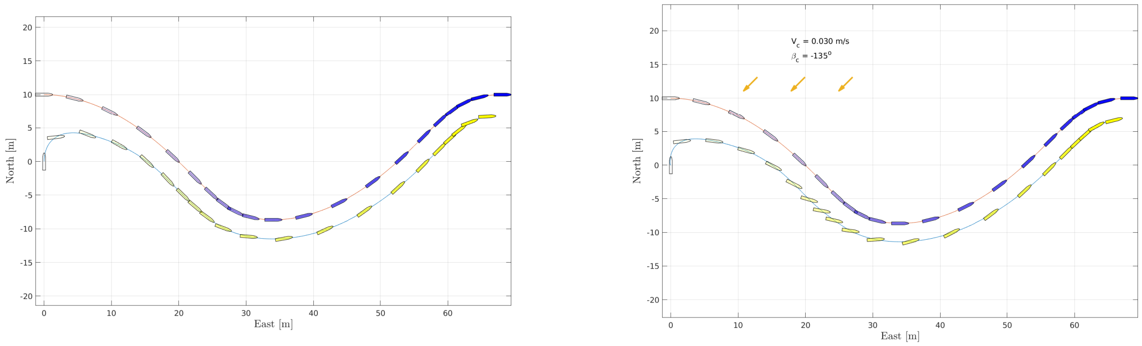

(a) Without current **(b)** With current $V_c = 0.03[m/s], \beta_c = -135°$

Figure 7.6: Case 1: Target tracking with time varying target course and speed with $\epsilon_d = [-3, 3]^\top$

We can see that the vessel is able to successfully track and maintain its desired relative position even though the time variations where the target vessel is speeding up initially, before slowing down in the middle of the first turn. Even with these variations, the target tracking guidance ensures the controlled vessel to smoothing in to the desired relative position and hold it. To test the combined guidance and controllers even more, the time variation amplitudes were made larger according to Case 2, as well as amplifying the current velocity to $V_c = 0.09[m/s]$. Figure 7.7 shows the response.

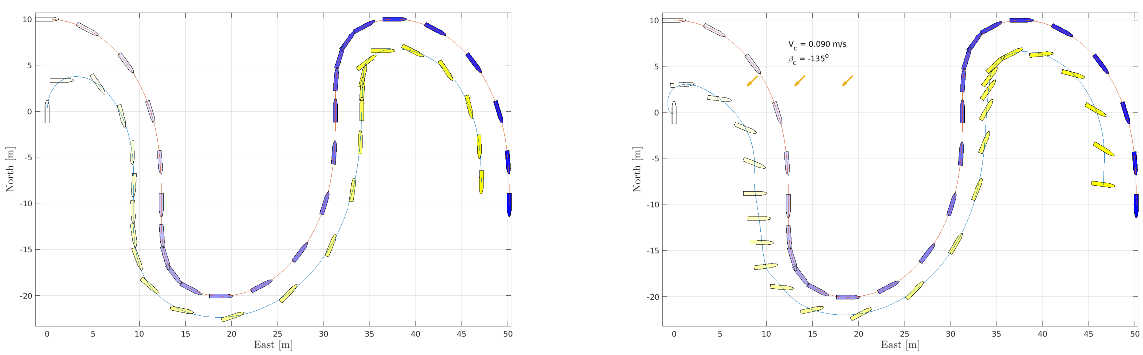

(a) Without current **(b)** With current $V_c = 0.09[m/s], \beta_c = -135°$

Figure 7.7: Case 2: Target tracking with time varying target course and speed with $\epsilon_d = [-3, 3]^\top$

We see that with amplified disturbances and movement of the target, the vessel still obtains a satisfactory tracking performance. We can conclude this by having successfully implemented a robust way of tracking a moving target utilizing an adaptive surge speed controller and hybrid heading controller, both with current compensation.

7.7 Discussion

In this chapter, the VVC problem is extended to PFC with different guidance schemes. For WP tracking, you could either choose to track a C^0 path with LOS-guidance for straight paths and WP switching, or generate a differentiable path for the vessel to follow. Either way, the implementation shows that the VVC ensures the velocity vector to converge to the output of the guidance scheme, and thus make sure the vessel tracks the given path nicely. As mentioned earlier, one concern was the VVC design's ability to track paths that required sharp turns with the low gain of $K_p = 0.04$. When this gain was amplified for the C^3 path, the average cross-track error were reduced by approximately a third. The target tracking performance were also good, and ensured the vessel to obtain a relative position of the target it was tracking, despite large currents and high frequently maneuvers by the target.

Chapter 8

Conclusion and Further Work

8.1 Overall Conclusion

The goal of this thesis was to design, implement and test a robust hybrid heading controller for ships. A suitable potential function that reflected the heading error as the arc length along the unit circle was used as a base, and a non-hybrid virtual control was designed to obtain a satisfactory convergence and stability for all heading errors that were not $\pm 180°$. Then a diffeomorphism was applied to the base potential function and virtual control in order to design two control laws that achieved similar stability characteristics. By a smooth switching logic between these two controls, global asymptotic stability could be achieved. The HHC was combined with a DP controller in surge and sway and tested extensively in the MC-lab to test its robustness. In addition, a Nonlinear Passive Observer and Extended Kalman filter was implemented (but not explained in detail in this thesis) on the lab-experiments, as the velocities needed to be estimated. The HHC was then extended to a VVC problem, and an adaptive surge speed controller as well as sideslip compensation that compensates for the effect of ocean currents was designed for this purpose. Combined with the HHC the vessel was able to track constant and time varying desired velocity vectors, both with and without the influence of current. Finally, the VVC was extended to path following on straight and curved paths with LOS guidance, as well as target tracking applications. The path following guidance were able to guide the vessels velocity vector such that the position of the vessel converged to the path.

Simulations are done on a very simplified model of the vessel with constant mass, damping and Coriolis matrices. For the maneuvering problems, the simple dynamics $\dot{r} = \tau_r$ was chosen to derive the control designs. The vessel was emulated to be underactuated in sway in the control allocation such that the vessel behave as if it was underactuated. With a small modification in the backstepping procedure, more realistic dynamics as the 1DOF Nomoto model can be used to derive more suitable feedback laws with rudder as input if the maneuvering model was linearized at a transit speed and Nomoto gains K and T are chosen accordingly. The control system was first implemented and tested using MATLAB and Simulink. Then HIL simulations were done using the same software as in the MC Lab, and the HHC design was tested physically on the scale model vessel. The VVC and PFC designs were not tested in the MC-lab due to the spacial constraints.

In the simulations, the control allocation assumed that the desired thrust was instantly achieved, and it was therefore no thrust allocation or smoothing of the control input, and it is therefore not guaranteed that the control allocation is suited for scale model test. However, the results shows that the HHC, VVC and PFC works as expected given these delimitations and achieves the control objective.

8.2 Further Work

Continuing this topic of study can be extended by developing a reference model with the same dynamics as $\dot{z} = \omega S z$. In addition, the maneuvering model could be linearized about some design cruise speed such that the Nomoto gains T and K could be chosen. Then only a small modification of the backstepping procedure for the HHC problem gives the rudder as the input. The hybrid controller could be tested with a more high-fidelity model than the one used in this thesis, such as with waves, winds, slowly varying forces and thrust allocation. Then the scale model can be tested in a larger ocean basin or even at open sea, as the spacial constraints as the MC-lab makes the maneuvering and path following designs not so well fitted for testing. However, the hybrid controller could be further tested at the MC-lab with the DP controller. As it was not tested with neither waves or current in the MC-lab, a possible continuation could be to adapt the DP controller in such environments, even with robust switching between different DP modes dependent on the environment. The choice of the gains K_p, K_2, K_3, γ_1 and γ_2 was done by trial and error, but this tuning could be performed in a more structured/mathematical manner or even with the aid of machine learning. As this thesis is a stepping stone for more advanced hybrid control systems for ships that increases the level of autonomy and robustness, it could be extended to work on spherical orientation control on $\mathbb{S}^2$ such as underwater robotics, and adapted to do more coordinated operations where several vessels or underwater vehicles cooperate. Full scale testing would also give valuable insight on how the overall performance is compared to model tests. In addition, collision avoidance guidance that follows the Convention on the International Regulations for Preventing Collisions at Sea (COLREG) could be investigated further.

Bibliography

Bhat, S. P., Bernstein, D. S., 2000. A topological obstruction to continuous global stabilization of rotational motion and the unwinding phenomenon. Systems Control Letters 39 (1), 63 – 70. URL http://www.sciencedirect.com/science/article/pii/S0167691199000900

Bjørnø, J., 2016. Thruster-assisted position mooring of c/s inocean cat i drillship.

Bjørnø, J., 2019. 6dof vessel model of csad received on mail from jon bjørnø.

Breivik, M., 2010. Topics in guided motion control of marine vehicles.

Breivik, M., Fossen, T. I., 2004. Path following of straight lines and circles for marine surface vessels. IFAC Proceedings Volumes 37 (10), 65–70.

Breivik, M., Fossen, T. I., 2007. Applying missile guidance concepts to motion control of marine craft. IFAC Proceedings Volumes 40 (17), 349 – 354, 7th IFAC Conference on Control Applications in Marine Systems.
URL http://www.sciencedirect.com/science/article/pii/S1474667015321200

Carlton, J., 2012. Marine propellers and propulsion.

Fossen, T., Pettersen, K., Galeazzi, R., 2015. Line-of-sight path following for dubins paths with adaptive sideslip compensation of drift forces. Ieee Transactions On Control Systems Technology 23 (2), 820–827.

Fossen, T. I., 2011. Handbook of marine craft hydrodynamics and motion control.

Fossen, T. I., 2016. Ttk4190-kinematics chapter 2, url: http://www.fossen.biz/wiley/Ch2.pdf.

Fossen, T. I., Breivik, M., Skjetne, R., 2003. Line-of-sight path following of underactuated marine craft. IFAC Proceedings Volumes 36 (21), 211–216.

Frederich, P., 2016. Constrained optimal thrust allocation for c/s inocean cat i drillship.

G. Sanfelice, R., Goebel, R., R. Teel, A., 01 2008. Invariance principles for hybrid systems with connections to detectability and asymptotic stability. Automatic Control, IEEE Transactions on 52, 2282 – 2297.

Haug, S., 2018. Robust hybrid course control of shipt- project thesis.

Lekkas, A., 2018. Ttk23: Introduction to autonomous robotic systems for industry 4.0 - lecture notes, nTNU, ITK.

Ludvigsen, M., Sørensen, A. J., 2016. Towards integrated autonomous underwater operations for ocean mapping and monitoring. Annual Reviews in Control 42, 145 – 157.
URL http://www.sciencedirect.com/science/article/pii/S1367578816300256

Lyngstadaas, O. N., 2018. Ship motion control concepts considering actuator constraints.

Matthews Gerald, Reinerman-Jones Lauren, B. D. T. G. W. R. L. J. P. A. R., 2016. Resilient autonomous systems: Challenges and solutions. Annual Reviews in Control, 208 – 213. 10.1109/RWEEK.2016.7573335.

Mayhew, C. G., Sanfelice, R. G., Teel, A. R., June 2011. Synergistic lyapunov functions and backstepping hybrid feedbacks. In: Proceedings of the 2011 American Control Conference. pp. 3203–3208.

Mayhew, C. G., Teel, A. R., June 2010. Hybrid control of planar rotations. In: Proceedings of the 2010 American Control Conference. pp. 154–159.

MCL, 2017. Marine cybernetics laboratory handbook. https://www.ntnu.edu/imt/lab/cybernetics.

National Research Council, 2005. Autonomous Vehicles in Support of Naval Operations. Committee on Autonomous Vehicles in Support of Naval Operations. ISBN: 0-309-09676-6.
URL https://scholar.google.com/scholar_lookup?title=Autonomous%20vehicles%20in%20support%20of%20naval%20operations&author=National%20Research%20Council&publication_year=2005

NIST, 2018. Autonomy levels for unmanned systems, url: http://www.nist.gov/el/isd/ks/autonomy_levels.cfm - Retrieved November 2018.

Nomoto, K., Taguchi, K., 1957. On steering qualities of ships. technical report. international shipbuilding progress, vol.4. Journal of Zosen Kiokai 1957 (101), 57–66.

NTNU, 2017. Cybership arctic drillship user manual. Retrieved from https://github.com/NTNU-MCS/MC_Lab_Handbook/blob/master/Version%202.0/CSAD%20Handbook/CSAD.pdf.

Rafal Goebel, R. G. S., Teel, A. R., 2012. Hybrid Dynamical Systems. Modeling, Stability, and Robustness. Princeton University Press.

Skjetne, R., 03 2005. The maneuvering problem. Ph.D. thesis.

Skjetne, R., 2018. Notes on: Ship maneuvering model and velocity control. Revision B. Unpublished.

Skjetne, R., 2019. Lecture 7: Maneuvering control design. Handout. Unpublished.

Sæterdal, T. E., 2018. Nonlinear adaptive motion controllers for ships: Model-scale experiments in an ocean basin.

Teel, A., 2018. Velocity tracking - technical note. Unpublished.

Tzeng, C.-Y., 06 1998. Analysis of the pivot point for a turning ship. Journal of Marine Science and Technology 6, 39–44.

Appendix A

Appendix

The following mathematical model in $\mathbb{R}^3$ is used:

$$\mathbf{M}\dot{\boldsymbol{\upsilon}}_r + \mathbf{C}(\boldsymbol{\upsilon}_r)\boldsymbol{\upsilon}_r + \mathbf{D}(\boldsymbol{\upsilon}_r)\boldsymbol{\upsilon}_r = \boldsymbol{\tau}, \tag{A.1}$$

A.1 Numerical Values for the CSAD Model

Table A.1 shows the numerical values of the parameters from different sources. The rightmost column is the chosen parameters used in this thesis.

Table A.1: Numerical values of CSAD

Parameter	Bjørnø (2016)	vesselABC from Bjørnø (2019)	Sæterdal (2018) & Lyngstadaas (2018) Session 1	Sæterdal (2018) Session 2	Lyngstadaas (2018) Session 2	Chosen parameters for this thesis	Unit
L	2.578	2.578	2.578	2.578	2.578	2.578	m
m	127.92	127.5122	127.92	127.92	127.92	127.92	kg
x_g	0	0.0433	**0.0375**	0.0375	0.0375	0.0375	m
I_z	61.967	61.7689	62	62	62	62	kgm^2
$X_{\dot{u}}$	3.262	-3.6975	**-3.262**	**-10**	**-10**	-10	kg
$Y_{\dot{v}}$	28.89	-29.1179	-28.9	**-105**	**-105**	-105	kg
$Y_{\dot{r}}$	0.525	-1.559	**-0.525**	-0.525	-0.525	-0.525	kgm
$N_{\dot{v}}$	0.157	-0.5922	**-0.157**	-0.157	-0.157	-0.157	kgm
$N_{\dot{r}}$	14	-12.6085	**-14**	**-3.5**	**-3.495**	-3.5	kgm^2
X_u	-2.332	-	-2.33	**-5.1**	**-5.35**	-5.35	kg/s
$X_{\|u\|u}$	0	-	0	0	0	0	kg/m
X_{uuu}	-8.56	-	-8.56	**-18.63**	**-19.6312**	-19	kgs/m^2
Y_v	-4.673	-	-4.67	**-10.2**	**-10.16**	-10.2	kg/s
$Y_{\|v\|v}$	0.3976	-	**-0.398**	**-0.86**	**-0.8647**	-0.86	kg/m
Y_{vvv}	-313	-	-313	**-665**	**-681.175**	-681	kgs/m^2
N_v	0	-	0	0	0	0	kgm/s
$N_{\|v\|v}$	-0.2088	-	-0.209	**-0.24**	-0.2088	-0.21	kg/m
N_{vvv}	0	-	0	0	0	0	kgs/m^2
Y_r	-7.25	-	-7.25	**-6.25**	-7.25	-7.25	kgm/s
$Y_{\|r\|r}$	-3.45	-	-3.450	**-3.65**	-3.450	-3.45	kg/s
Y_{rrr}	0	-	0	0	0	0	kgs/m^2
N_r	-0.0168	-	**-6.916**	**-14.55**	**-14.55**	-14.55	kg/s
$N_{\|r\|r}$	-0.0115	-	**-4.73**	**-9.96**	**-9.9597**	-9.96	kgm^2
N_{rrr}	- 0.000358	-	**-0.147**	**-0.31**	**-0.3101**	-0.31	kgs/m^2
$N_{\|v\|r}$	0.08	-	0.08	**0**	0.08	0.08	kg/m
$N_{\|r\|v}$	0.08	-	0.08	**0**	0.08	0.08	kg/m
$Y_{\|v\|r}$	-0.845	-	-0.845	**0**	-0.845	-0.845	kg
$Y_{\|r\|v}$	-0.805	-	-0.805	**0**	-0.805	-0.805	kg

Direct calculation of $\mathbf{M}$ and $\mathbf{D}_L$ yields:

$$\mathbf{M} = \begin{bmatrix} 137.92 & 0 & 0 \\ 0 & 232.92 & 5.3220 \\ 0 & 4.9540 & 58.5 \end{bmatrix} \tag{A.2}$$

$$\mathbf{D}_L = \begin{bmatrix} 5.35 & 0 & 0 \\ 0 & 10.2 & 7.25 \\ 0 & 0 & 14.55 \end{bmatrix} \tag{A.3}$$

It is observed that $m_{23} \neq m_{32}$. In some derivations for CDMs, the parameter $m^*_{23} = m^*_{32} = \frac{1}{2}(m_{23} + m_{32}) = 5.138$ is used for simplification. However, in simulations, the original mass matrix is used.

A.2 Derivations of $\nabla_z\vartheta(z)$ and $\nabla_z\kappa_{02}(z)$

$$\nabla_z\kappa_{02}(z) = \begin{bmatrix} \frac{\partial\kappa_{02}(z)}{\partial z_x} & \frac{\partial\kappa_{02}(z)}{\partial z_y} \end{bmatrix} \tag{A.4}$$

$$\begin{aligned} \frac{\partial\kappa_{02}(z)}{\partial z_x} = &-\frac{K_p\, z_x}{2\,(\lambda^2\, {z_x}^2 - 1)\,\sqrt{L\,(\mathrm{acos}\,(\lambda\, z_x) - \mathrm{acos}\,(\lambda))}} \\ &- \frac{K_p\,\sqrt{L\,(\mathrm{acos}\,(\lambda\, z_x) - \mathrm{acos}\,(\lambda))}}{L\,\lambda\,\sqrt{1 - \lambda^2\, {z_x}^2}} \\ &- \frac{K_p\,\lambda\, {z_x}^2\,\sqrt{L\,(\mathrm{acos}\,(\lambda\, z_x) - \mathrm{acos}\,(\lambda))}}{L\,(1 - \lambda^2\, {z_x}^2)^{3/2}} \end{aligned} \tag{A.5}$$

$$\frac{\partial\kappa_{02}(z)}{\partial z_y} = 0 \tag{A.6}$$

$$\nabla_z\vartheta(z) = \begin{bmatrix} \frac{\partial\kappa_{\mathcal{T}_1}}{z_x} & \frac{\partial\kappa_{\mathcal{T}_1}}{z_y} \\ \frac{\partial\kappa_{\mathcal{T}_2}}{z_x} & \frac{\partial\kappa_{\mathcal{T}_2}}{z_y} \end{bmatrix} = \begin{bmatrix} a_{11} & a_{12} \\ a_{21} & a_{22} \end{bmatrix} \tag{A.7}$$

where a_{1q} and a_{2q} for $q = \{1, 2\}$ are shown below. These are solved by using the algebraic expression for $\kappa_{\mathcal{T}_q}$ with symbolic variables and calling the MATLAB function *diff* $(\kappa_{\mathcal{T}_q}, z_x)$ and *diff* $(\kappa_{\mathcal{T}_q}, z_y)$.

$$
\begin{aligned}
a_{1q} = {} & \frac{K_p\, k_q\, \lambda^2 z_x z_y \left(z_x \cos\left(L k_q\, (\mathrm{acos}(\lambda z_x) - \mathrm{acos}(\lambda))\right) - z_y \sin\left(L k_q\, (\mathrm{acos}(\lambda z_x) - \mathrm{acos}(\lambda))\right)\right) \sqrt{L\left(\mathrm{acos}\left(\lambda\left(z_x \cos\left(L k_q\, (\mathrm{acos}(\lambda z_x) - \mathrm{acos}(\lambda))\right) - z_y \sin\left(L k_q\, (\mathrm{acos}(\lambda z_x) - \mathrm{acos}(\lambda))\right)\right)\right) - \mathrm{acos}(\lambda)\right)}}{\left(\frac{L k_q \lambda z_y}{\sqrt{1-\lambda^2 z_x^2}} + 1\right)^2 \left(1 - \lambda^2 z_x^2\right)^{3/2} \sqrt{1 - \lambda^2 \left(z_x \cos\left(L k_q\, (\mathrm{acos}(\lambda z_x) - \mathrm{acos}(\lambda))\right) - z_y \sin\left(L k_q\, (\mathrm{acos}(\lambda z_x) - \mathrm{acos}(\lambda))\right)\right)^2}} \\
& - \frac{K_p \sqrt{L\left(\mathrm{acos}\left(\lambda\left(z_x \cos\left(L k_q\, (\mathrm{acos}(\lambda z_x) - \mathrm{acos}(\lambda))\right) - z_y \sin\left(L k_q\, (\mathrm{acos}(\lambda z_x) - \mathrm{acos}(\lambda))\right)\right)\right) - \mathrm{acos}(\lambda)\right)} \left(\cos\left(L k_q\, (\mathrm{acos}(\lambda z_x) - \mathrm{acos}(\lambda))\right) + \frac{L k_q \lambda z_y \cos\left(L k_q\, (\mathrm{acos}(\lambda z_x) - \mathrm{acos}(\lambda))\right)}{\sqrt{1-\lambda^2 z_x^2}} + \frac{L k_q \lambda z_x \sin\left(L k_q\, (\mathrm{acos}(\lambda z_x) - \mathrm{acos}(\lambda))\right)}{\sqrt{1-\lambda^2 z_x^2}}\right)}{L \lambda \left(\frac{L k_q \lambda z_y}{\sqrt{1-\lambda^2 z_x^2}} + 1\right) \sqrt{1 - \lambda^2 \left(z_x \cos\left(L k_q\, (\mathrm{acos}(\lambda z_x) - \mathrm{acos}(\lambda))\right) - z_y \sin\left(L k_q\, (\mathrm{acos}(\lambda z_x) - \mathrm{acos}(\lambda))\right)\right)^2}} \\
& - \frac{K_p \lambda \left(z_x \cos\left(L k_q\, (\mathrm{acos}(\lambda z_x) - \mathrm{acos}(\lambda))\right) - z_y \sin\left(L k_q\, (\mathrm{acos}(\lambda z_x) - \mathrm{acos}(\lambda))\right)\right)^2 \sqrt{L\left(\mathrm{acos}\left(\lambda\left(z_x \cos\left(L k_q\, (\mathrm{acos}(\lambda z_x) - \mathrm{acos}(\lambda))\right) - z_y \sin\left(L k_q\, (\mathrm{acos}(\lambda z_x) - \mathrm{acos}(\lambda))\right)\right)\right) - \mathrm{acos}(\lambda)\right)} \left(\cos\left(L k_q\, (\mathrm{acos}(\lambda z_x) - \mathrm{acos}(\lambda))\right) + \frac{L k_q \lambda z_y \cos\left(L k_q\, (\mathrm{acos}(\lambda z_x) - \mathrm{acos}(\lambda))\right)}{\sqrt{1-\lambda^2 z_x^2}} + \frac{L k_q \lambda z_x \sin\left(L k_q\, (\mathrm{acos}(\lambda z_x) - \mathrm{acos}(\lambda))\right)}{\sqrt{1-\lambda^2 z_x^2}}\right)}{L \left(\frac{L k_q \lambda z_y}{\sqrt{1-\lambda^2 z_x^2}} + 1\right) \left(1 - \lambda^2 \left(z_x \cos\left(L k_q\, (\mathrm{acos}(\lambda z_x) - \mathrm{acos}(\lambda))\right) - z_y \sin\left(L k_q\, (\mathrm{acos}(\lambda z_x) - \mathrm{acos}(\lambda))\right)\right)^2\right)^{3/2}} \\
& - \frac{K_p \left(z_x \cos\left(L k_q\, (\mathrm{acos}(\lambda z_x) - \mathrm{acos}(\lambda))\right) - z_y \sin\left(L k_q\, (\mathrm{acos}(\lambda z_x) - \mathrm{acos}(\lambda))\right)\right) \left(\cos\left(L k_q\, (\mathrm{acos}(\lambda z_x) - \mathrm{acos}(\lambda))\right) + \frac{L k_q \lambda z_y \cos\left(L k_q\, (\mathrm{acos}(\lambda z_x) - \mathrm{acos}(\lambda))\right)}{\sqrt{1-\lambda^2 z_x^2}} + \frac{L k_q \lambda z_x \sin\left(L k_q\, (\mathrm{acos}(\lambda z_x) - \mathrm{acos}(\lambda))\right)}{\sqrt{1-\lambda^2 z_x^2}}\right)}{2 \left(\frac{L k_q \lambda z_y}{\sqrt{1-\lambda^2 z_x^2}} + 1\right) \left(\lambda^2 \left(z_x \cos\left(L k_q\, (\mathrm{acos}(\lambda z_x) - \mathrm{acos}(\lambda))\right) - z_y \sin\left(L k_q\, (\mathrm{acos}(\lambda z_x) - \mathrm{acos}(\lambda))\right)\right)^2 - 1\right) \sqrt{L\left(\mathrm{acos}\left(\lambda\left(z_x \cos\left(L k_q\, (\mathrm{acos}(\lambda z_x) - \mathrm{acos}(\lambda))\right) - z_y \sin\left(L k_q\, (\mathrm{acos}(\lambda z_x) - \mathrm{acos}(\lambda))\right)\right)\right) - \mathrm{acos}(\lambda)\right)}}
\end{aligned}
$$

$$
\begin{aligned}
a_{2q} = {} & \frac{K_p \sin\left(L k_q \left(\mathrm{acos}(\lambda z_x) - \mathrm{acos}(\lambda)\right)\right)\left(z_x \cos\left(L k_q \left(\mathrm{acos}(\lambda z_x) - \mathrm{acos}(\lambda)\right)\right) - z_y \sin\left(L k_q \left(\mathrm{acos}(\lambda z_x) - \mathrm{acos}(\lambda)\right)\right)\right)}{2\left(\frac{L k_q \lambda z_y}{\sqrt{1-\lambda^2 z_x^2}} + 1\right)\left(\lambda^2\left(z_x \cos\left(L k_q \left(\mathrm{acos}(\lambda z_x) - \mathrm{acos}(\lambda)\right)\right) - z_y \sin\left(L k_q \left(\mathrm{acos}(\lambda z_x) - \mathrm{acos}(\lambda)\right)\right)\right)^2 - 1\right)\sqrt{L\left(\mathrm{acos}\left(\lambda\left(z_x \cos\left(L k_q \left(\mathrm{acos}(\lambda z_x) - \mathrm{acos}(\lambda)\right)\right) - z_y \sin\left(L k_q \left(\mathrm{acos}(\lambda z_x) - \mathrm{acos}(\lambda)\right)\right)\right)\right) - \mathrm{acos}(\lambda)\right)}} \\
& + \frac{K_p \sin\left(L k_q \left(\mathrm{acos}(\lambda z_x) - \mathrm{acos}(\lambda)\right)\right)\sqrt{L\left(\mathrm{acos}\left(\lambda\left(z_x \cos\left(L k_q \left(\mathrm{acos}(\lambda z_x) - \mathrm{acos}(\lambda)\right)\right) - z_y \sin\left(L k_q \left(\mathrm{acos}(\lambda z_x) - \mathrm{acos}(\lambda)\right)\right)\right)\right) - \mathrm{acos}(\lambda)\right)}}{L\lambda\left(\frac{L k_q \lambda z_y}{\sqrt{1-\lambda^2 z_x^2}} + 1\right)\sqrt{1 - \lambda^2\left(z_x \cos\left(L k_q \left(\mathrm{acos}(\lambda z_x) - \mathrm{acos}(\lambda)\right)\right) - z_y \sin\left(L k_q \left(\mathrm{acos}(\lambda z_x) - \mathrm{acos}(\lambda)\right)\right)\right)^2}} \\
& + \frac{K_p k_q\left(z_x \cos\left(L k_q \left(\mathrm{acos}(\lambda z_x) - \mathrm{acos}(\lambda)\right)\right) - z_y \sin\left(L k_q \left(\mathrm{acos}(\lambda z_x) - \mathrm{acos}(\lambda)\right)\right)\right)\sqrt{L\left(\mathrm{acos}\left(\lambda\left(z_x \cos\left(L k_q \left(\mathrm{acos}(\lambda z_x) - \mathrm{acos}(\lambda)\right)\right) - z_y \sin\left(L k_q \left(\mathrm{acos}(\lambda z_x) - \mathrm{acos}(\lambda)\right)\right)\right)\right) - \mathrm{acos}(\lambda)\right)}}{\left(\frac{L k_q \lambda z_y}{\sqrt{1-\lambda^2 z_x^2}} + 1\right)^2\sqrt{1 - \lambda^2 z_x^2}\sqrt{1 - \lambda^2\left(z_x \cos\left(L k_q \left(\mathrm{acos}(\lambda z_x) - \mathrm{acos}(\lambda)\right)\right) - z_y \sin\left(L k_q \left(\mathrm{acos}(\lambda z_x) - \mathrm{acos}(\lambda)\right)\right)\right)^2}} \\
& + \frac{K_p \lambda \sin\left(L k_q \left(\mathrm{acos}(\lambda z_x) - \mathrm{acos}(\lambda)\right)\right)\left(z_x \cos\left(L k_q \left(\mathrm{acos}(\lambda z_x) - \mathrm{acos}(\lambda)\right)\right) - z_y \sin\left(L k_q \left(\mathrm{acos}(\lambda z_x) - \mathrm{acos}(\lambda)\right)\right)\right)^2\sqrt{L\left(\mathrm{acos}\left(\lambda\left(z_x \cos\left(L k_q \left(\mathrm{acos}(\lambda z_x) - \mathrm{acos}(\lambda)\right)\right) - z_y \sin\left(L k_q \left(\mathrm{acos}(\lambda z_x) - \mathrm{acos}(\lambda)\right)\right)\right)\right) - \mathrm{acos}(\lambda)\right)}}{L\left(\frac{L k_q \lambda z_y}{\sqrt{1-\lambda^2 z_x^2}} + 1\right)\left(1 - \lambda^2\left(z_x \cos\left(L k_q \left(\mathrm{acos}(\lambda z_x) - \mathrm{acos}(\lambda)\right)\right) - z_y \sin\left(L k_q \left(\mathrm{acos}(\lambda z_x) - \mathrm{acos}(\lambda)\right)\right)\right)^2\right)^{3/2}}
\end{aligned}
$$

Appendix B

Video of Experiment

This video presents the lab experiments showing the hybrid mechanisms for which way the vessel turns when initiated at an angle $\psi_0 = 0°$ and receives setpoints of $\psi_d = \{-170°, 170°, 180°\}$ with initial logic modes $q_0 = \{1, 2\}$.

https://vimeo.com/344285825